

# HYDRODYNAMIC SIMULATIONS OF EJECTA PRODUCTION FROM SHOCKED METALLIC SURFACES

by

Varad Abhimanyu Karkhanis

A dissertation submitted to the faculty of  
The University of North Carolina at Charlotte  
in partial fulfillment of the requirements  
for the degree of Doctor of Philosophy in  
Mechanical Engineering

Charlotte

2017

Approved by:

---

Dr. Praveen Ramaprabhu

---

Dr. Russell Keanini

---

Dr. David Weggel

---

Dr. Shaozhong Deng



## ABSTRACT

VARAD ABHIMANYU KARKHANIS. Hydrodynamic Simulations of Ejecta Production from Shocked Metallic Surfaces. (Under the direction of DR. PRAVEEN RAMAPRABHU)

The phenomenon of mass ejection into vacuum from a shocked metallic free surfaces can have a deleterious effect on the implosion phase of the Inertial Confinement Fusion (ICF) process. Often, the ejecta take the form of a cloud of particles that are the result of microjetting sourced from imperfections on the metallic free surface. Significant progress has been achieved in the understanding of ejecta dynamics by treating the process as a limiting case of the baroclinically-driven Richtmyer-Meshkov Instability (RMI). This conceptual picture is complicated by several practical considerations including breakup of spikes due to surface tension and yield strength of the metal. Thus, the problem involves a wide range of physical phenomena, occurring often under extreme conditions of material behavior.

We describe an approach in which continuum simulations using ideal gases can be used to capture key aspects of ejecta growth associated with the RMI. The approach exploits the analogy between the Rankine-Hugoniot jump conditions for ideal gases and the linear relationship between the shock velocity and particle velocity governing shocked metals. Such simulations with  $\gamma$ -law fluids have been successful in accurately predicting the velocity and mass of ejecta for different shapes, and in excellent agreement with experiments. We use the astrophysical FLASH code, developed at the University of Chicago to model this problem. Based on insights from our simulations, we suggest a modified expression for ejecta velocities that is valid for large initial perturbation

amplitudes. The expression for velocities is extended to ejecta originating from cavities with any arbitrary shape. The simulations are also used to validate a recently proposed source model for ejecta that predicts the ejected mass per unit area for sinusoidal and non-standard shapes. Such simulations and theoretical models play an important role in the design of target experiment campaigns.

## DEDICATION

I dedicate this work to my loving wife, my amazing brother, and my extraordinary parents.

## ACKNOWLEDGMENTS

I would like to thank my thesis advisor, and my mentor Dr. Praveen Ramaprabhu for providing me an opportunity to work on this research. His continuous guidance and evaluation of my work always kept me on the right track. His encouragement to try new things, and motivation to aim for the best helped me in many ways. I would like to thank my thesis committee members Dr. Russell Keanini, Dr. David Weggel, and Dr. Shaozhong Deng for reviewing my thesis, and helping me out in meeting important deadlines imposed by the graduate school.

I would like to thank Mr. Pedram Bigdelou (Laboratory for Multiscale Computational Fluid Dynamics) for helping me out in preparing my thesis draft, and defense presentation. I thank Mr. Ismael D. Boureima for his timely help in many aspects.

Finally, I thank Drs. J. E. Hammerberg, F. J. Cherne, and M. J. Andrews (Los Alamos National Laboratory) for guidance, and useful discussions. This work was supported by the (U.S.) Department of Energy (DOE) under Contract No. DE-AC52-06NA2-5396. FLASH was developed by the DOE-sponsored ASC/Alliance Center for Astrophysical Thermonuclear Flashes at the University of Chicago.

## TABLE OF CONTENTS

LIST OF TABLES	viii
LIST OF FIGURES	ix
CHAPTER 1: INTRODUCTION AND LITERATURE REVIEW	1
1.1 Ejecta bubble and spike velocity models	4
1.2 Ejecta mass models	8
CHAPTER 2: PROBLEM SETUP AND NUMERICAL METHOD	11
CHAPTER 3: EJECTED MASS FROM NON-SINUSOIDAL SHAPES	17
3.1 Surfaces studied	17
3.2 Discussion and Results	23
CHAPTER 4: EJECTA PRODUCTION FROM SECOND SHOCK	35
4.1 Ejecta simulations ( $A \rightarrow -1$ cases)	36
4.2 Bubble Surface Shape Analysis	46
4.3 Comparison with the experiments	52
CHAPTER 5: NUMERICAL STUDY OF BUBBLE AND SPIKE	60
VELOCITIES IN SHOCK-DRIVEN LIQUID METALS	
5.1 Extension to non-sinusoidal shapes	61
5.2 Initial amplitude variation (Sinusoidal interfaces)	63
5.3 Non-sinusoidal Shapes	74
5.4 Ejected mass per unit area	82
CHAPTER 6: SUMMARY AND CONCLUSIONS	86
REFERENCES	93

## LIST OF TABLES

TABLE. 3.1. FLASH simulations: (a) $kh_0=1/8$ , $h_0=0.02$ cm, $\lambda=1.0$ cm. (b) $kh_0=1.0$ , $h_0=0.1592$ cm, $\lambda=1.0$ cm.	(25)
TABLE 4.1. Summary of FLASH simulations ( $A \rightarrow -1$ ).	(37)
TABLE 4.2. Geometric properties of the interfaces at second shock from FLASH simulations.	(49)
TABLE 5.1. Interface shapes investigated using FLASH ( $\lambda=1$ cm) simulations ( $kh_0=1/8$ , 0.5, 1 and 2).	(75)



## LIST OF FIGURES

- FIG. 2.1. Schematic of the computational domain showing the problem configuration and nomenclature adopted from [46]. (a) Initial condition, (b) configuration after shock-interface interaction. (15)
- FIG. 2.2. x-t diagram from a typical second shock simulation.  $SI_1$  – first shock-interface interaction,  $TS_1$ - transmitted shock wave from first shock,  $RR_1$ - Reflected rarefaction from first shock,  $IS_1$  – Incident shock 1 and so on. (16)
- FIG. 3.1. The shapes described by these functions. a) Sinusoidal, b) Chevron, c) Fly-Cut, d) Square-Wave, and e) Gaussian. (18)
- FIG. 3.2. FLASH simulations for Sinusoidal (upper panel), Chevron (middle panel) and Square-Wave (lower panel) shapes.  $kh_0 = 1$ ,  $t/\tau = 16.77$ . (26)
- FIG. 3.3. FLASH simulations for Sinusoidal (upper panel), Chevron (middle panel) and Square-Wave (lower panel) shapes.  $kh_0 = 1$ ,  $t/\tau = 0, 1.16, 6.32, 12.76, 25.62$ , and  $51.38$ . (27)
- FIG. 3.4. Ejected mass per unit area for FLASH simulations. (31)  
a)  $kh_0 = 1/8$ ,  $m(t)$  vs. time; b)  $kh_0 = 1/8$ , scaled mass  $m(t)/(2/3m_{0eff})$  vs. time; c)  $kh_0 = 1$ ,  $m(t)$  vs. time; d)  $kh_0 = 1$ , scaled mass  $m(t)/(2/3m_{0eff})$  vs. time.
- FIG. 3.5. Simulation mass per unit area compared with theoretical model, FLASH simulations. (a) and (b)  $kh_0 = 1/8$ : (a) Method I, (b) Method II; (c) and (d)  $kh_0 = 1$ : (c) Method I, (d) Method II. Dashed line—theoretical model. (33)
- FIG. 4.1. Density contour images from FLASH simulations (case 1,  $kh_{bu} \sim 0.45$ ) at different scaled times  $((t-t_{SI2})/\tau^{++})$ . Dashed line indicates the location of unperturbed free surface. (39)
- FIG. 4.2. Time evolution of (a) scaled bubble and spike amplitudes, scaled (b) bubble and (c) spike velocities from case 1. Simulation data is compared with predictions from ejecta model of [9] summarized in eqs. (1.3), (1.5), and (1.8). (41)
- FIG. 4.3. Density contour images from FLASH simulations (case 3,  $kh_{bu} \sim 0.96$ ) at different scaled times  $((t-t_{SI2})/\tau^{++})$ . Dashed line indicates the location of unperturbed free surface. (43)
- FIG. 4.4. Time evolution of (a) scaled bubble and spike amplitudes, scaled (b) bubble and (c) spike velocities from case 3. Simulation data is (45)

compared with predictions from ejecta model of [9] summarized in eqs. (1.3), (1.5), and (1.8).

- FIG. 4.5. PEAK bubble growth rates from FLASH simulations scaled with VOMB++ and plotted against the scaled initial bubble amplitude prior to second shock. Simulation data is compared with peak bubble growth rates from model of [9]. (46)
- FIG. 4.6. Shape analysis of the interface at second shock: (a) Geometric parameters associated with a flycut surface, and (b) flycut and sine profiles fitted to the pre-second shock bubble profile from case 1. (49)
- FIG. 4.7. Ejected mass from (a) case 1 and (b) case 3 compared with predictions from the mass model of [7] evaluated for sine and flycut profiles. (c) Time evolution of ejecta masses from cases 1 and 3, calculated using eq. (1.13). (51)
- FIG. 4.8. Scaled ejecta mass from all FLASH simulations plotted against the prediction from the mass model of [7], eq. (1.13). The 45 degree line indicates perfect agreement. (52)
- FIG. 4.9. (a) Schematic of the recent HE experiments conducted at LANL [17,18], with modifications to generate second shock, and (b) the scaled free-surface velocity from FLASH simulations. (54)
- FIG. 4.10 Time evolution of scaled (a) bubble and (b) spike velocities from case 4. Simulation data is compared with prediction from ejecta model of [9] summarized eqs. (1.3), (1.5), and (1.8). and experimental data from [18]. (58)
- FIG. 4.11 (a) Ejected mass from case 4 compared with predictions from mass model of [7] evaluated for sine and flycut profiles. (b) Scaled ejecta mass from case 4, compared with data from the experiments of [18]. (59)
- FIG. 5.1. Density contour images from FLASH simulations at different scaled times for an initially sinusoidal interface ( $kh_0=1/8$ ). (65)
- FIG. 5.2. Late time ( $t/\tau=13.5$ ) x-profiles of the planar-averaged mass fraction ( $\langle Y_A \rangle$ ), and the centerline scaled velocity ( $V/V_{sp}$ ) from FLASH simulation with  $kh_0=1/8$ . (66)
- FIG. 5.3. Time evolution of scaled (a) bubble and (b) spike amplitudes, and (c) corresponding absolute scaled velocities ( $V_{bu/sp}/V_0^{MB}$ ) from FLASH simulations and comparison with models. Data from  $kh_0=1/8$  sinusoidal case. (69)

FIG. 5.4. Density contour images from FLASH simulations at different scaled times for initially sinusoidal interface ( $kh_0=2$ ). Dashed line is free surface. (70)

FIG. 5.5. Time evolution of scaled (a) bubble and (b) spike amplitudes, and (c) corresponding absolute scaled velocities ( $V_{bu/sp}/V_0^{MB}$ ) from FLASH simulations and comparison with models. Data from  $kh_0=2$  sinusoidal case. (72)

FIG. 5.6. Nonlinear factors for bubble and spike ( $F_{bu/sp}^{NL}$ ) embodied in eqs. (1.6-1.7) plotted against scaled initial amplitude ( $kh_0$ ), and comparison with data from FLASH simulations. (73)

FIG. 5.7. Density contour images from FLASH simulations ( $kh_0=1/8$ ) for (a) Sinusoidal (upper panel), (b) Chevron (2nd panel), (c) Gaussian (3<sup>rd</sup> panel), and (d) Flycut (lower panel) at different scaled times. Dashed line is free surface. (78)

FIG. 5.8. Time evolution of scaled (a) bubble, and (b) spike amplitudes, and (c) bubble, and (d) spike velocities from FLASH simulations for all shapes with  $kh_0=1/8$ . Bubble velocities are scaled using eq. 1.8 [9] which is corrected for  $\lambda_{eff}$  of each shape. Spike velocities for different shapes are scaled using the asymptotic expression (eq. (5.6)). (79)

FIG. 5.9. Time evolution of scaled (a) bubble, and (b) spike amplitudes, and (c) bubble, and (d) spike velocities from FLASH simulations for all shapes with  $kh_0=2$ . Bubble velocities are scaled using eq. 1.8 [9] which is corrected for  $\lambda_{eff}$  of each shape. Spike velocities for different shapes are scaled using the asymptotic expression (eq. (5.6)). (81)

FIG. 5.10. Summary of simulations: asymptotic spike velocity ( $V_{sp}/V_0^{MB}$ ) from FLASH simulations (solid symbols), SPaSM simulations (open symbols) and models (lines) for all shapes plotted against initial amplitude ( $k_{eff}h_0$ ). (82)

FIG. 5.11. Plot of parameter beta ( $\beta$ ) as a function of initial amplitude ( $kh_0$ ) from simulations and models. (84)

FIG. 5.12. Scaled ejected mass per unit area from: (a) FLASH simulations, (b) SPaSM simulations [7] with  $kh_0=1$  for all shapes studied in this work. Dashed 45-degree line indicates model prediction evaluated using modified expression of  $\beta$  (eq. 5.3). (85)

## CHAPTER 1: INTRODUCTION AND LITERATURE REVIEW

The phenomenon of mass ejection into vacuum from a shocked metallic free surface can have a deleterious effect on the implosion phase of the Inertial Confinement Fusion [1] (ICF) process. Often, the ejecta take the form of a cloud of particles that are the result of microjetting sourced from imperfections on the metallic free surface. Similarly, stellar ejections are central to the process of mass and energy distribution associated with supernovae detonations [2-4]. Ejecta are also capable of corrupting optical and electrical measurements at metallic surfaces. Much of the recent progress in our understanding of ejecta dynamics stems from the recognition that ejecta constitute a limiting case of the shock-driven Richtmyer-Meshkov [5,6] (RM) instability problem. Also, in these applications of interest, RM instability (and the ensuing ejecta generation) is not the result of a single, but multiple incident shocks originating in the same material. This approach has led to successful models that describe several quantities of interest, including the velocities and mass. In this work, we build on these earlier efforts to (i) combine numerical simulations and data from recent experiments to characterize ejecta from second shock impact, and in the process validate a recently developed model [7,8] for mass ejection, (ii) suggest an expression for ejecta spike velocity that is accurate for large initial perturbation amplitudes imposed at the free surface, (iii) extend this expression and a previously proposed model for bubble velocities [9] to ejecta from arbitrary shapes using the approach outlined in [7], (iv) validate these models for

different initial shapes and perturbation amplitudes using an extensive suite of continuum hydrodynamics and molecular dynamics simulations, and (v) evaluate the implications of these findings to a recently proposed source model for ejecta [7,8].

While the ejecta phenomenon has been addressed extensively through experiments [10-18,9,19-23] and numerical simulations [7,24-30], the corresponding double shock problem [31] has received comparably less attention. Charakhch'an [32] numerically studied ejecta from RM instability under the influence of two successive shocks impacting a free surface of Aluminum. The first shock in their continuum model was stronger (75 GPa) with a piston velocity of 3 km/s, so that Al is in a liquid state for the second shock event ( $P_{\text{melt}}$  for Al  $\sim$  70 GPa). Recent experiments at Los Alamos National Laboratory (LANL) [18,17] reported measurements of ejecta mass from a metallic Sn target that was driven by two successive shocks generated using a high explosive (HE) driver package. Shocks of different strengths resulting in temperatures below and above the metal melt condition were investigated, while measurements included free surface velocities, ejecta mass and velocities. Such experiments in which the drive is provided by detonation of high-explosives resulting essentially in Taylor waves follow earlier efforts at LANL in which supported shock waves were generated with the use of flyer plates [10].

Ejecta development occurs in three distinct stages that are referred as “sourcing”, “transport” and “conversion”. When ejecta are generated from a shocked metallic free surface in to vacuum, the associated ‘sourcing’ and ‘transport’ phenomena can be explained in terms of the initial stages of the RM instability in the limit of infinite density ratios between the two fluids. This is reflected in the Atwood number parameter

$\left( A = \frac{\rho_B - \rho_A}{\rho_B + \rho_A} \right)$ , which approaches  $A \rightarrow -1$  in this limit. Cherne et al. [7] exploited this

analogy to propose an RM-based source model for ejecta, that is also valid for any initial perturbation shape. Similarly, “transport” refers to the flight of ejecta in the participating medium, a process that is explained through an understanding of the nonlinear bubble and spike velocities associated with the underlying RM instability. Successful ejecta transport models must acknowledge this connection, which is the approach taken in several recent articles [7,8,25,9], as well as this work. The emphasis on nonlinearities and non-sinusoidal shapes is important to interpreting experiments where the metal free surface is shocked twice in succession [18,17]. It is expected that at the time of second shock, the interface would have already evolved to a nonlinear amplitude and a non-sinusoidal shape resulting from the first shock interaction. Thus, our objective in this work is to understand how ejecta sourcing and transport are modified by the twin issues of nonlinearities and non-standard shapes, using simulations and models. The more complex issue of ejecta conversion falls outside the scope of this work.

We briefly review phenomenology and models of RM growth from a single-wavelength perturbation, before discussing recent theoretical efforts focused on modeling ejecta from machined grooves. We adopt the following terminology: the amplitudes, velocities and ejected mass associated with perturbations are denoted by  $h$ ,  $V$  and  $m$  respectively. Additional information on the state of the flow at which quantities are extracted, and the provenance of the data are provided through subscripts and superscripts. Thus, subscripts ‘0’ refers to quantities at their initial state (prior to shock impact), while ‘bu’ and ‘sp’ connote quantities associated with bubbles and spikes respectively. Superscripts provide

information on the source of data, so that quantities computed from a particular model are identified by the author(s)' initials, and data from the LANL experiments are indicated by the use of EXPT etc. Finally, we specify conditions immediately after (before) the first shock with the additional superscript '+' ('-'), while the properties immediately following (before) the second shock are denoted with the superscript '++' ('--').

### 1.1 Ejecta bubble and spike velocity models

In this work, we have evaluated several existing models for ejecta bubble and spike velocities by comparison with continuum hydrodynamics simulations using FLASH, and have suggested a modified expression for ejecta velocities motivated by the models of [33,34]. We first briefly review models for bubble and spike growth rates that are based on linear and nonlinear Richtmyer-Meshkov (RM) theory at ejecta conditions ( $A \rightarrow -1$ ). The relative scale of initial perturbations at the interface determine the subsequent RM instability-driven growth. Thus, a stage of linear growth is observed when the perturbation wavenumber ( $k \equiv \frac{2\pi}{\lambda}$ ), and the pre-shock amplitude ( $h_0^-$ ) satisfy  $kh_0^- \ll 1$ . In this regime, the initial peak growth rate immediately following the interaction of the shock with the interface is given by the impulsive model of [5] according to:

$$V_0^{RM} = kh_0^+ A^+ \Delta U. \quad (1.1)$$

In eq. (1.1),  $\Delta U$  is the interface jump velocity due to shock impulse, and  $A^+$  is the post-shock Atwood number:  $A^+ = \frac{\rho_2 - \rho_1}{\rho_2 + \rho_1}$  (Fig 1b). Note that compressibility effects are typically addressed in eq. (1.1) by taking post-shock values for the amplitude ( $h_0^+$ ) and

the Atwood number. The post-shock amplitude is obtained as  $h_0^+ = F^c h_0^-$ , where the compressibility factor  $F^c = 1 - \frac{\Delta U}{W_i}$  is computed using the incident shock speed ( $W_i$ ) and the interface velocity ( $\Delta U$ ). For  $A^+ < 0$ , Meyer-Blewett [35] suggested replacing  $h_0^+$  with the average of pre- and post-shock amplitudes  $\left(\frac{h_0^- + h_0^+}{2}\right)$ , since the interface in such heavy-to-light interactions undergoes a phase inversion. In this case, the compressibility factor becomes  $F^c = 1 - \frac{\Delta U}{2W_i}$ , so that when  $F^c$  is applied to the pre-shock amplitude, the operation returns the average of the pre- and post-shock amplitudes. The linear growth rate according to their model at  $A = -1$  is then:

$$V_0^{MB} = F^c k h_0^- \Delta U. \quad (1.2)$$

For  $kh_0^- \geq 1$  or  $kh^+(t) \geq 1$ , the resulting flow is nonlinear and eqs. (1.1) – (1.2) are no longer applicable. A physical manifestation of the nonlinear regime is the appearance of asymmetric bubble cavities and spike jets on either side of the original interface. Several nonlinear models have been proposed [33,36] to predict the asymptotic behavior of bubbles and spikes, and are based on the general potential flow approach first introduced by Layzer's [37]. Mikaelian [36] found solutions to the potential flow equations for the special case of  $|A|=1$ , by choosing appropriate velocity-potential functions in the neighborhood of bubbles, and arrived at the following analytical expression for the time-dependent ejecta bubble velocity:



$$V_{bu}^{KM}(t) = \frac{V_0}{1 + \frac{3}{2}V_0 kt}. \quad (1.3)$$

Zhang [33] extended this approach to spikes by taking the spike curvature as opposite in sign to the corresponding bubble curvature. Thus, for a sinusoidal perturbation, Zhang [33] obtains  $\xi_{\text{spike}} = -\xi_{\text{bubble}} = kh_0/2$ , leading to the following expression for the asymptotic spike velocity:

$$V_{sp}^{QZ} = V_0 \sqrt{3 \frac{kh_0 + 1}{3kh_0 + 1}}. \quad (1.4)$$

The term within the square-root in eq. (1.4) accounts for the initial condition (nonlinear) effects through the spike curvature. Mikaelian [34] extended the above model to 3D using Bessel functions.

An upper limit for the asymptotic spike velocities may be found by applying the limit  $kh_0 \ll 1$  (Mikaelian [38]):

$$V_{sp}^{KM} \rightarrow V_0 \sqrt{3}. \quad (1.5)$$

Note that in eqs. (1.3-1.5), the choice of  $V_0$  is not specified, and we must account for the possibility that the initial growth rate may itself be compromised by nonlinearities resulting from finite-sized initial perturbations ( $kh_0^- \geq 1$ ). Using perturbation analysis, Velikovich and Dimonte [39] obtained independent expressions for bubble and spike growth rate reduction factors in terms of higher-order Pade approximants (up to order 33) to capture the nonlinear modification to the initial velocity from eq (1.2). Dimonte and Ramaprabhu [40] provided a compact expression for the spike nonlinear growth rate reduction factor, as a fit to the higher order Pade approximant from [39]:

$$F_{sp}^{NL} = \frac{1}{1 + \left(\frac{kh_0^-}{2}\right)^2}. \quad (1.6)$$

Recently, Velikovich et al. [41] used high-order perturbation theory to develop an expression for a nonlinear correction factor to Richtmyer's impulsive model (eq. 1.1) for any arbitrary Atwood number. In the limit of  $A \rightarrow -1$ , their formula for nonlinear correction reduces to eq. (1.6) when higher order terms  $\left(O(kh_0^-)^3\right)$  are neglected. Buttler et al.[9] suggested a similar nonlinear correction for bubbles as a fit to the corresponding higher-order Pade approximant to the bubble growth rate from [39]:

$$F_{bu}^{NL} = \frac{1}{1 + \frac{kh_0^-}{6}}. \quad (1.7)$$

Thus, eqs. (1.7) and (1.6) are intended as prefactors to be used in eq. (1.2) to obtain the actual bubble/spike growth rate when the interface is seeded with large initial perturbations. From Buttler et al. [9], we get:

$$V_{bu0/sp0}^{WB} = F_{bu/sp}^{NL} V_0^{MB}. \quad (1.8)$$

Buttler et al. [9] further suggested using the above expression for the initial nonlinear bubble/spike growth rate as a choice for  $V_0$  in eq. (1.3) or eq. (1.5) for the corresponding asymptotic velocities.

From continuum and molecular dynamics simulations across a wide range of parameters, authors of [25] obtained the following models by fitting to observed bubble and spike growth rates:

$$V_{bu0}^{GD} = \frac{V_0^{MB}}{1 + \phi_{bu} k h_0^-}, \quad V_{sp}^{GD}(t) = |V_{bu0}^{GD}| \sqrt{\phi_{sp}^2 \frac{k h_0^- + 1}{3 M_i k h_0^- + 1}}, \quad (1.9)$$

Dimonte et al.[25] recommended using  $\phi_{bu} \sim 0.45$ ,  $\phi_{sp} \sim 2.625$  (for  $\gamma_A \sim 3$ ) to match simulation and experimental data. The above model accounts for compressibility effects through the inclusion of the shock Mach number  $M_i$  and by making  $\phi_{sp}$  dependent on the adiabatic index  $\gamma_A$ . This may well be an important effect, but is not explored in this work.

Based on these earlier efforts, and the above discussion, we highlight the following attributes for a spike velocity model:

1. A model for spike velocities should include the effects due to the initial spike curvature on the asymptotic velocity as suggested by [33].
2. In addition, the initial growth rates are also modified by nonlinearity, and this must be included through  $V_0$  separately for bubbles and spikes (e.g. eq. (1.8)).
3. In the limit of  $k h_0 \rightarrow 0$ , the asymptotic spike velocity should approach the corresponding potential flow result  $\sqrt{3}V_0$ , since both the curvature and nonlinear effects are negligible in that limit.
4. It is desirable (though not necessary) for the model to explain existing data without the use of tunable coefficients.

## 1.2 Ejecta mass models

The mass of ejecta generated at a shocked free surface depends on the missing area carved out by bubbles that have saturated in time. Thus, the bubble velocity history (eq. 1.3) and the shape of saturated bubbles determine the quantity of ejecta channeled through the spikes. A recent ejecta source model [15] is based on the above hypotheses,

and obtains the time-dependent ejecta mass from integrating the asymptotic bubble velocity from (eq. 1.3):

$$m^{WB}(t) = \frac{\rho}{\lambda} \int_0^t S_f(t) V_{bu}(t) dt = m_0 \ln \left( 1 + \frac{t}{\tau} \right). \quad (1.10)$$

In the above equation, the shape factor  $S_f$  was assumed to be unity resulting in  $m_0 = \frac{\rho\lambda}{3\pi}$

, and  $\tau = \frac{\lambda}{3\pi V_{bu0}^{WB}}$  is a time constant. Note that using  $S_f = 1$  in eq. (1.10) sets an upper

limit for the ejecta mass, and implies idealized bubble channels that are rectangular. Authors of Ref. [7] extended the above model by using a parabolic shape factor representative of real bubbles to obtain the following expression for the time evolution of ejecta mass:

$$m^{FC}(t) = \frac{\rho}{\lambda} \int_0^t \frac{4}{3} L_{bu}(t) V_{bu}(t) dt. \quad (1.11)$$

The bubble half width at the location of the free surface is denoted by  $L_{bu}(t)$  in eq. (1.11), and appears here as a result of the parabolic shape factor assumption. Enforcing conservation of volume flux across the free-surface [7] leads to an expression for  $L_{bu}$  directly in terms of bubble and spike velocities:

$$L_{bu}(t) = \frac{V_{sp}(t)\lambda}{2} \frac{1}{V_{bu}(t) + V_{sp}(t)}. \quad (1.12)$$

Inserting eq. (1.12) in eq. (1.11) and integrating over time, the following source model for ejecta mass is obtained [7]:

$$m^{FC}(t) = \frac{2}{3} m_0 \ln \left( \frac{1 + \frac{t}{\beta\tau}}{1 + \frac{\Delta t}{\beta\tau}} \right), \quad \beta = \frac{V_{bu0} + V_{sp}(t)}{V_{sp}(t)}. \quad (1.13)$$

Note that the pre-factor  $2/3$  stems from the use of the parabolic shape factor approximation for bubbles, while the parameter  $\beta$  in the logarithmic term lengthens the timescale, and is a consequence of volume flux conservation. Using the initial bubble velocity  $V_{bu0}^{WB}$  from eq. (1.8) and the asymptotic spike velocity  $V_{sp}^{KM}(t) \rightarrow V_0\sqrt{3}$  from eq. (1.5) in eq. (1.13), the following expression for  $\beta$  is obtained [7]:

$$\beta^{KM} = 1 + \frac{1}{\sqrt{3}} \frac{F_{bu}^{NL}}{F_{sp}^{NL}}. \quad (1.14)$$

In Chapter 5, we use our proposed expression for asymptotic spike velocity to evaluate the parameter  $\beta$ , and compare it with data from numerical simulations.

## CHAPTER 2: PROBLEM SETUP AND NUMERICAL METHOD

The simulations described in this work were performed using the astrophysical FLASH [42] code, developed by the FLASH center for computational sciences at the University of Chicago. The numerical method employed in FLASH is the 2<sup>nd</sup> order Piecewise Parabolic Method (PPM) to solve the Euler equations. PPM has been demonstrated [43] to be well suited to describing flows involving contact discontinuities such as sharp material interfaces and shocks. FLASH is also equipped with an Adaptive Mesh Refinement (AMR) capability, so that mesh resources are concentrated in regions of large gradients in the primary variables [44]. FLASH is a massively parallel code, with demonstrated scaling performance over hundreds of thousands of processor cores, and across multiple computing platforms. In FLASH, an ideal gas equation of state capable of handling multiple species calculates the thermodynamic properties of an ideal, gamma law fluid.

In our continuum simulations we have adopted the approach of [25] to model metallic ejecta with an equivalent  $\gamma$ -law fluid. In the instance of shock-driven jetting of material from perturbed surfaces, the response of a metal to shock loading can be described using a linear  $u_s$ - $u_p$  relation [45]:

$$u_s = c_0 + s u_p \quad (2.1)$$

Here,  $u_s$  is the incident shock speed, while  $u_p$  is the particle (piston) velocity behind the shock,  $c_0$  is the bulk sound speed in the metal, and  $s$  is a constant. Dimonte et. al [25]

estimated that for weak shocks, the relationship between the shock speed and the particle velocity in a  $\gamma$ -law fluid simplifies to:

$$u_s = \sqrt{\frac{\gamma_A P_0}{\rho_A}} + \left( \frac{\gamma_A + 1}{4} \right) u_p \quad (2.2)$$

Equation (2.2) may be taken to be the  $\gamma$ -law analog of Equation (2.1), with  $c_0 = \sqrt{\frac{\gamma_A P_0}{\rho_A}}$ ,

and  $s = \frac{\gamma_A + 1}{4}$ . By comparing parametric plots of  $P$ ,  $u_s$  and density vs.  $u_p$ , obtained from

simulations of a metal described by a Mie-Gruneisen EOS and a  $\gamma$ -law fluid, Dimonte et al. [25] concluded that the behavior of Copper under explosive loading may be approximated by an ideal fluid with  $\rho_A = 8.93 \text{ g/cm}^3$ , and  $\gamma_A = 3.0$ . Specifically, the choice of  $\gamma_A = 3.0$  was found to reproduce the hydrodynamic response of Copper (to within 7%) over the range  $u_p = 0 - 5 \text{ km/s}$ , although the temperature response was not captured due to differences in the EOS. Thus, for the continuum simulations described here, we adopt the following approach to approximate the hydrodynamic response of shock-loaded Copper. First, we estimate the incident shock speed  $u_s$  from Equation (2.2) for a particle velocity of  $u_p = 2.5 \text{ km/s}$  employed in the MD simulations. The continuum simulations were then initialized with an initial shock with strength Mach number,  $Ma \sim 2.5$  matching the shock properties used in MD. In FLASH, the light fluid was chosen to be air with  $\gamma_B = 5/3$  and  $\rho_B = 1.22 \times 10^{-3} \text{ g/cm}^3$ , while the Cu-equivalent fluid had  $\rho_A = 8.93 \text{ g/cm}^3$ , and  $\gamma_A = 3.0$ . The corresponding particle velocity from the Rankine-Hugoniot jump conditions is  $612.53 \text{ cm/s}$ . The density of the shocked region is  $15.4 \text{ g/cm}^3$ , while the corresponding release density for these conditions is  $7.57 \text{ g/cm}^3$ . Using continuum

simulations, we have investigated shock-driven jetting arising from initial perturbations with Sinusoidal, Chevron, Fly-Cut, Square-Wave and Gaussian forms (results are detailed in Chapter 3). The initial non-dimensional perturbation amplitudes employed were  $kh_0=1$  and  $1/8$  and the simulations were run to a non-dimensional timescale of  $t/\tau=65$  and  $t/\tau=44.1$  respectively. The perturbation wavelength was chosen to be  $\lambda=1$  cm for all initial waveforms. To observe the late-time nonlinear development of imposed perturbations, the 2D simulation domain had an aspect ratio of 40 for  $kh_0=1$  and 80 for  $kh_0=1/8$  (corresponding to  $t/\tau=65$  and 44.1 respectively). An Adaptive Mesh Refinement (AMR) level of 6 corresponding to an equivalent uniform mesh resolution of 256 zones /  $\lambda$  was employed in the continuum simulations.

Fig. 2.1 is a schematic of the problem configuration used in the numerical simulations reported here, where we have adopted the nomenclature suggested by Mikaelian [46] to delineate shocked and unshocked regions. The pressure in region 3, corresponding to an incident shock strength of  $Ma=2.5$ , was initialized to be  $8.9 \times 10^5$  Pa. Results for shocked Copper at these shock conditions are summarized in Chapter 3.

We have also performed simulations of ejecta production from twice shocked Tin ( $\rho_A = 7.29$  g/cm<sup>3</sup>), and compare our simulation results with target experiments of [18,17] in Chapter 4. The second shock generation technique differs slightly from the simulation setup explained earlier. Fig. 2.2 shows a typical  $x-t$  diagram for our double-shock setup, where the sequence of events in a doubly-shocked RM problem are shown. Velocities of the incident (IS) and transmitted shocks (TS), rarefactions (RR) and the interface obtained from FLASH in fig. 2.2 agree with the corresponding values from the Rankine-



Hugoniot jump conditions [46] to within 2%. Following the exit of the reflected rarefaction wave ( $RR_1$ ) from the first shock/interface interaction (event  $SI_1$  in fig. 2.2) through boundary  $x_L$ , a second shock is specified in the region occupied by guard cells at  $x \leq x_L$  in fig. 2.1(b). In many of our simulations, we manipulate the second shock arrival time at the interface (event  $SI_2$  in fig. 1(c)), to achieve specific values of the nonlinear amplitude of the interface at the instance of the second shock-interface interaction ( $kh_0^-$ ). The sinusoidal perturbations were specified according to  $h(y) = h_0 \cos(ky)$ , where  $h_0$  was the initial amplitude and was varied in our simulations. Chapter 4 details FLASH continuum simulations performed for the double-shock study as well as the procedure we have adopted to compare our simulation results with data from the target experiments of [18,17].

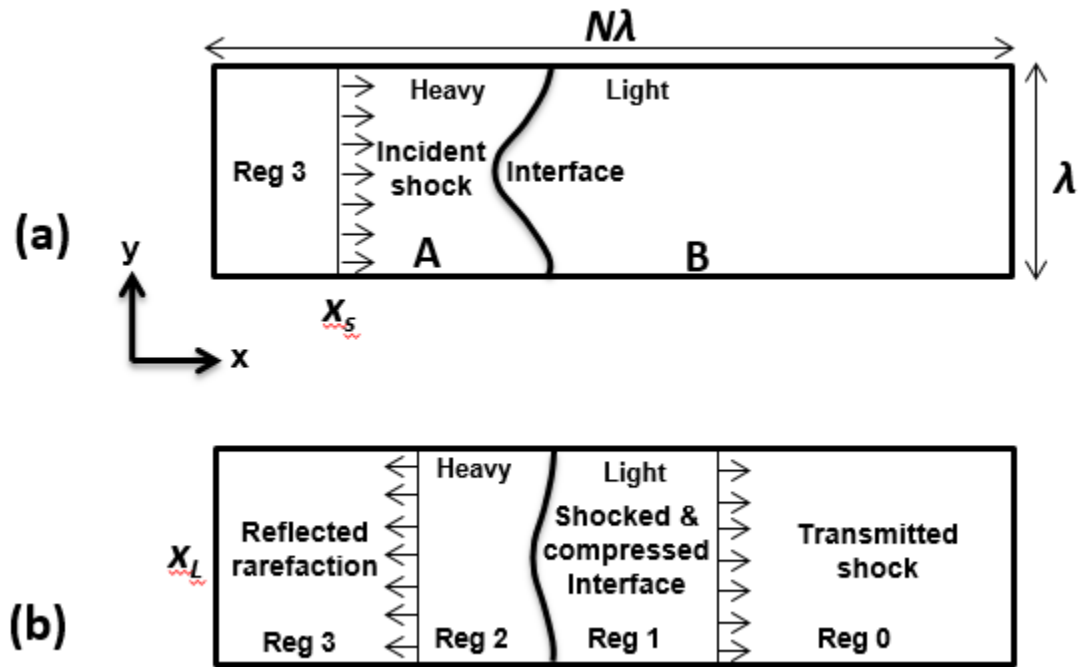


FIG. 2.1. Schematic of the computational domain showing the problem configuration and nomenclature adopted from [46]. (a) Initial condition, (b) configuration after shock-interface interaction.

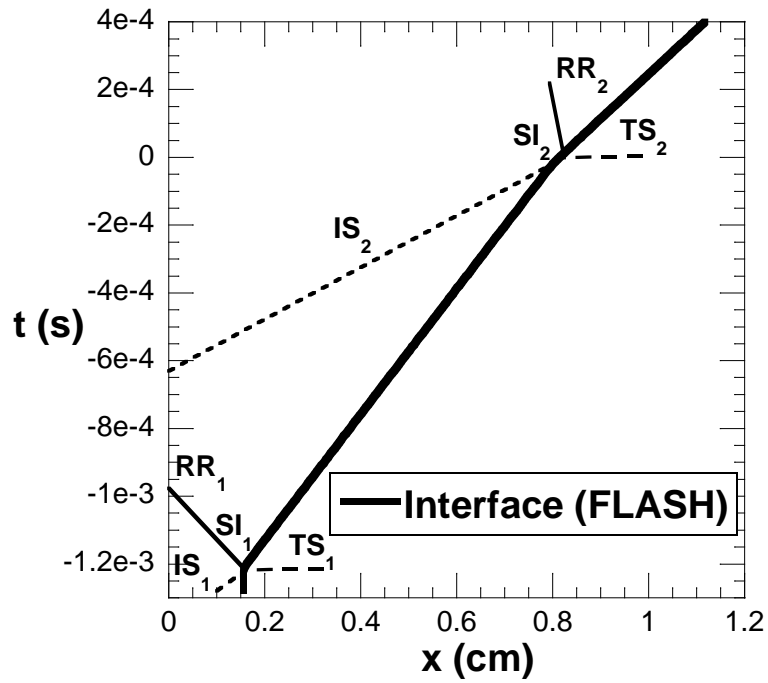


FIG. 2.2. x-t diagram from a typical second shock simulation.  $SI_1$  – first shock-interface interaction,  $TS_1$ - transmitted shock wave from first shock,  $RR_1$ - Reflected rarefaction from first shock,  $IS_1$  - Incident shock 1 and so on.

## CHAPTER 3: EJECTED MASS FROM NON-SINUSOIDAL SHAPES

In this Chapter, we discuss the effects of machining different two-dimensional shaped grooves in copper and examine the resulting flow of the material after being shocked into liquid on release. Simulations are performed using massively parallel FLASH code (detailed in Chapter 2) with machined grooves of  $kh_0=1$  and  $kh_0=1/8$ , where  $2h_0$  is the peak-to-valley height of the perturbation with wavelength  $\lambda$  and  $k=2\pi/\lambda$ . The surface morphologies studied include a Chevron, a Flycut, a Square-wave, and a Gaussian. Our findings indicate that the resulting mass can be scaled by the missing area of a sinusoidal curve with an effective wavelength,  $\lambda_{eff}$ , that has the same missing area. The mass formula proposed by authors of [7] with extension to any arbitrary shape captures the corresponding time evolution and total mass for all shapes considered here. In the following, we provide details of surfaces studied under this work.

### 3.1 Surfaces studied

Surface profiles were constructed using the expressions below. We recognize that some of these profiles may be difficult to manufacture due to their complexity, yet within the numerical simulation cell, the material ejected from these can be studied to determine isolated geometrical effects. In all of the simulations presented below the  $kh_0$  was held fixed at a value of 1 or 1/8. A value for  $h_0$  was defined as half the total height between the machined surface groove top and bottom. All shapes were constructed about the centerline axis of symmetry, as shown in Figure 3.1.

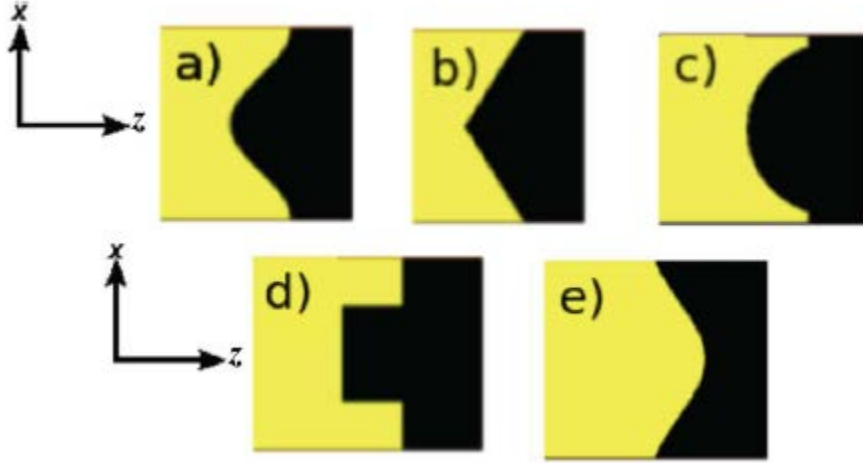


FIG. 3.1. The shapes described by these functions. a) Sinusoidal, b) Chevron, c) Fly-Cut, d) Square-Wave, and e) Gaussian.

Since the profiles are even periodic functions in  $x$  we can use a Fourier cosine series representation. The Fourier cosine series can be generalized as:

$$f(x) = a_0 + \sum_{n=1}^{\infty} a_n \cos(k_n x), \quad (3.1)$$

where  $k_n = (2\pi/\lambda)n$ . Mikaelian [47] has defined an "asymptotic-shape" that describes the RM linear growth instability of the perturbation. According to Mikaelian [47] the "asymptotic-shape" for a particular profile is related to the above Fourier series as:

$$f_{\text{asympt}}(x) = \sum_{n=1}^{\infty} k_n a_n \cos(k_n x) \quad (3.2)$$

We note that there are special cases where the above series may not converge, namely, when the  $a_n$  values decay as  $1/n$ , then  $k_n a_n$  would be a constant value, and indeed, this is the case for several of the profiles, and may be observed in the resulting surface structure.

The linear RM instability amplitude growth formula for a wavenumber  $k$  is,  $h^k(t) = h_0(1 + \Delta U k A t)$ , taking a value of -1 for solid shocked into a vacuum,  $t$  is time, and  $h_0$  is the initial sinusoidal amplitude. Applying this to each of the Fourier terms gives a shape that initially develops (with  $a_0=0$ ) as:

$$h(x, t) = \sum_{n=1}^{\infty} a_n \cos(k_n x) + \Delta U A t \sum_{n=1}^{\infty} k_n a_n \cos(k_n x) \quad (3.3)$$

It is evident that the notion of an “asymptotic shape” derives from the development of the second term on the right hand side of Equation (3.3). However, we note that this is a “linear” RM evolution, and so as a wave evolves we should expect a different shape from a cosine. Mikaelian [47] also notes that at points where there are discontinuities in the original function, “kink-singularities” form, and are affected by effects such as nonlinearity, compressibility, viscosity, surface tension, and strength.

In the following, we provide the functional representation of the surface and then its Fourier cosine series representation. In some cases, namely for the circular based profiles, the series expansion assumes particular values for the radius, wavelength, and height of the machined well. Our objective with these functions is to develop an understanding for the principal mode responsible for ejecta formation, and the resulting velocities.

#### A. Sinusoidal:

The simplest, and the standard surface used, to study Richtmyer-Meshkov instability is that of a sinusoid, namely,  $h(x) = -h_0 \cos(2\pi x/\lambda)$  and  $f_{asymp} = -h_0 k \cos\left(\frac{2\pi x}{\lambda}\right)$ . The simulation surface is shown in Figure 3.1 (a).

#### B. Chevron:

This profile could be obtained from a machining process where v-notched grooves were left in the surface. It is also one of the simpler functions for Fourier series representation, and is shown in Figure 3.1 (b). The Chevron surface is represented by a periodic representation, and its Fourier cosine series representation is given by:

$$h(x) = \frac{4h_0}{\lambda} |x| - h_0, \quad -\frac{\lambda}{2} \leq x \leq \frac{\lambda}{2} \quad (3.4)$$

and

$$h_f(x) = -\frac{8h_0}{\pi^2} \sum_{n=0}^{\infty} \frac{1}{(2n+1)^2} \cos\left(\frac{2\pi(2n+1)x}{\lambda}\right) \quad (3.5)$$

We note that in Equation (3.5) the pre-factor decays as the inverse of the square of the odd coefficients, and also that the asymptotic shape function is given by:

$$f_{\text{asympt}}(x) = -\frac{16h_0}{\pi} \sum_{n=0}^{\infty} \frac{1}{(2n+1)} \cos\left(\frac{2\pi(2n+1)x}{\lambda}\right) \quad (3.6)$$

### C. Fly-cut:

The Fly-Cut shape could be manufactured by the tip of a fly-cutter machining off material at a depth less than the radius of curvature of the machine tool tip. However, as will be evident from the results, the Fly-Cut also closely resembles the late-time evolved shape of all the shapes considered, and as such is a canonical case as an initial condition at second shock. Evaluation of the Fourier cosine coefficients for circular-based shapes is complicated because it involves evaluation of the integral:

$$a_n = \frac{2}{\lambda} \left[ \int_0^b \left( C_0 \pm \sqrt{R^2 - x^2} \right) \cos\left(\frac{2\pi nx}{\lambda}\right) dx + \int_b^{\lambda/2} h_0 \cos\left(\frac{2\pi nx}{\lambda}\right) dx \right], \quad (3.7)$$

where  $b$  is the intersection of the circle with the flat surface based on the depth of the groove, namely,  $\pm\sqrt{2Rh_0 - h_0^2}$ , and  $C_0$  is the translation along the axis of symmetry for the desired circle center. The  $a_n$  values oscillate and decay  $\sim 1/n$ . The above integral is readily evaluated numerically for a given  $\lambda$  and  $h_0$ . We evaluate the Fourier series representation of the above integral for the special case  $kh_0 = 1$  below.

This shape is perhaps the closest to a machined surface, Figure 3.1 (c). Fly-Cut machine tools consist of a cutting angle with a semicircular section at the tip. The actual functions that produce this shape are given by the following expressions:

$$\begin{aligned}
 h(x) &= h_0 & 0 \leq x \leq \frac{\lambda}{2} - b, \\
 &= R - h_0 - \sqrt{R^2 - \left(x - \frac{\lambda}{2}\right)^2} & \frac{\lambda}{2} - b \leq x \leq \frac{\lambda}{2} + b, \\
 &= h_0 & \frac{\lambda}{2} + b \leq x \leq \lambda.
 \end{aligned} \tag{3.8}$$

where  $R$  is the radius of the tip of the cutter and to generate the series,  $R = 2.2h_0$ . The Fourier cosine series is:

$$\begin{aligned}
 h(x) &= 0.140274 - 1.11995 \cos(x) + 0.162593 \cos(2x) + 0.104506 \cos(3x) - \\
 &\quad 0.126311 \cos(4x) + 0.0523246 \cos(5x) + 0.0221736 \cos(6x) - \\
 &\quad 0.0501894 \cos(7x) + 0.032069 \cos(8x) + 0.00325706 \cos(9x) \dots
 \end{aligned} \tag{3.9}$$

and

$$\begin{aligned}
 f_{asympt}(x) &= -1.11995 \cos(x) + 0.325186 \cos(2x) + 0.313518 \cos(3x) - \\
 &\quad 0.505244 \cos(4x) + 0.261623 \cos(5x) + 0.1330416 \cos(6x) - \\
 &\quad 0.3513258 \cos(7x) + 0.256552 \cos(8x) + 0.02931354 \cos(9x) \dots
 \end{aligned} \tag{3.10}$$



#### D. Square-wave:

This shape, Figure 3.1 (d), is not feasibly machined but it is interesting from a modal analysis perspective, and as a limiting case with a step as opposed to a finite gradient.

The functional representation of this shape is given by:

$$h(x) = \begin{cases} h_0 & -\lambda/2 \leq x \leq -\lambda/4 \\ -h_0 & -\lambda/4 \leq x \leq \lambda/4 \\ h_0 & \lambda/4 \leq x \leq \lambda/2 \end{cases} \quad (3.11)$$

The Fourier cosine series representation is:

$$h(x) = \sum_{n=1}^{\infty} \frac{4h_0}{n\pi} \sin\left(\frac{n\pi}{2}\right) \cos\left(\frac{2n\pi x}{\lambda}\right) \quad (3.12)$$

The Fourier coefficients decay as  $1/n$  and oscillate between positive and negative numbers. This is in contrast to the Chevron coefficients that decay as  $1/n^2$  for all odd values of  $n$ . The longer decay for a Square-Wave may contribute to regions of very high strain rates as the perturbation evolves, namely, the corners of the square well.

The "asymptotic" shape function is:

$$f_{asymp}(x) = \sum_{n=1}^{\infty} \frac{8h_0}{\lambda} \sin\left(\frac{n\pi}{2}\right) \cos\left(\frac{2n\pi x}{\lambda}\right) \quad (3.13)$$

where this expression does not converge at high values of  $n$ , but recall that this result relates to a linear analysis of the evolution.

#### E. Gaussian:

The motivation for studying a Gaussian shaped surface (Fig. 3.1(e)), was that it may best approximate a post shocked surface profile after a Richtmyer-Meshkov instability inverts.

The functional representation of a Gaussian is given by:

$$h(x) = 2h_0 e^{\left(\frac{-x^2}{2c^2}\right)} \quad (3.14)$$

where  $h_0$  and  $c$  are the height and width of the Gaussian spike respectively. Unlike the former profiles, where we have specified the functional axis to be the midpoint between the top and the bottom of the excavated well, here the axis is from the flat surface. The integration of this function to determine the Fourier coefficients is significantly simplified:

$$a_0 = \frac{2h_0 c \sqrt{2\pi}}{\lambda} \text{Erf}\left(\frac{\lambda}{2c\sqrt{2}}\right) \quad (3.15)$$

and

$$a_n = \frac{2h_0 c \sqrt{2\pi}}{\lambda} e^{-\frac{2cn^2\pi^2}{\lambda^2}} \left( \text{Erf}\left(\frac{\lambda^2 - 4ic^2 n\pi}{2c\lambda\sqrt{2}}\right) + \text{Erf}\left(\frac{\lambda^2 + 4ic^2 n\pi}{2c\lambda\sqrt{2}}\right) \right) \quad (3.16)$$

From examination of the expression in Equation (3.16) it is evident that the real portion of  $a_n$  decays as  $\sim e^{-n^2}$ , implying that the first Fourier coefficient would be the dominant mode.

### 3.2 Discussion and Results

We adopt the following approach, developed in [7] to detect the x-locations of bubble and spike extrema from our simulations. The position of the bubble tip is identified as the x-location where the planar (y-) averaged density falls below 90% of the release density- $\rho_{rel}$  following the first or second shock events. From mass conservation across the interface, the position of the free-surface may be determined from:

$$m(t) = \int_{x_{bu}(t)}^{x_{fs}(t)} (\rho_{rel} - \langle \rho(x) \rangle) dx = \int_{x_{fs}(t)}^{\infty} \langle \rho(x) \rangle dx, \quad (3.17)$$

where  $x_{bu}$ ,  $x_{fs}$  are bubble, and free-surface locations in the shock tube, while  $\langle \rho(x) \rangle$  is the planar-averaged density at  $x$ . An iterative process is then used to infer the location of the free-surface  $x_{fs}$ . We also use the LHS of Equation (3.17) to track the ejected mass  $m(t)$  from our simulations for comparison with the model described in Chapter 2.

Initial wavelengths and amplitudes for the FLASH simulations are given in Tables 3.1. Figure 3.2 shows density plots from the FLASH simulations for  $kh_0=1$  for Sinusoidal, Chevron and Square Wave profiles at non-dimensional timescale of  $t/\tau=16.77$ . We note that these FLASH results are in remarkably good agreement with corresponding results from Molecular Dynamics (MD) simulations [7] at the same non-dimensional time (albeit on different length and time scales). While the gross features between the MD and FLASH simulations are in excellent agreement, differences at the small scales are observed likely due to the absence of physical viscosity in the FLASH calculations which was present in MD.

TABLE. 3.1. FLASH simulations: (a)  $kh_0=1/8$ ,  $h_0=0.02$  cm,  $\lambda=1.0$  cm. (b)  $kh_0=1.0$ ,  $h_0=0.1592$  cm,  $\lambda=1.0$  cm.

Shape	$h_{0f}$ (cm)	$\lambda_{eff}$ (cm)	$k_{eff}$ (cm <sup>-1</sup> )
a)			
Sinusoidal	0.02	1.0	6.2832
Fly-Cut	0.0173	0.5	12.5664
Gaussian	0.0146	0.88	7.1400
Square	0.0255	1.0	6.2832
Chevron	0.0162	1.0	6.2832
b)			
Sinusoidal	0.1592	1.0	6.2832
Fly-Cut	0.1519	1.26	4.9867
Gaussian	0.1163	0.88	7.1400
Square	0.2027	1.0	6.2832
Chevron	0.1290	1.0	6.2832

Figure 3.3 shows the temporal progression of bubbles and spikes and the complex subsurface release wave structure. Figures 3.3 (a) – (f) show contours of density realized at key stages of flow evolution corresponding to non-dimensional times,  $t/\tau = 0, 1.16, 6.32, 12.76, 25.62$  and  $51.38$ , respectively. The solid black line in each figure indicates the location of the equivalent free surface, obtained from a separate simulation with  $kh_0 = 0$ . The phase reversal process expected for these  $A < 0$  simulations is clearly under way by  $t/\tau = 1.16$  (Figure 3.3 (b)), and is complete by  $t/\tau = 6.32$  (Figure 3.3 (c)). The Sinusoidal (top panel) and Chevron waveforms (middle panel) result in qualitatively similar flow structures through intermediate (Figures 3.3 (c) – (d)) and late times (Figures

3.3 (e) - (f)), since the wavenumber content of the initial conditions for each of these cases are similar.

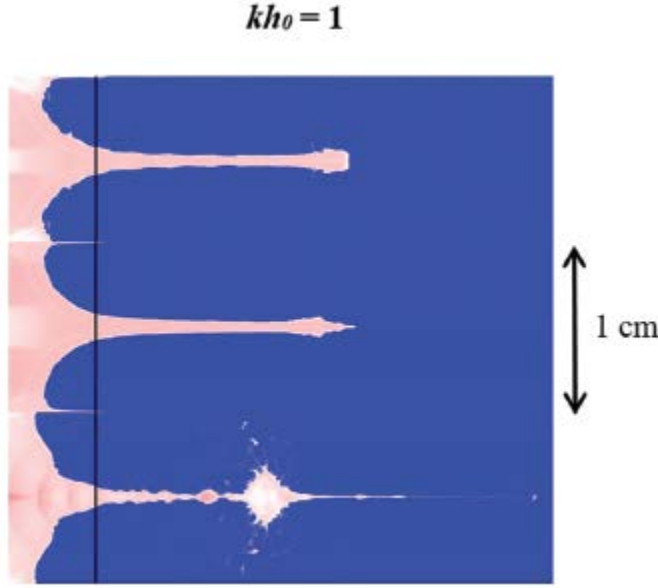


FIG. 3.2. FLASH simulations for Sinusoidal (upper panel), Chevron (middle panel) and Square-Wave (lower panel) shapes.  $kh_0=1$ ,  $t/\tau=16.77$ .

Bubble structures that are nearly flat displace the heavy fluid into long and tenuous spikes visible in Figures 3.3 (d) – (f). In contrast, simulations initialized with a square wave display more complicated structures, consistent with the presence of a broad spectrum of modes that only decay as  $1/n$  in Equation (3.12). By  $t/\tau = 51.38$ , spikes growing out of a square wave perturbation appear to be susceptible to a secondary instability seen in the bottom panel of Figure 3.3 (f).

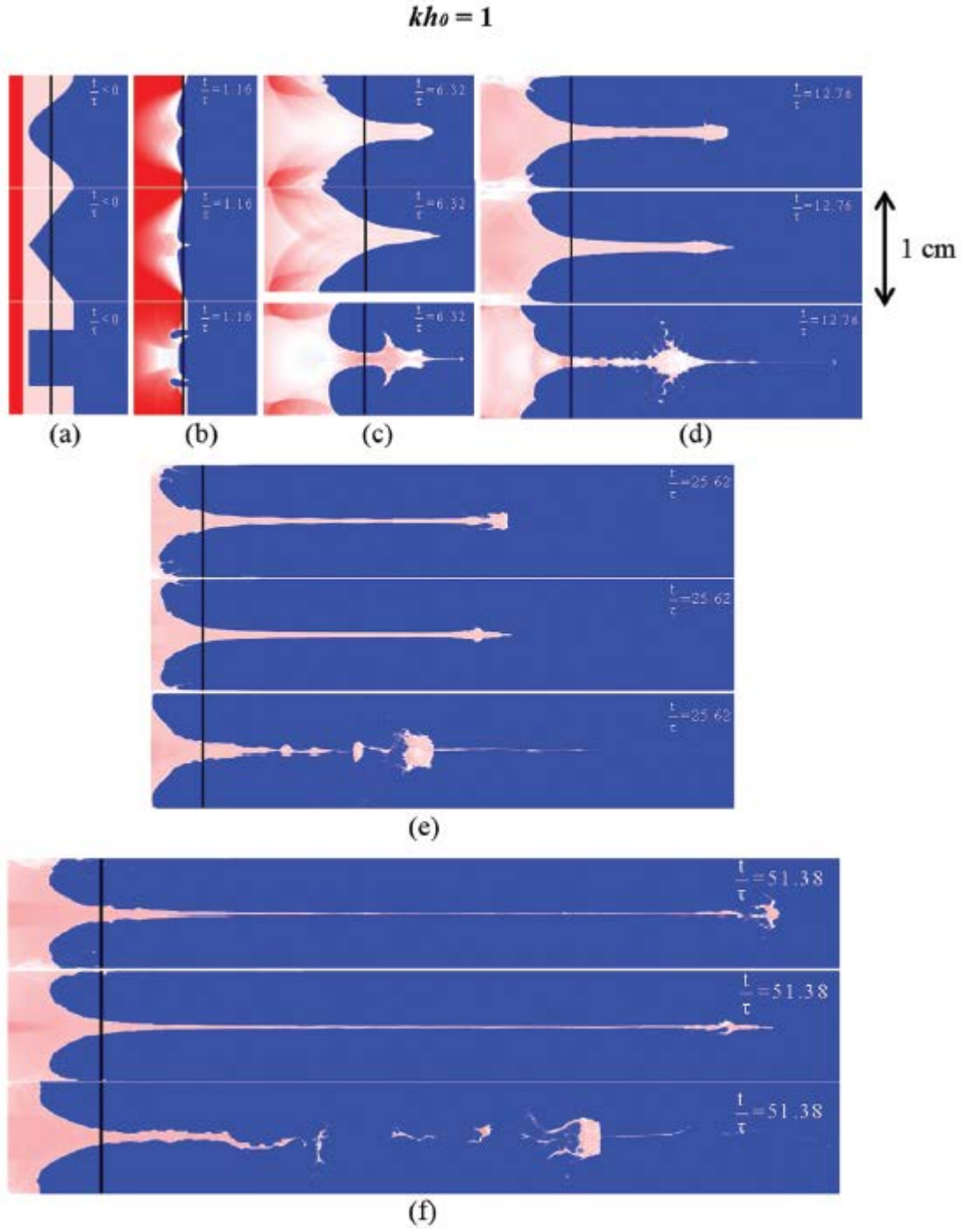


FIG. 3.3. FLASH simulations for Sinusoidal (upper panel), Chevron (middle panel) and Square-Wave (lower panel) shapes.  $kh_0=1$ ,  $t/\tau=0, 1.16, 6.32, 12.76, 25.62$ , and  $51.38$ .

Note that by  $t/\tau \sim 51.38$  (Figure 3.3 (f)), the spikes only span a few mesh cells and are thus likely to be no longer resolved structures. Thus, the breakup seen in Figure 3.3 (f) could be attributed to numerical dissipation at such small scales. Overall, the hydrodynamic simulations produce spike amplitudes that are in good agreement with the MD simulations [7] at similar values of  $t/\tau$  for the same values of  $kh_0$ . Note that at large initial amplitudes ( $kh_0 = 1$ ), both FLASH and SPaSM [7] simulations exhibit complex secondary features not observed at lower values of  $kh_0$ . These features include bubble-side ejections and blunted spike tips (figs. 3.2-3.3), and are attributed to the additional vorticity deposited at the interface at larger interfacial amplitudes due to the increased misalignment between the shock and the interface. Such features have been observed elsewhere in simulations [25] and pRad experiments [9]. The FLASH simulations were performed without surface tension ( $T$ ) and viscosity ( $\mu$ ). We believe these effects may cause modifications at the fine-scale structure of the microjetting phenomena, but do not significantly affect the integral quantities discussed in this paper. For instance, surface tension has been observed to cause jet breakup and fragmentation of spikes at late times in experiments. However, the FLASH simulations reported here have been run up to  $kV_0t \sim 50$  ( $V_0$  being the initial RM growth rate), a time period over which the surface tension driven breakup process does not advance significantly. This can be demonstrated with the following simple analysis adopted from [25]: The velocity scale associated with the spike fragmentation process can be written as  $V_{\text{jet-breakup}} \sim \sqrt{2T / \rho_2 \lambda}$  (from [48]). Using the surface tension for molten Cu ( $T \sim 1000$  dyne/cm [49]), we obtain  $V_{\text{jet-breakup}} \sim 0.03$  km/s for MD simulations, and 16.25 cm/s for FLASH simulations (if it had surface tension). For the

longest simulations in this study with  $kV_{MB}t \sim 50$ , the spike fragmentation process has only have experienced  $V_{jet-breakup} \times \frac{kV_{MB}t}{V_{MB}} \sim 1.38$  e-foldings [25] for the FLASH simulations (while the RMI has clearly proceeded to non-linearity). Thus, we do not expect the exclusion of surface tension in FLASH to significantly alter the results compared to its MD counterpart. Similarly, the model of [50] may be used to estimate the reduction in growth rate due to viscosity of molten Cu in the MD simulations relative to the continuum simulations, which were inviscid. From [50], in the presence of viscosity, the RM growth rate is modified according to

$$\dot{h} = h_0 \Delta u A_i k e^{(-2k^2 \nu t)} \quad (3.18)$$

Furthermore, the strain rates in the FLASH simulations are much lower ( $kV_0 \sim 5.6e2$  ( $3.7e3$ )  $s^{-1}$  for the  $kh_0 = 1/8$  (1) cases). It is not clear how viscosity would affect RM in the nonlinear stage, but we expect small-scale features (visible in some of the FLASH simulations) to be affected by the inclusion of viscosity.

We have used several methods to analyze the computed results. We first define an effective wavelength,  $\lambda_{eff}$ , from the area excavated out to form the initial surface perturbation,  $A_{sh}$ , by  $\lambda_{eff} = A_{sh}/h_0$ , where  $h_0$  is the half height of the peak to valley distance. Accordingly, the effective wavenumber  $k_{eff} = 2\pi/\lambda_{eff}$ . and the timescale  $\tau$  (Eq. 1.10) is given by  $\tau_{eff} = \lambda_{eff} / (3\pi \dot{\gamma}_0^b)$ . Similarly, an effective mass per unit area,  $m_{0eff}$ , is defined as,  $m_{0eff} = \rho \lambda_{eff} / 3\pi$ . It can be shown that upon integration of Equation (1.3), substituting  $k_{eff}$  in place of the  $k$ ,  $m_0$  in Equation (1.10) becomes  $m_{0eff}$ . We also define an amplitude,  $h_{of}$ , equal to the first amplitude coefficient in the Fourier series expansion.



Table 3.1 provides parameter values for the shapes considered for values of  $kh_0 = 1$  and  $1/8$ .

We start our analysis by inspecting the areal mass vs. time plots in Figures 3.4 (a) and (c) for FLASH simulations. Although all the shapes had the same initial  $h_0$  and  $\lambda$  it is evident that they produce different areal masses, with the flycut being the lowest for  $kh_0 = 1/8$  and the highest for  $kh_0 = 1$ . The model formula (eq. 1.13) suggests an areal mass scaling of  $m_0 = \rho\lambda/3\pi$ . Since  $\lambda$  is the same for all the shapes, this will not usefully scale the shapes. However, the Figures 3.4 (b) and (d), show that a scaling based on  $m_{0eff} = \rho\lambda_{eff}/3\pi$  does give a useful collapse for both  $kh_0 = 1$  and  $1/8$ . This is essentially the same scaling used by Asay and Bertholf [22]. However our model suggests an additional time scaling that is examined in the next paragraph.

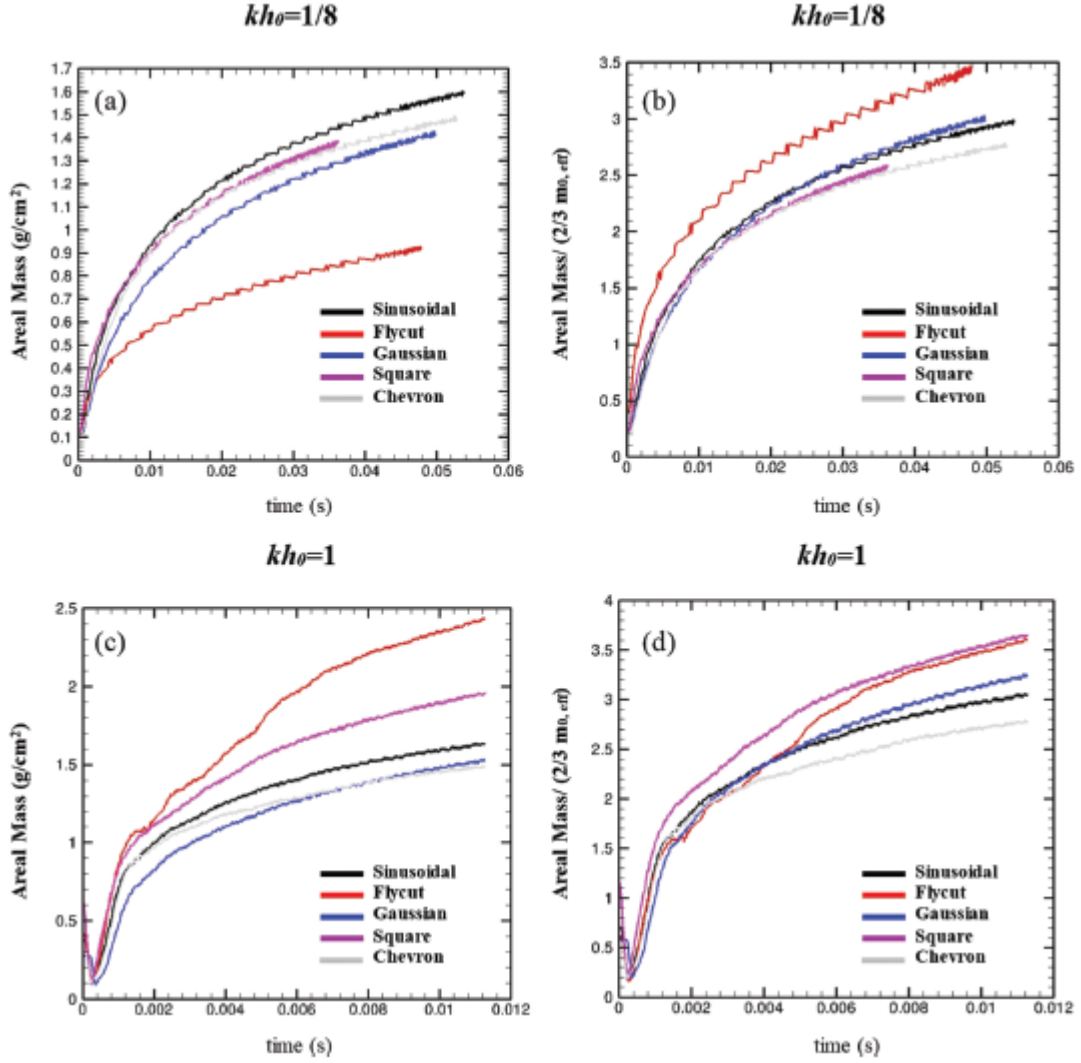


FIG. 3.4. Ejected mass per unit area for FLASH simulations. a)  $kh_0=1/8$ ,  $m(t)$  vs. time; b)  $kh_0=1/8$ , scaled mass  $m(t)/(2/3 m_{0,eff})$  vs. time; c)  $kh_0=1$ ,  $m(t)$  vs. time; d)  $kh_0=1$ , scaled mass  $m(t)/(2/3 m_{0,eff})$  vs. time.

To further assess the model given in Equation (1.13) it is necessary to specify  $\tau_{eff}$  which depends on both  $\lambda$  and  $kh_0$ . We consider two methods. The first method (I) assumes that the shape with a given peak to valley height,  $2h_0$ , may be represented by an equivalent sinusoidal perturbation with  $\lambda \rightarrow \lambda_{eff}$  and  $kh_0 \rightarrow k_{eff} h_0$ . The second method (II) assumes that at late times, the bubble growth is dominated by the longest wavelength in the

Fourier decomposition as discussed above. We thus take  $\lambda$  and  $kh_0 \rightarrow kh_{0f}$  as variables in Equation (1.13). Figure 3.5 compares these two methods for the FLASH hydrodynamic simulations. Figures 3.5 (a) and (c) show the ejecta mass per unit area scaled by  $2/3 m_{0eff}$  plotted vs. the natural logarithm on the right hand side of Equation (1.13) using method (I). Figure 3.5 (a) corresponds to  $kh_0=1/8$  and Figure 3.5 (c) to  $kh_0=1$ . Figures 3.5 (b) and 3.5 (d) are the same  $kh_0$  values using method (II). The FLASH simulations were run for approximately 12 milliseconds for  $kh_0=1$  cases ( $t/\tau \sim 65$ ), and 54 milliseconds for  $kh_0=1/8$  cases ( $t/\tau \sim 44$ ). Perfect agreement between theory and simulation corresponds to a straight line at 45 deg. in these figures. We track independently the time evolution of bubble and spike tips in our FLASH simulations, from which we obtain the timestamps of the following key events: the instance when the shock first arrives at the interface ( $T_1$ ), the time instance when the shock arrives at the valley of the perturbation ( $T_2$ ), and the instance when the interface is flat ( $T_3$ ).  $\Delta t$  is then computed as  $\Delta t = T_3 - T_1$  for use in Equation (1.13).

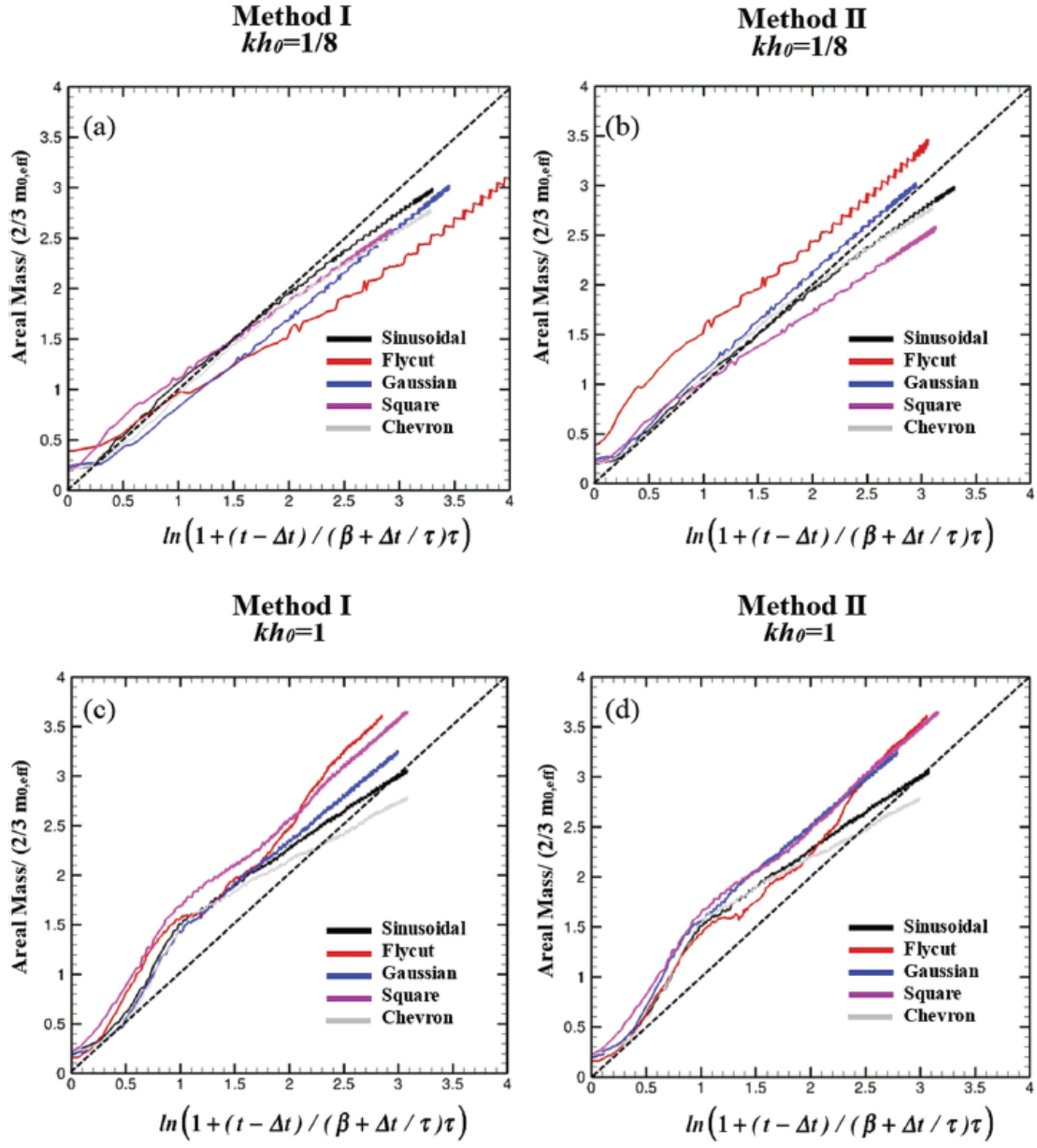


FIG. 3.5. Simulation mass per unit area compared with theoretical model, FLASH simulations. (a) and (b)  $kh_0=1/8$ : (a) Method I, (b) Method II; (c) and (d)  $kh_0=1$ : (c) Method I, (d) Method II. Dashed line—theoretical model.

Figure 3.5 reveals a reasonable agreement with the theoretical prediction using both method I and II. However one must take into account the scaling of the data and ordering of the curves shown in Figure 3.4. Referring to Table 3.1, the ordering in Figures 3.4 (a) and (c) has the highest areal mass corresponding to the largest values of  $\lambda_{eff}$ . When  $\lambda_{eff}$  is the same, the ordering is approximately according to the magnitude of  $h_{of}$ . Method I incorporates the  $\lambda_{eff}$  ordering explicitly in the pre-factor  $m_{0eff}$ . Since method I depends on the local geometry of the perturbation it may be useful for calculating the ejected mass from machined surfaces with local inhomogeneities and a distribution of surface roughness. Method II incorporates the missing area dependence in  $\tau_{eff}$  through  $h_{of}$  rather than with  $\lambda_{eff}$  and gives areal masses proportional to  $h_{of}$  in the limit that  $t \ll \tau$  which is approximately correct for the simulation data. We recommend method I because of its simplicity and its ease of generalization to non-periodic or quasi-periodic surface profiles. In Figures 3.5 (c) and (d), for  $t^* < 1$  ( $t^*$  is the x-axis coordinate in Figure 3.5  $t^* = \ln(1 + (t - \Delta t) / (\beta + \Delta t / \tau) \tau)$ ) and  $kh_0 = 1$  there is a steeper growth of areal mass release, but thereafter the areal mass release matches well with the model. This steeper release for  $kh_0 = 1$  does not occur for  $kh_0 = 1/8$  indicating that the initial inversion period does not follow the sinusoidal path suggested by the model collapse. However, the  $t^* > 1$  collapse for  $kh_0 = 1$  onto the model supports the overarching hypothesis that late-time areal mass release is controlled by the longest wavelength and initial amplitude.

## CHAPTER 4: EJECTA PRODUCTION FROM SECOND SHOCK

In this Chapter, we explore ejecta production at an interface that is impulsively accelerated by two successive shock waves using detailed numerical simulations and comparison with recent experiments. The perturbed material interface demarcates the boundary between a metal and vacuum resulting in the formation of ejecta driven by the Richtmyer-Meshkov instability. The numerical simulations were performed with the astrophysical FLASH code, in which the shocked metallic response is conceptually modeled using continuum hydrodynamics. The experimental data were obtained from a two-shockwave, high-explosive tool at Los Alamos National Laboratory capable of generating ejecta from a shocked Sn surface in to a vacuum. In both the simulations and the experiment, linear growth is observed following the first shock event, while the second shock strikes a finite-amplitude interface leading to nonlinear growth. The timing of the second incident shock was varied systematically in our simulations to realize a finite-amplitude re-initialization of the RM instability driving the ejecta. We take advantage of the nonlinear growth following the second shock, to evaluate a recently proposed model for sourcing of mass in ejecta formation that accounts for shape effects through an effective wavelength. In particular, we find the agreement between simulations, experiments and the mass model is improved when such shape effects associated with the interface at the instance of second shock are incorporated. The

approach outlined here of combining continuum simulations with validated nonlinear models can aid in the design of future experimental campaigns.

#### 4.1 Ejecta simulations ( $A \rightarrow -1$ cases)

In this section, we present results from our double shock simulations at ejecta conditions with molten ‘Sn’ modeled as an ideal  $\gamma$ -law fluid using the methodology outlined in Chapter 2. At these conditions, pre- and post-shock Atwood numbers differ only slightly so that  $A^- \sim A^+ \sim -1$ . In many of our simulations, the interface has evolved to a nonlinear state at the instance of second-shock arrival, so that the subsequent evolution of bubbles and spikes will be described by nonlinear models such as eqs. (1.3), (1.5), and (1.8). We also report on the evolution of ejected mass from successive shock events, and compare our numerical results with a recently developed ejecta source model [7] (eq. 1.13).

Table 4.1 provides a listing of FLASH simulations performed in this study at  $A \rightarrow -1$ , with corresponding values of first ( $Ma_1$ ) and second shock ( $Ma_2$ ) strengths, initial perturbation forms and interfacial amplitudes ( $kh_0^{--}$ ) immediately prior to second shock event. Note that all the cases in Table 4.1 were initialized with a scaled interfacial amplitude of  $kh_0^- = 0.12$  prior to the first shock, ensuring the initial perturbation growth occurs within the linear RM regime governed by eq. (1.2). In contrast, the time of arrival of the second shock was varied to realize perturbed interfaces of different amplitudes at the instance of second shock impact.

TABLE 4.1. Summary of FLASH simulations ( $A \rightarrow -1$ )

Case	First shock Mach number	Second shock Mach number	Scaled bubble amplitude before second shock ( $kh_{bu}^-$ )
1	1.6	1.3	0.45
2	1.6	1.3	0.75
3	1.6	1.3	0.96
4	1.53	1.2	0.5

In Figure 4.1, we plot density contours from case 1 corresponding to different values of the non-dimensional time [7]  $\frac{t-t_{SI_2}}{\tau^{++}}$ . Note that  $t_{SI_2}$  refers to the time of second shock impact, while  $\tau^{++}$  is used as defined in the context of equation (1.13), but evaluated for second shock conditions. The initial sinusoidal perturbation with  $kh_0^- = 0.12$  is shown in Figure 4.1 (a), with the incident Mach 1.6 shock located upstream at  $x = x_s$ , while the location of the corresponding unperturbed interface (obtained separately from a simulation with  $kh_0^- = 0$ ) is depicted by the dashed line. Following shock impact (SI<sub>1</sub> in Figure 2.2), the interface in our simulations is compressed to a post-shock amplitude of  $\sim 0.05$ , in agreement with  $kh_0^+ = \chi kh_0^- = 0.055$ , where  $\chi \equiv \frac{h_0^+}{h_0^-} = 1 - \frac{\Delta U^+}{W_i^-} \sim 0.45$  is an amplitude compression factor and  $W_i^-$  is the incident first-shock speed. The reflected rarefaction from the shock-interface interaction decompresses material A from an initial density of 7.29 g/cm<sup>3</sup> to a final ‘release’ density  $\rho_{rel}^+ \sim 7.073$  g/cm<sup>3</sup>. Since the shock



passage is from a heavy-to-light medium with  $\Delta U^+ < W_i^-$ , an ‘indirect’ phase inversion [51] is observed in Figure 4.1 (b), where erstwhile bubbles (spikes) have inverted to form spikes (bubbles). Figure 4.1 (c) shows the interface has achieved a scaled bubble amplitude of  $kh_{bu}^{--} \sim 0.45$  at  $\frac{t-t_{SI_2}}{\tau^{++}} \sim 0$  prior to second shock impact. The sequence of events following the interaction of the interface with the Mach 1.3 second shock (SI<sub>2</sub>) is shown in Figures 4.1 (d) – (g). The second shock compresses the interface to a post-shock bubble amplitude of  $kh_{bu}^{++} \sim 0.3$ , consistent with the compression factor  $\chi \equiv \frac{h_0^{++}}{h_0^{--}} = 1 - \frac{\Delta U^{++}}{W_i^{--}} \sim 0.65$  evaluated for conditions of the second shock interaction. The rarefaction from the second shock results in further decompression of fluid A to  $\rho_{rel}^{++} \sim 7.0442 \text{ g/cm}^3$ . This is followed by a second phase inversion (since  $A^{++} < 0$ ), which leads first to a flat interface at  $\frac{t-t_{SI_2}}{\tau^{++}} \sim 2.2$  (Figure 4.1 (d)) and to the restoration of bubbles and spikes to their original y-positions by  $\frac{t-t_{SI_2}}{\tau^{++}} \sim 3.3$  (Figure 4.1 (e)). Note that the momentary flattening of the interface in Figure 4.1 (d) implies the bubble surface recovers the ejected mass from the first shock interaction that has been fed to the spikes. At late times (Figures 4.1(f) – (g)), the twice-shocked interface goes through a nonlinear saturation, marked by the emergence and dominance of higher harmonics as well as bubbles and spikes acquiring distinct shapes - the bubbles appear to flatten, while the spikes are concentrated into long and narrow jets of the heavy fluid penetrating the light. As the mature bubbles feed mass in to the spikes, mass conservation dictates that the

spikes become progressively narrower while their amplitudes increase linearly with time according to eq. (1.5). Thus, we terminate our simulations at late times when the spikes span merely a few mesh cells, and are thus susceptible to dissipation by numerical viscosity.

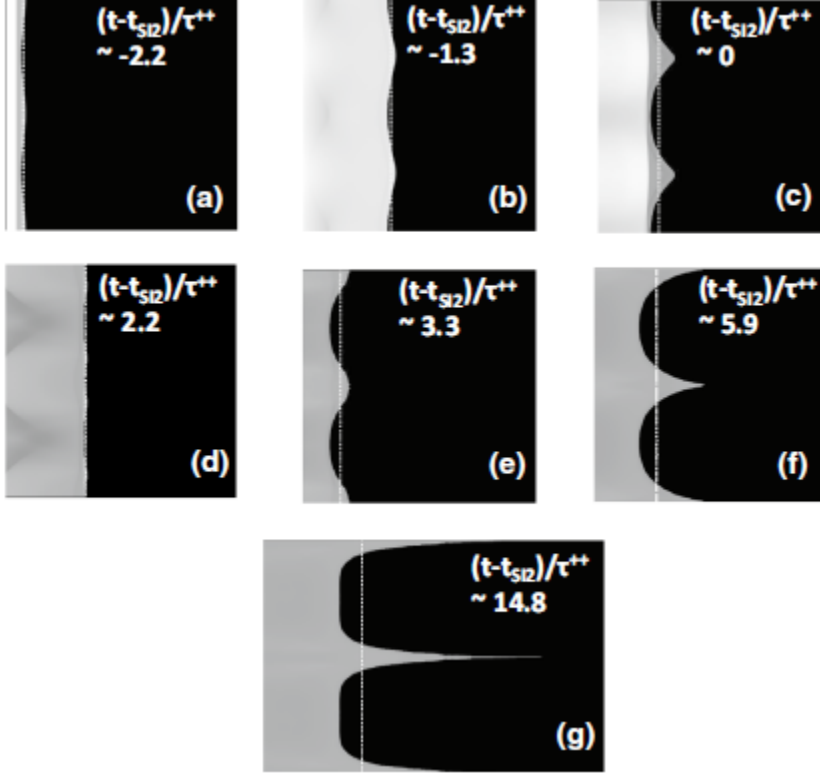


FIG. 4.1. Density contour images from FLASH simulations (case 1,  $kh_{bu} \sim 0.45$ ) at different scaled times  $((t-t_{s12})/\tau^{++})$ . Dashed line indicates the location of unperturbed free surface.

The spike locations, namely  $x_{sp}$  are computed as 1% of planar (y-) averaged mass fraction of heavy fluid, a measure that was found to be a robust predictor based on comparisons with density contours as well as velocity profiles along the length of the spike.

In Figure 4.2 (a), we plot bubble and spike amplitudes scaled by the perturbation wavenumber  $k$ , and as a function of the scaled time  $(\frac{t-t_{SI_2}}{\tau^{++}})$  from a doubly-shocked simulation (case 1) using the techniques described above. The associated bubble and spike velocities are scaled with the prediction from the Meyer-Blewett [35] impulsive model evaluated for second-shock conditions  $(V_0^{MB++})$ , and plotted in Figure 4.2 (b) – (c). The heavy-to-light shock transition ( $A < 0$ ) sets up a phase inversion clearly visible in Figure 4.2 (a), as bubble (solid line) and spike (dashed line) amplitudes grow negatively from their initial values in each case. As predicted by eq. (1.3), bubble amplitudes appear to saturate at late times, while the spikes grow linearly in time with a terminal velocity.

The corresponding bubble velocity in Figure 4.2 (b) achieves short-lived peaks following the first and second shock events at  $\frac{t-t_{SI_2}}{\tau^{++}} \sim -1$  and  $\sim 0$  respectively, before entering a prolonged period of decay consistent with eq. (1.3). Following first shock, the maximum

bubble velocity (at  $\frac{t-t_{SI_2}}{\tau^{++}} \sim -1$ ) from the simulation satisfies eq. (1.8) to within 5%,

provided we take  $F^{L+} = 1 - \frac{\Delta U^+}{2W_i^-} \sim 0.73$ , and  $F_{bu}^{NL+} = \frac{1}{1 + \frac{kh_0^-}{6}} \sim 0.98$ . Similarly, the

maximum bubble velocity following second shock impact (at  $\frac{t-t_{SI_2}}{\tau^{++}} \sim 0$ ) is within 5% of

eq. (1.8), if  $F_{bu}^{NL++}$  is calculated using  $kh_{bu}^{--} \sim 0.45$ , the bubble amplitude immediately preceding shock arrival. The ensuing time-dependent bubble decay in Figure 4.2 (b)

(dashed line) is in excellent agreement with the  $\sim \frac{1}{V_{bu_0}^{WB++} kt}$  trend line predicted by eq.

(1.3) through late times. As spikes continue to narrow, they reach a constant, terminal velocity seen in Figure 4.2 (c). The dashed line in Figure 4.2 (c) indicates the terminal velocity obtained by spikes given by eq. (1.5). Note that the Meyer-Blewett growth rate

$V_0^{MB++}$  in eq. (1.8) is calculated using the bubble amplitude  $(kh_{bu}^{--})$  at the time of second shock. Thus, evaluating  $F_{sp}^{NL++}$  in eq. (1.8) with  $kh_{sp}^{--} \sim 1$ , we obtain

$V_{sp_0}^{WB++} \sim 0.8V_0^{MB++}$  and an asymptotic scaled spike velocity of  $\frac{V_{sp}(t \rightarrow \infty)}{V_0^{MB++}} \sim 1.4$  in good

agreement with eq. (1.5) in Figure 4.2 (c).

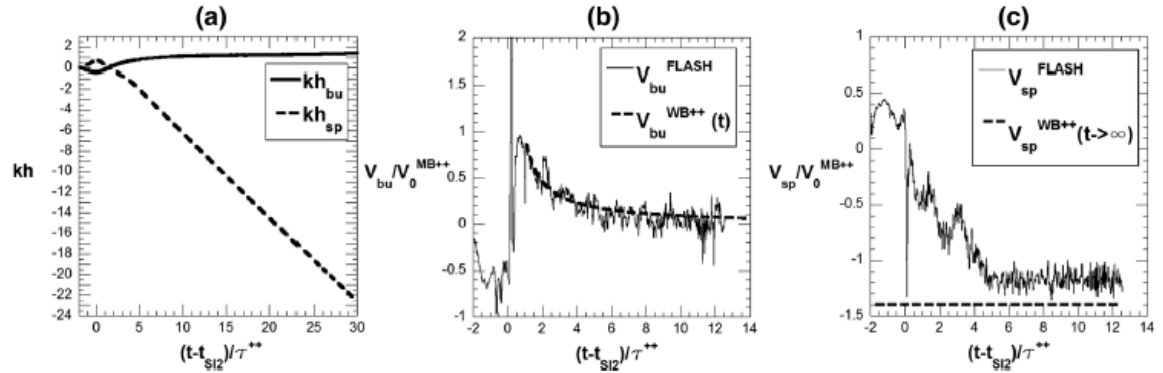


FIG. 4.2. Time evolution of (a) scaled bubble and spike amplitudes, scaled (b) bubble and (c) spike velocities from case 1. Simulation data is compared with predictions from ejecta model of [9] summarized in eqs. (1.3), (1.5), and (1.8).

In Figures 4.3 (a) – (g), we plot density contours from case 3, in which the second shock

was delayed so that the bubble amplitude prior to  $SI_2$   $\left(\frac{t-t_{SI_2}}{\tau^{++}} \sim 0\right)$  was nonlinear and

approaching  $kh_{bu}^{--} \sim 0.96$ . At the instant of second shock arrival, corresponding spikes

have matured to a nonlinear amplitude of  $kh_{sp}^{--} \sim 2$  and are shown in Figure 4.3 (c). Thus, the finite amplitudes of bubbles and spikes at second shock suggest this is a robust test case for nonlinear, analytical growth models such eqs. (1.3), (1.5), and (1.8). Second shock compression reduces the post-shock bubble amplitudes from  $kh_{bu}^{--} \sim 0.96$  to  $kh_{bu}^{++} \sim 0.63$  ( $\chi \sim 0.65$ ), before triggering another indirect phase inversion evident in Figures 4.3 (c) - (d). In contrast to the low amplitude case discussed earlier, the ejecta remnants from the first shock event are visible on the newly formed second shock bubble surface (Figures 4.3 (d) – (e)). At late times (Figures 4.3 (f) – (g)), such secondary features on the bubble tips recede due to the ongoing phase inversion followed by localized mean transport away from the bubble tip, leaving behind a clean, rounded bubble surface that is excavating and redirecting mass into long, pointed spike jets.

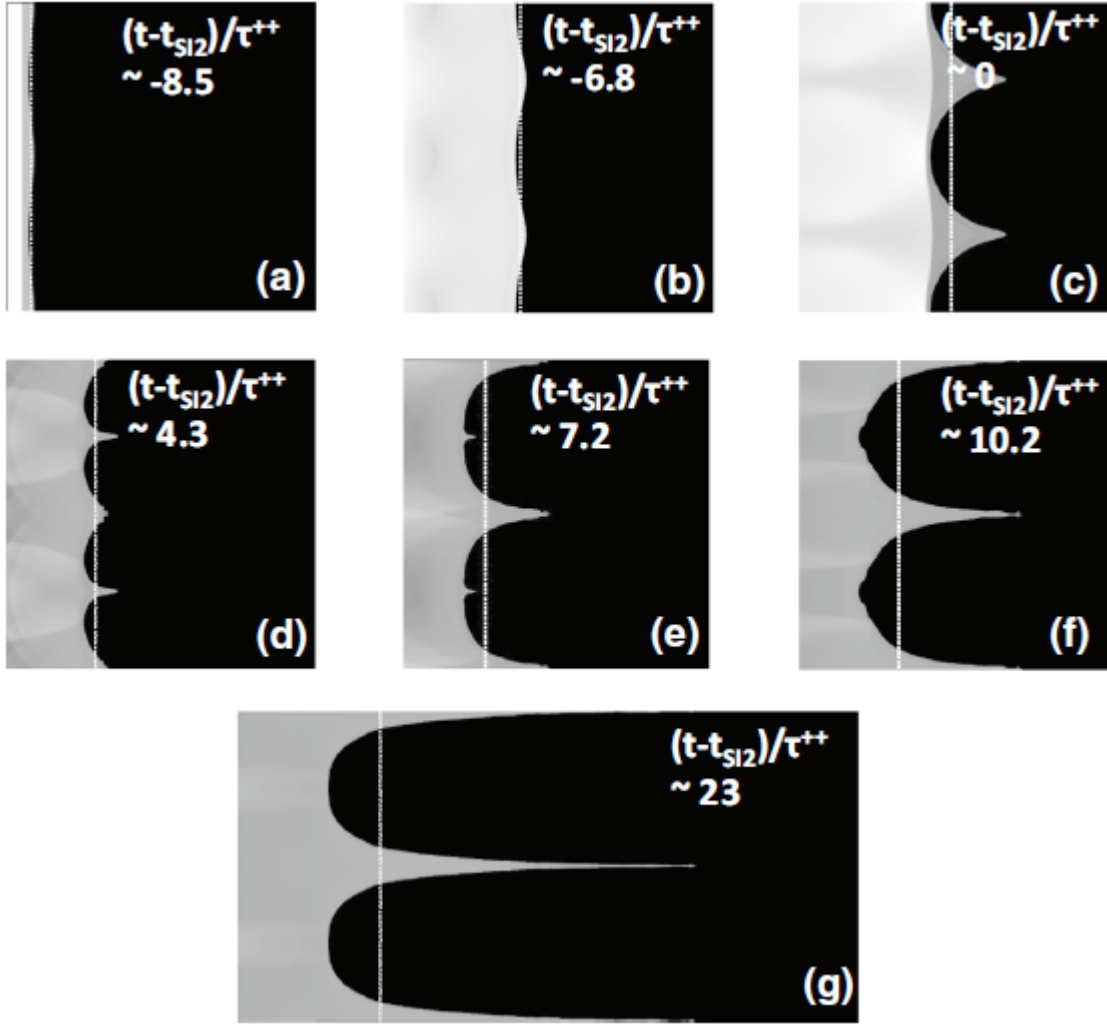


FIG. 4.3. Density contour images from FLASH simulations (case 3,  $kh_{bu} \sim 0.96$ ) at different scaled times  $((t-t_{SI2})/\tau^{++})$ . Dashed line indicates the location of unperturbed free surface.

Quantitative data from this case includes the time evolution of scaled bubble and spike amplitudes (Figure 4.4 (a)) and corresponding scaled velocities in Figures 4.4 (b) – (c). Similar to the low amplitude case discussed earlier, bubble and spike amplitudes from case 3 undergo sign reversals following each shock in Figure 4.4 (a). At late times, bubble amplitudes saturate to  $kh_{bu} \sim 2$ , compared to a saturation amplitude of  $kh_{bu} \sim 1.5$

for case 1. This trend is consistent with the observation in [25] that the eventual saturation amplitudes of bubbles  $(kh_{bu}(t \rightarrow \infty))$  depends (linearly) on the average of the pre- and post-shock initial perturbation amplitudes. Bubble and spike velocities from case 3 are depicted in Figures 4.4 (b) - (c), and show behavior predicted eqs. (1.3), (1.5), and (1.8). For instance, eq. (1.8) suggests the scaled peak bubble velocity should satisfy

$$V_{bu_0}^{WB+} / V_0^{MB+} = F_{bu}^{NL+}. \text{ Prior to its interaction with the second shock, the interface acquires}$$

an amplitude of  $kh_{bu}^{--} \sim 0.96$ , so that  $F_{bu}^{NL++}$  evaluates to  $\sim 0.86$ , compared to the observed peak of  $\sim 0.84$ . The subsequent decay of bubble velocity from our simulations also appears to be captured by eq. (1.3), which is an extension of eq. (1.8) to capture the time-dependence. Similarly, according to eqs. (1.8), (1.5) spikes must have an initial

$$\text{velocity of } V_{sp_0}^{WB+} / V_0^{MB+} = F_{sp}^{NL+} \text{ which will increase to a terminal velocity of } \sqrt{3} V_{sp_0}^{WB+}.$$

As before using  $kh_{sp}^{--} \sim 2$ , the terminal spike velocity of  $\frac{V_{sp}^{WB++}(t \rightarrow \infty)}{V_0^{MB++}} \sim 0.9$  is in good

agreement with simulation data in Figure 4.4 (c).

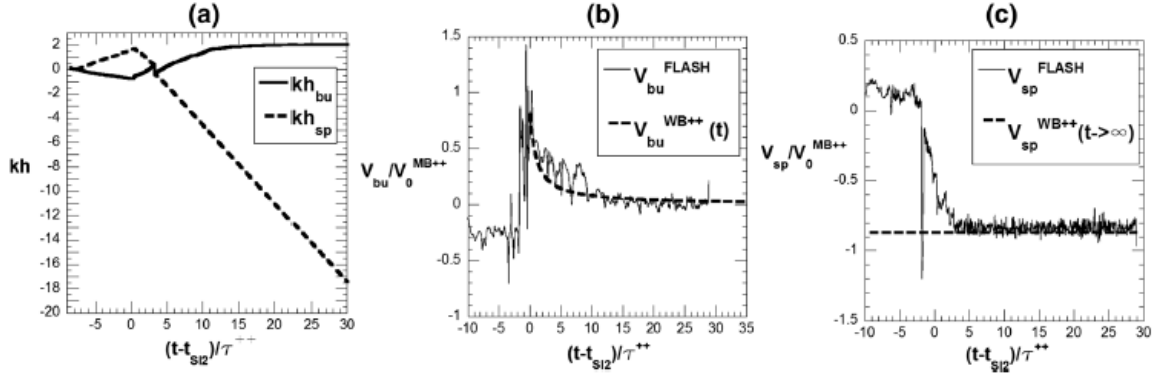


FIG. 4.4. Time evolution of (a) scaled bubble and spike amplitudes, scaled (b) bubble and (c) spike velocities from case 3. Simulation data is compared with predictions from ejecta model of [9] summarized in eqs. (1.3), (1.5), and (1.8).

We summarize bubble peak velocities from all the simulations in Figure 4.5, where we

plot  $V_{bu_0}^{++} / V_0^{MB++}$  obtained immediately after  $SI_2$  as a function of the corresponding scaled

bubble amplitude  $(kh_{bu}^{--})$ . The dashed line indicates prediction from eq. (1.8) and thus

corresponds to  $F_{bu}^{NL+}$  evaluated for the range of pre-second shock amplitudes. From

Figure 4.5, the nonlinear decay factor for bubbles  $(F_{bu}^{NL+})$  is in excellent agreement with

the simulation data. This is particularly important as the bubble velocity following  $SI_2$  features prominently in the determination of the ejected mass according to eq. (1.13).

Note that the nonlinear factors  $(F_{bu/sp}^{NL+})$  were also independently proposed in [41].



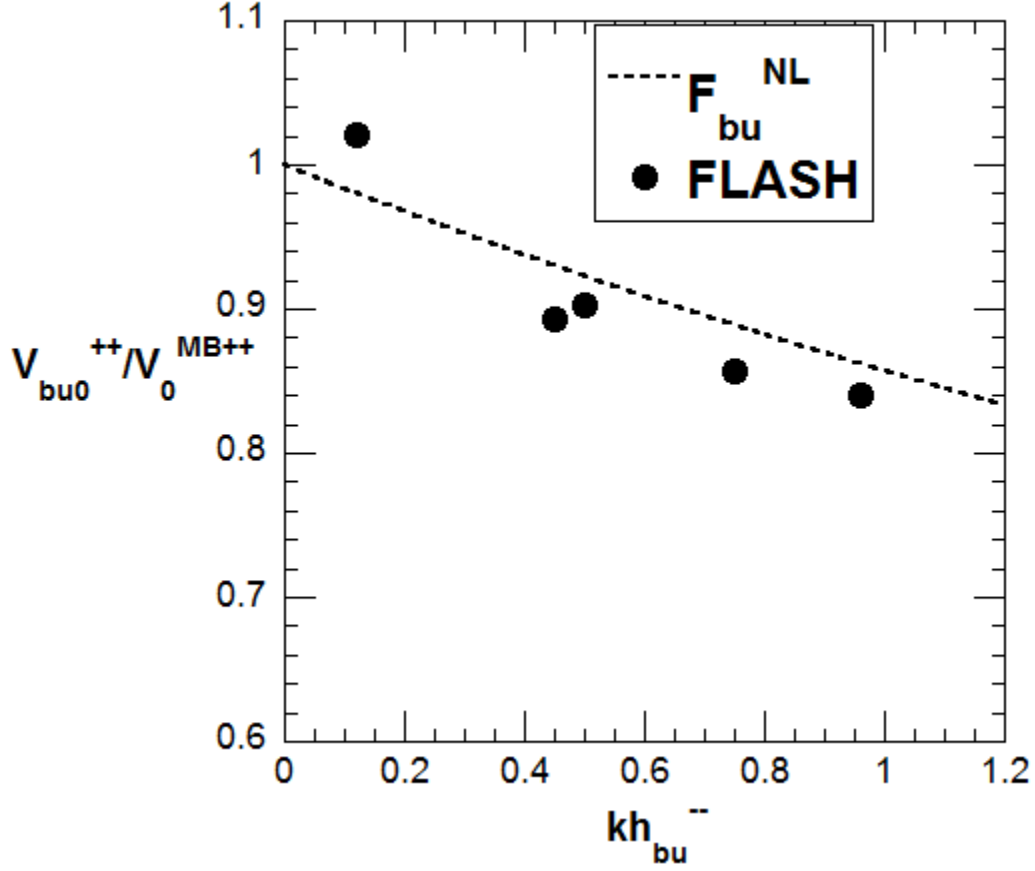


FIG. 4.5. PEAK bubble growth rates from FLASH simulations scaled with  $V_0^{MB++}$  and plotted against the scaled initial bubble amplitude prior to second shock. Simulation data is compared with peak bubble growth rates from model of [9].

#### 4.2 Bubble Surface Shape Analysis

The shape of the bubble surface prior to second shock is of particular importance since it sources the mass that is fed in to the spikes. After examining several candidate shapes, we find the nonlinear bubble surface prior to the second phase inversion (Figures 4.1 (c), 4.3 (c)) most closely resembles a ‘flycut’ profile with a phase-shift of  $\pi$  from the original sinusoid. The authors of [7] reported that eq. (1.13) successfully predicts the ejected mass from different shapes if the effective wavelength  $\lambda_{eff}$  associated with each

shape is used in that equation. In this article, we follow a similar approach in describing the bubble surface just before second shock as a flycut with an effective wavelength that is used in eq. (1.13) to compute the ejected mass. We find the difference in missing areas for bubbles associated with a sinusoid and a flycut is significant, and is a source for additional mass ejection in the case of the flycut.

To account for the additional missing area available for mass ejection, we first attempt to fit a flycut profile to the bubble immediately preceding the second shock. A flycut surface can be defined with three independent parameters, the amplitude  $h_0$ , the wavelength  $\lambda$  and the radius  $R$  using the equation

$$\begin{aligned}
 h(x) &= h_0 & 0 \leq x \leq \frac{\lambda}{2} - b, \\
 &= R - h_0 - \sqrt{R^2 - \left(x - \frac{\lambda}{2}\right)^2} & \frac{\lambda}{2} - b \leq x \leq \frac{\lambda}{2} + b, \\
 &= h_0 & \frac{\lambda}{2} + b \leq x \leq \lambda.
 \end{aligned} \tag{4.1}$$

In Equation (4.1),  $b = \sqrt{R^2 - (R - 2h_0)^2}$  is the length of the chord that signifies the intersection of the circle with the flat surface (Figure 4.6 (a)). Such shapes are generated in practice by a fly cutter milling tool frequently used in face milling operations. In Figure 4.6 (b), we attempt to construct a flycut with  $(h_0, \lambda, R)$  that match corresponding properties associated with the mature bubble surface just before it is impacted by the second shock. From Figures 4.6 (a) – (b), it is clear that  $2(L_{bu} + L_{sp}) = \lambda$ , where  $L_{bu}$  ( $L_{sp}$ ) is the half width of the bubble (spike). Similarly, we define the flycut amplitude  $h_0 = h_{bu}$ ,

the bubble height relative to the position of the free surface in our simulation. From the geometry of the flycut, this leads to

$$R = \frac{1}{2} \left( h_{bu}^{--} + \frac{L_{bu}^{--2}}{h_{bu}^{--}} \right), \quad (4.2)$$

thereby defining a profile based on the independent parameters  $(h_{bu}, L_{bu}, L_{sp})$  that match the bubble surface properties. The thick-dashed line in Figures 4.6 (b) shows the profile so constructed to match the interface (solid-thin line), and the  $R^2$  fit with the underlying bubble shape is 0.99. The corresponding sine wave fit is shown as the dotted line in Figures 4.6 (b), and clearly undercounts the bubble mass available for ejection ( $R^2 = 0.86$ ). An effective wavelength for the flycut may then be defined as  $\lambda_{eff} = \frac{A_{shape}}{h_{bu}^{--}}$ , where

$A_{shape}$  is the missing area associated with that shape and obtained as the area enclosed by the circular arc and the chord with length  $2b$  in Figures 4.6 (a). From the geometry of Figures 4.6 (a),  $A_{shape} = \theta R^2 - b(R - 2h_0)$ , where  $\theta = \sin^{-1} \frac{b}{R}$ . A summary of bubble surface profiles and corresponding flycut parameters is provided in Table 4.2 for all the simulations considered in this study.

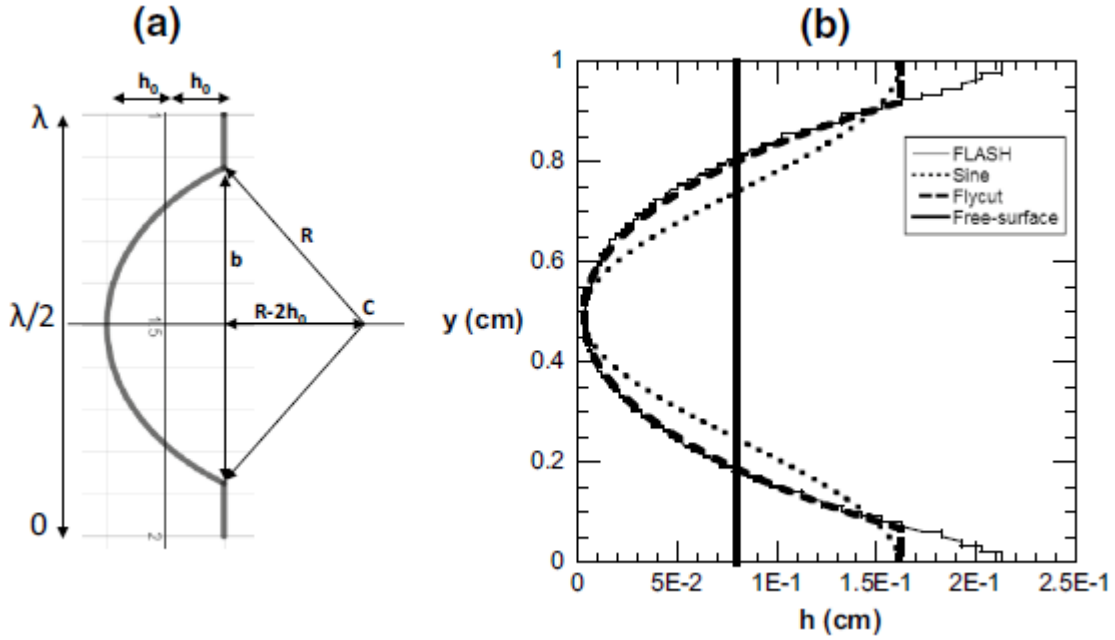


FIG. 4.6. Shape analysis of the interface at second shock: (a) Geometric parameters associated with a flycut surface, and (b) flycut and sine profiles fitted to the pre-second shock bubble profile from case 1.

TABLE 4.2. Geometric properties of the interfaces at second shock from FLASH simulations.

Case	Scaled bubble amplitude ( $kh_{bu}^-$ ) before second shock	Bubble half width ( $L_{bu}^-$ ) at second shock (cm)	Radius (R) (cm)	Chord length (b) (cm)	$\lambda_{eff}$ (cm)
1	0.45	0.300	0.664	0.412	1.125
2	0.75	0.335	0.530	0.443	1.246
3	0.96	0.336	0.446	0.423	1.242
4	0.5	0.300	0.651	0.411	1.12

The time evolution of ejected mass from case 1 is shown in Figure 4.7 (a), along with predictions from eq. (1.13) for different shapes. The mass from the FLASH simulations  $m^{FLASH}(t)$  is computed from planar-averaged density profiles using eq. (3.17). We also plot  $m^{FC}(t)$  from eq. (1.13), evaluated separately for  $\text{sine}(\lambda_{eff} = \lambda)$  and flycut

$(\lambda_{eff} = 1.125\lambda)$  shapes. The time axis is origin-shifted by  $t_{SI_2} + \Delta t^{++}$ , where  $\Delta t^{++}$  is the time interval between second shock breakout at the perturbed interface and the instant when the interface is rendered completely flat. Figure 4.7 (a) reveals ejecta mass from our double-shock simulations are in excellent agreement with the model of [7] following both first and second shocks, particularly when eq. (1.13) is evaluated for a flycut shape with consistent  $\lambda_{eff}$ . Note that the second phase inversion leads to a momentary flattening of the interface (see Figure 4.1 (d) for instance), resulting in a partial recovery of the mass ejected from the first shock. Subsequently, the RM growth from the second shock releases additional mass from the newly formed bubble surface through long and directed spikes. The higher value of  $\lambda_{eff}$  associated with the flycut increases  $m_0^{++}$  in eq. (1.13) to  $\sim 0.84 \text{ g/cm}^2$  (from  $\sim 0.74 \text{ g/cm}^2$  for a corresponding sinusoid), while increasing  $\tau^{++}$  from  $\sim 1.0\text{e-}3 \text{ s}$  to  $\sim 1.3\text{e-}3 \text{ s}$ . The results from case 3 ( $kh_0 \sim 1$ ) are plotted in Figure 4.7 (b), and show a similar trend to the lower amplitude simulation discussed above. Due to the larger initial amplitudes, the bubble surface prior to  $SI_2$  encompasses significantly more missing area. As a result, the higher value of  $\lambda_{eff}$  increases  $m_0^{++}$  used in equation (1.13) from  $\sim 0.74 \text{ g/cm}^2$  (sine) to  $\sim 0.93 \text{ g/cm}^2$  (flycut) which shows better agreement with the FLASH data. Thus, when the mass history from the model eq. (1.13) ( $m^{FC}(t)$ ) is plotted with corrections for a flycut shape, significant improvement in agreement with simulation results are observed compared with the original uncorrected sine profile. In Figure 4.7 (c), we plot the time evolution of the ejecta masses computed from the mass model described in eq. (1.13). The lines corresponding to cases 1 and 3 are plotted to the

times when the bubble velocities in each case drop to 0.1% of their initial peaks. We take the corresponding late-time masses as indicative of the asymptotic ejecta mass for that case. Thus, from Figure 4.7 (c), case 1 saturates to  $\sim 3.1 \text{ g/cm}^2$ , while the asymptotic mass from case 3 is  $\sim 3.3 \text{ g/cm}^2$ .

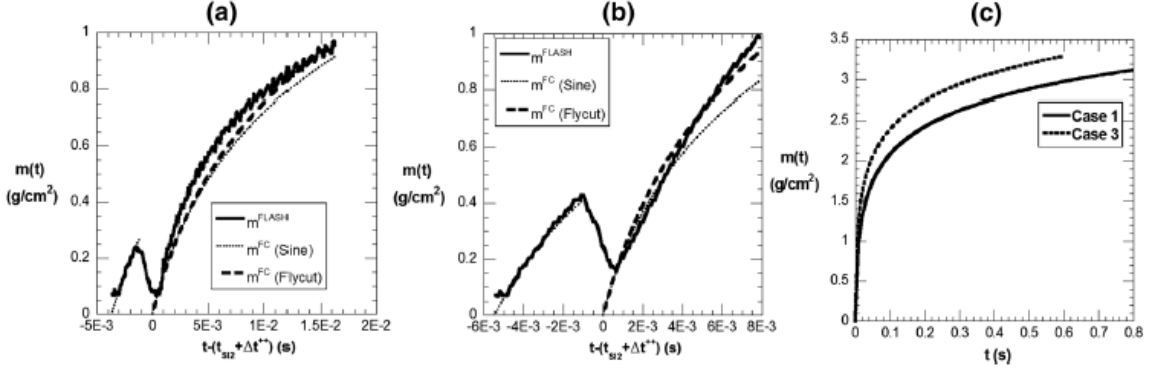


FIG. 4.7. Ejected mass from (a) case 1 and (b) case 3 compared with predictions from the mass model of [7] evaluated for sine and flycut profiles. (c) Time evolution of ejecta masses from cases 1 and 3, calculated using eq. (1.13).

We summarize our results in Figure 4.8, by comparing the scaled mass from cases 1 – 3 with the logarithmic mass model of [7]. Accordingly, we plot the mass ejections recorded in our simulations against the RHS from eq. (1.13). The ejected mass from each of the FLASH calculations is scaled by the corresponding  $m_0^{++}$  calculated for second-shock conditions using appropriate  $\lambda_{eff}$ , while the x-axis is the RHS from eq. (1.13) with  $\beta^{++}$  and  $\tau^{++}$  evaluated for second shock conditions. Thus, the diagonal represents perfect agreement with the model. The collapse of results from simulations with different  $kh_0^{++}$  in Figure 4.8 suggests the release of mass in double-shocked ejecta follows eq. (1.13),

and is explained by fitting a flycut to the bubble surface at second shock with an inferred  $\lambda_{\text{eff}}$ .

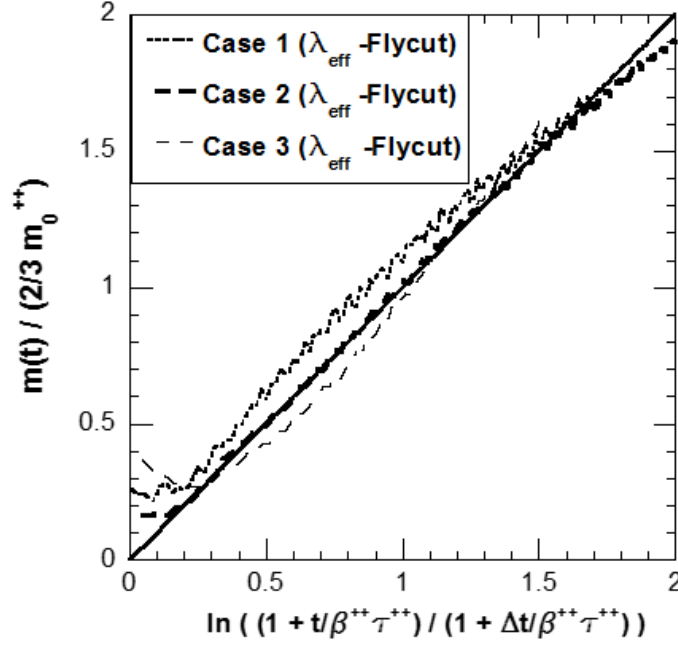


FIG. 4.8. Scaled ejecta mass from all FLASH simulations plotted against the prediction from the mass model of [7], eq. (1.13). The 45 degree line indicates perfect agreement.

### 4.3 Comparison with the experiments

In this section, we describe our results from FLASH simulations and comparison with the recent campaign of double-shocked, high-explosive (HE) experiments [18,17] conducted at the Los Alamos National Laboratory. Details of the experiment are reviewed only briefly here, and we refer the reader to [18,17] for additional information. A schematic of the two-shockwave package used in [18,17] is shown in Figure 4.9 (a), and includes a machined Sn target that is exposed to explosive loading generated by a HE PBX 9501 package coupled to a layer of TNT. The triggered detonation of the composite booster generates a shockwave incident on the target surface, while a reflected component is

returned from an anvil as the second shock. The experimental design allows for the ability to isolate rarefaction waves from the first and second shock impact events, so that the target releases to zero pressure in each case. Furthermore, the strength of the shocks can be controlled through the composition of the booster package to achieve pressures above or below melt. The time interval between shocks may also be manipulated by altering the thickness of the composite booster. Results from three shots at different first-shock pressures were reported in [18], but we choose to compare data from our hydrodynamic simulations with their highest-pressure shot (# 1756). This experimental run produced a shock pressure of 26.4 GPa [18], above the onset of the melt-on-release pressure for Sn which is estimated to be  $\sim 19.5$  GPa [52-54], so that the ejecta is comprised of a mixed phase of liquid and solid Sn. The experiments employed circular Sn targets with a diameter  $\sim 94$  mm, thickness  $\sim 4$  mm and were machined with grooves that may be characterized by a dominant wavelength  $\lambda \sim 80 \mu\text{m}$  and amplitude  $h_0 \sim 1.5 \mu\text{m}$  ( $kh_0^- \sim 0.12$ ). The experimental diagnostic package included a network of strategically positioned lithium-niobate (LN) piezoelectric probes and laser Doppler velocimetry (LDV) probes. The LDV probes report free-surface velocity measurements, while the LN piezo probes were utilized for ejecta mass measurements.



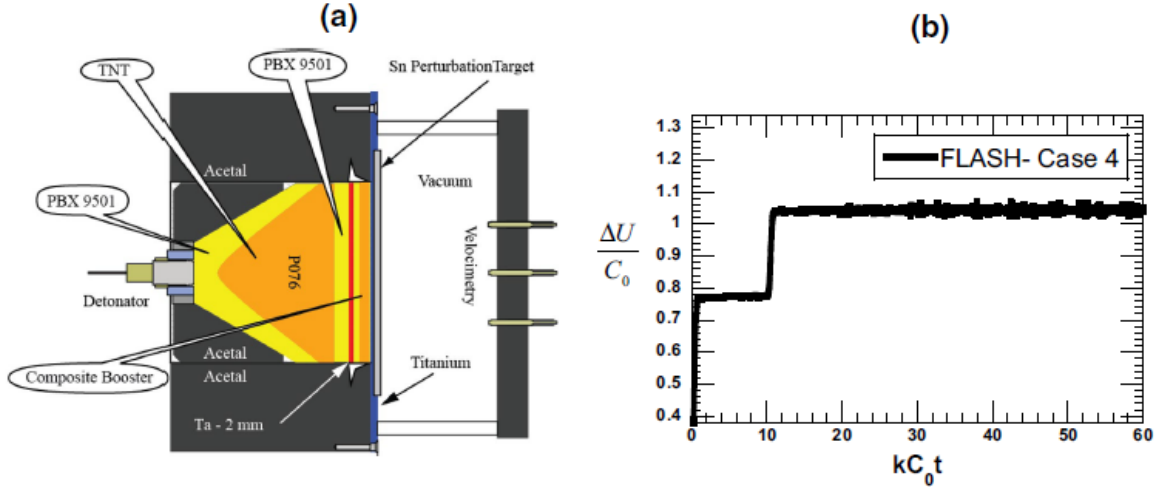


FIG. 4.9. (a) Schematic of the recent HE experiments conducted at LANL [18,17], with modifications to generate second shock, and (b) the scaled free-surface velocity from FLASH simulations.

Our approach to matching the experimental conditions is based on matching the inferred shock strengths for the first and second shocks reported in [18], as well as the scaled perturbation amplitudes on the target surfaces prior to  $SI_1$  and  $SI_2$ . The free surface velocities  $\Delta U^+$  ( $\Delta U^{++}$ ) after the first (second) shock for experimental shot 1756 is reported from LDV measurements to be 1.85 (0.5) mm/ $\mu$ s in [18] (Table 2). Applying the Rankine-Hugoniot relations in the ejecta limit [25], the post-shock particle velocity  $u_3^+$

may be estimated from  $\left(\frac{\Delta U^+}{u_3^+} \sim 2\right)$ . Finally, the incident shock velocities ( $W_i^-$  and  $W_i^{--}$ )

and corresponding Mach numbers used in the simulations are obtained from a ‘Us-Up’ relationship that relates the shock and particle velocities [45]. In our simulations, we match the experimental Mach numbers for the first and second shocks thus estimated. All other flow and material parameters are initialized using the methodology outlined in Chapter 2 and validated extensively for ejecta conditions in [7,25].

The perturbation amplitude at second shock was estimated for the experiments [18] from the measured ejecta and free-surface velocities and the estimated second shock speeds. The detailed analysis was carried out by [18] and involves using the nonlinear spike model [9] described in eq. (1.5) to project the measured spike velocities back in time to an initial undulation amplitude that must have existed at the time of second shock to source ejecta at that velocity. This inversion of eq. (1.5) leads to an expression for the scaled initial amplitude at second shock given by:

$$(kh_0^{--})^2 + 4\sqrt{3}(kh_0^{--}) \frac{1 - \left[ \Delta U^{++} / 2W_i^{--} \right]}{1 - \left[ (V_{sp}^{++} - \Delta U^+) / \Delta U^{++} \right]} + 4 = 0. \quad (4.3)$$

In the experiments [18,17],  $\Delta U^{++}$  and  $V_{sp}^{++}$  were obtained from LDV and Ln (from measured mass-velocity distributions) probes respectively. The incident second shock speed was estimated independently using detailed CTH simulations. The FLASH simulations reported below were designed by choosing a time interval ( $\Delta t$ ) between shocks such that the interface at second shock had the same scaled amplitude ( $kh_0^{--}$ ) as the experimental estimate (for the same second shock strength). However, note that there may be an important distinction between the experiments and simulations in the evolution of the interface leading to second shock. In the experiments, much of the ejecta generated from the *first shock* might have detached from the original interface likely due to surface tension-driven breakup, leaving behind an interface with  $kh_0^{--} \sim 0.5$  estimated from measured spike velocities (while some of this material may be recollected by the advancing spikes before second shock, thus complicating the picture even further). In

contrast, ejecta stay attached to the surface in the FLASH simulations, which did not include surface tension. We overcome this difference in first-shock interface evolution between experiments and simulations, by choosing  $\Delta t / \tau^+$  ( $\sim 1.1$ ) so that the scaled interface amplitudes at the time of second shock are comparable (in contrast, the experiments had  $\Delta t / \tau^+ \sim 140$ ). Since our main focus in this work is the generation of second shock ejecta, our use of different values of  $\Delta t / \tau^+$  in the simulation to achieve the same initial condition for second shock as the experiment is justified. Finally, we note the precise shape and amplitude of the perturbations at second shock in the experiments are not known from current measurements. We have attempted to overcome this gap in our knowledge of the experimental conditions through the analysis described above.

In Figure 4.9 (b), we plot free-surface velocities from a baseline unperturbed simulation ( $kh_0^- = 0$ ). The velocities in each case are scaled with the sound speed ( $C_0$ ) in the respective media. The corresponding experimental values obtained using LDV probes [18] are  $\frac{\Delta U^+}{C_0} \sim 0.7088 \pm 0.004$  for the first shock, and  $\frac{\Delta U^{++}}{C_0} \sim 0.9 \pm 0.079$  for the second shock in fair agreement with simulation results with Figure 4.9 (b). The agreement of the scaled velocities from FLASH (Figure 4.9 (b)) with experimental data is encouraging and serves to validate our strategy of performing simulations in which the shock strengths are matched with their experimental or application counterparts. The scaled bubble and spike velocities are shown in Figures 4.10 (a) and (b) and are plotted

against the scaled time  $\frac{t-t_{SI_2}}{\tau^{++}}$ . The saturated spike velocities from FLASH following

both shock events are in excellent agreement with the experimentally reported values shown in dashed lines (Figure 4.10 (b)). Note that both the experimental and simulation values are within 10 -15 % of eqs. (1.3), and (1.5). While the HE experiments do not directly report time-dependent data on bubble velocities, we compare bubble-tip velocities from FLASH with eq. (1.3) in Figure 4.10 (a). Following the first shock, we obtain a peak bubble velocity of  $V_{bu_0}^{FLASH+} \sim 1.08 V_{MB}^{+}$ , while eq. (1.8) predicts

$$V_{bu_0}^{FLASH+} / V_0^{MB+} = F_{bu}^{NL+} \sim 0.98, \text{ for an initial groove amplitude of } kh_0^{-} = 0.12 \text{ on the Sn}$$

target surface. Similarly, for second shock conditions we obtain  $V_{bu_0}^{FLASH++} \sim 0.9 V_{MB}^{++}$

which is consistent with the theoretical value of  $V_{bu_0}^{WB++} / V_0^{MB++} = F_{bu}^{NL++} \sim 0.92$  for a

scaled bubble amplitude prior to second shock of  $kh_{bu}^{--} \sim 0.5$ . Also, the time dependent bubble velocity history predicted by equation (1.3) (dashed line in Figure 4.10 (a)) is captured accurately by our simulations of experimental conditions.

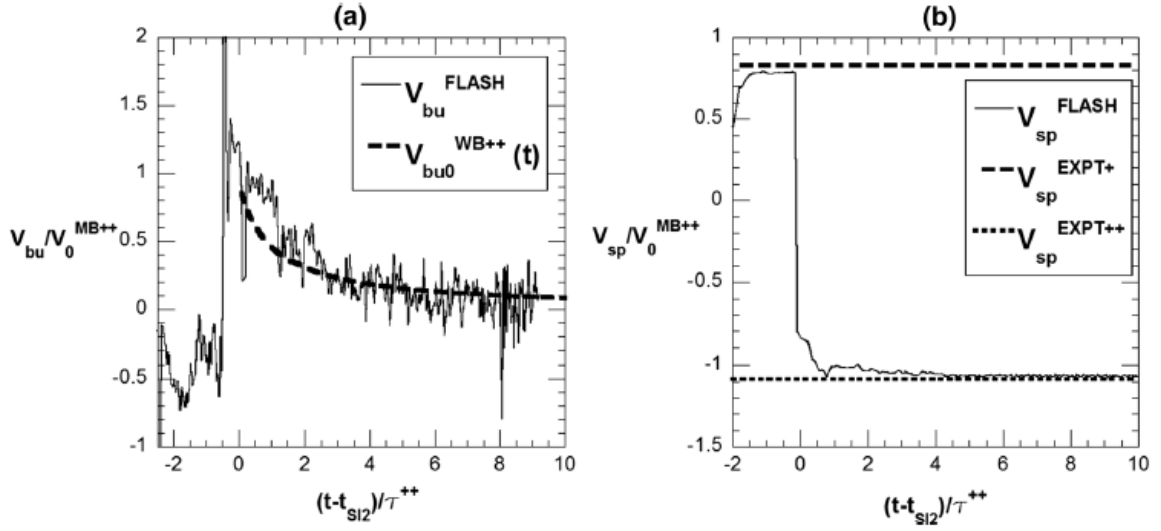


FIG. 4.10 Time evolution of scaled (a) bubble and (b) spike velocities from case 4. Simulation data is compared with prediction from ejecta model of [9] summarized eqs. (1.3), (1.5), and (1.8). and experimental data from [18].

The ejected mass from case 4 is plotted in Figure 4.11 and compared with the cumulative areal mass reported in the experiment [18]. In Figure 4.11 (a), we compare the ejecta mass with the model eq. (1.13) for both sinusoidal and flycut shapes with the effective wavelengths  $\lambda_{eff}$  consistently evaluated for each shape. As observed in §4.2, the correction to  $\lambda_{eff}$  corresponding to a flycut accounts for the additional missing area (and mass), and improves the agreement with the model relative to the sinusoid. In Figure 4.11 (b), we scale ejected mass from FLASH and experiments with  $\frac{2}{3}m_0^{++}$ , where  $m_0^{++}$  is evaluated for second-shock conditions. For FLASH simulations, this means  $\lambda_{eff}$  for flycut modifies  $m_0^{++}$  to  $(m_0^{++})_{flycut}$  of  $\sim 0.85 \text{ g/cm}^2$  from a baseline value of  $(m_0^{++})_{sine}$  of  $\sim 0.76 \text{ g/cm}^2$  for the corresponding sinusoid. For the HE experiments following the

second shock, [18] report an ejected mass of  $4 \text{ mg/cm}^2$  from two of the LN probes employed, while a third probe reported a value of  $12 \text{ mg/cm}^2$  (the reported values are accurate to within  $\pm 25\%$ , while the higher value may be attributed to contribution from a recompaction event associated with the first shock [18]). Based on these bounds, and evaluating  $\frac{2}{3}m_0^{++} \sim 4 \text{ mg/cm}^2$  for experimental conditions, we estimate the scaled mass

from [18] to lie between  $\sim 1$  and  $\sim 3$  in Figure 4.11 (b).

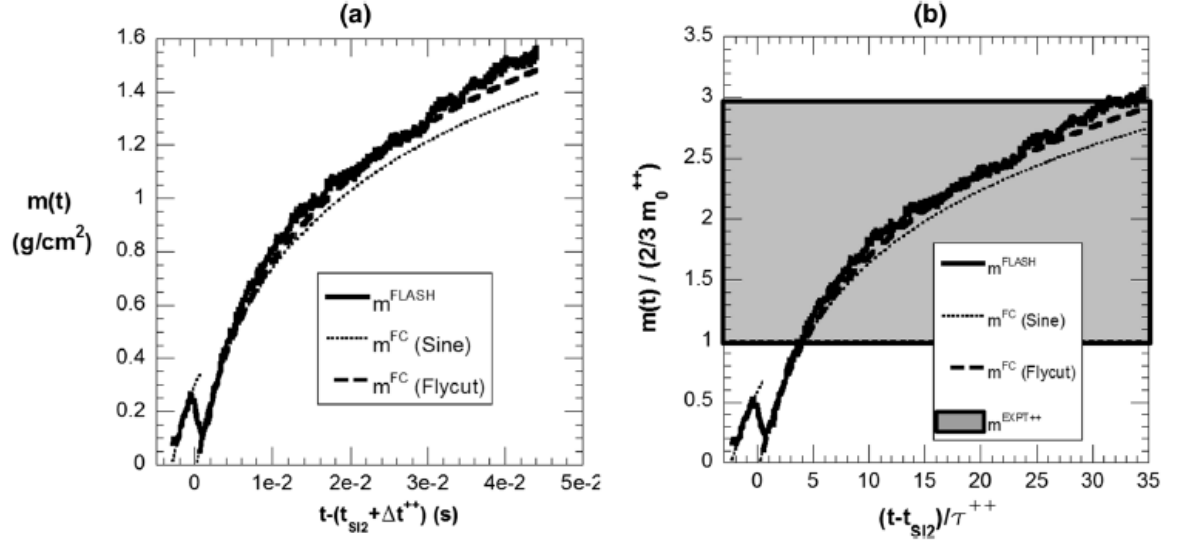


FIG. 4.11 (a) Ejected mass from case 4 compared with predictions from mass model of [7] evaluated for sine and flycut profiles. (b) Scaled ejecta mass from case 4, compared with data from the experiments of [18].

## CHAPTER 5: NUMERICAL STUDY OF BUBBLE AND SPIKE VELOCITIES IN SHOCK-DRIVEN LIQUID METALS

In this Chapter, we evaluate eqs. (1.3) – (1.5) (Chapter 1) by comparing with an extensive simulation database using FLASH, with different initial amplitudes and shapes. We find for bubbles, eq. (1.3) accurately captures growth rate prediction from the simulations, when used with the nonlinear bubble growth rate reduction from eq. (1.7). However, for spikes eq. (1.5) provides an upper bound corresponding to the linear limit, and overpredicts the simulation data even when  $V_0$  is corrected with eq. (1.6) for finite amplitudes. This is because nonlinearity limits both the initial growth rate ( $V_0$ ) and the asymptotic spike velocity (through the curvature). Instead, we suggest a more complete expression for spikes should be eq. (1.4), but with the initial spike velocity corrected by the nonlinear correction factor from eq. (1.6) thus giving:

$$V_{sp}(t) = F_{sp}^{NL} V_0^{MB} \sqrt{3 \frac{kh_0 + 1}{3kh_0 + 1}}. \quad (5.1)$$

Eq. (5.1) includes the effects of nonlinearity on the initial growth ( $F_{sp}^{NL}$ ), compressibility ( $F^C$ ) and the initial curvature, all of which are assumed to act independently of each other. The asymptotic spike velocities affect ejected mass through parameter  $\beta$  as detailed in Chapter 1. Using spike model of [34], we arrive at eq. (1.14) for  $\beta$ . We rewriting that equation here for completeness:

$$\beta^{KM} = 1 + \frac{1}{\sqrt{3}} \frac{F_{bu}^{NL}}{F_{sp}^{NL}}. \quad (5.2)$$

However, if nonlinear effects due to curvature are included, the asymptotic spike velocity is given by the proposed expression in (eq. 5.1), leading to the modified parameter  $\beta$ ,

$$\beta = 1 + \frac{1}{\sqrt{3 \frac{kh_0 + 1}{3kh_0 + 1}}} \frac{F_{bu}^{NL}}{F_{sp}^{NL}}. \quad (5.3)$$

Of course, in the limit of  $kh_0 \rightarrow 0$ ,  $\beta \rightarrow \beta^{KM}$  as expected.

Similarly, if we use the spike velocity from the empirical model of [25] in eq. (1.13), the following modified expression for  $\beta^{GD}$  is obtained:

$$\beta^{GD} = 1 + \frac{1}{\sqrt{\phi_{sp}^2 \frac{kh_0 + 1}{3M_i kh_0 + 1} \frac{1}{1 + \phi_{bu} kh_0}}} \frac{F_{bu}^{NL}}{F_{sp}^{NL}}. \quad (5.4)$$

In §5.4, we compare  $\beta^{KM}$ ,  $\beta$ , and  $\beta^{GD}$  from eqs. (5.2-5.4) above with results from numerical simulations.

### 5.1 Extension to non-sinusoidal shapes

As shown in our recent work [7,28], when ejecta are sourced from non-sinusoidal perturbations, it is the longest perturbation wavelength and corresponding amplitude that are responsible for most of the resulting ejecta mass. Thus, for any shape the ejecta mass from eq. (1.13) can be applied by replacing  $\lambda$  with an effective wavelength  $\lambda_{eff} = \frac{A_{sh}}{h_0}$ ,

where  $A_{sh}$  is the missing area associated with the perturbation cutout and  $h_0$  is the



perturbation amplitude. Simulations using continuum hydrodynamics and molecular dynamics confirmed this hypothesis, and showed [7] that eq. (1.13) can be extended to arbitrary shapes, when the effective wavelength of the equivalent sinusoid is used. In [28], this approach was extended to doubly-shocked ejecta, where the nonlinear bubble surface prior to second shock was approximated with a flycut profile. Using the effective wavelength for a flycut in eq. (1.13) predicted ejecta areal masses in agreement with FLASH simulations and HE experimental data [18]. Since, ejecta masses depend directly on the bubble velocity through eq. (1.11), and indirectly on the spike velocity through eq. (1.12), we expect the velocities from these models to collapse when scaled with  $\lambda_{eff}$ . For bubbles, we may thus write

$$V_{bu}^{WB}(t) = \frac{(V_{bu0}^{WB})_{eff}}{1 + t / \tau_{eff}}, \quad (5.5)$$

where  $(V_{bu0}^{WB})_{eff}$  is initial peak bubble growth rate from model of [9] (eq. (1.8)) evaluated

using  $\lambda_{eff}$  of the concerned shape, and  $\tau_{eff} = \frac{\lambda}{3\pi(V_{bu0}^{WB})_{eff}}$ . Similarly, the asymptotic

spike velocity from eq. (5.1) must be evaluated as

$$V_{sp}(t) = (F_{sp}^{NL})_{eff} (V_0^{MB})_{eff} \sqrt{3 \frac{(kh_0)_{eff} + 1}{3(kh_0)_{eff} + 1}}, \quad (5.6)$$

where the subscript ‘eff’ indicates that term be computed with the effective wavelength  $\lambda_{eff}$  associated with the shape. Finally, the ejecta areal mass from eq. (1.13) is rewritten for an arbitrary shape as

$$m(t) = \frac{2}{3} m_{0,eff} \ln \left( \frac{1 + \frac{t}{\beta_{eff} \tau_{eff}}}{1 + \frac{\Delta t}{\beta_{eff} \tau_{eff}}} \right). \quad (5.7)$$

We verify equations (5.5-5.7) in § 5.3-5.4, by comparing with FLASH simulations initialized using Sinusoidal, Gaussian, Flycut and Chevron profiles.

## 5.2 Initial amplitude variation (Sinusoidal interfaces)

We first present results from ejecta simulations using FLASH for baseline conditions characterized by a sinusoidal initial interface with different perturbation amplitudes  $(kh_0^- = 1/8, 2)$ , and at  $M_a = 2.5$ . We compare bubble and spike development from each case with corresponding model predictions from Chapter 1. Variations from this baseline are explored in § 5.3 - § 5.4.

Contours of the density field from the simulation with  $kh_0^- = 1/8$  are shown in figs. 5.1

(a) – (f). The individual panels correspond to different scaled times  $(t - t_{SI})/\tau$ , where  $t_{SI}$  is the time at which the incident shock impacts the interface. The white dashed line in each image shows the location of the corresponding (unperturbed) free-surface as a reference, and was obtained separately from 1D simulations. Even at the strong shock conditions investigated here, the post-shock Atwood number  $A^+$  remains  $\sim -1$ , while the post-shock amplitude  $h_0^+$  is substantially altered from its pre-shock value  $(h_0^-)$  through the effects of compressibility and phase inversion. For example, the incident planar shock in fig. 5.1 (a) (denoted by the high density region in white) compresses the perturbation amplitude from its pre-shock value of  $kh_0^- = 1/8$  to a post-shock value of  $kh_0^+ = 0.02$ .

The corresponding compressibility factor is  $\frac{h_0^+}{h_0^-} \sim 0.16$ , in agreement with the theoretical estimate given by  $F^C = 1 - \frac{\Delta U}{W_i} \sim 0.16$ . In addition to the shock compression, the interface also undergoes a phase inversion driven by the negative RM growth rate associated with  $A < 0$ .

Remnants of the reflected rarefaction for this heavy--> light problem are clearly visible in figs. 5.1 (b) – (c). The rarefaction fan decompresses the heavy fluid from its initial density ( $\rho_A$ ) of 8.93 g/cc to an eventual release density of ( $\rho_{rel}$ ) of 7.57 g/cc. Nonlinearities eventually appear by  $(t - t_{sl})/\tau \sim 2.8$  in Fig. 5.1(d), evidenced by the appearance of asymmetric bubble and spike structures. In particular, bubbles are parabolic in shape and eventually flatten (Figs 5.1(e)-(f)), while spikes tend to develop in to long and projected jets. We terminate the FLASH simulations at late times, when the ejecta span a few mesh cells across the jet, and are susceptible to numerical dissipation.

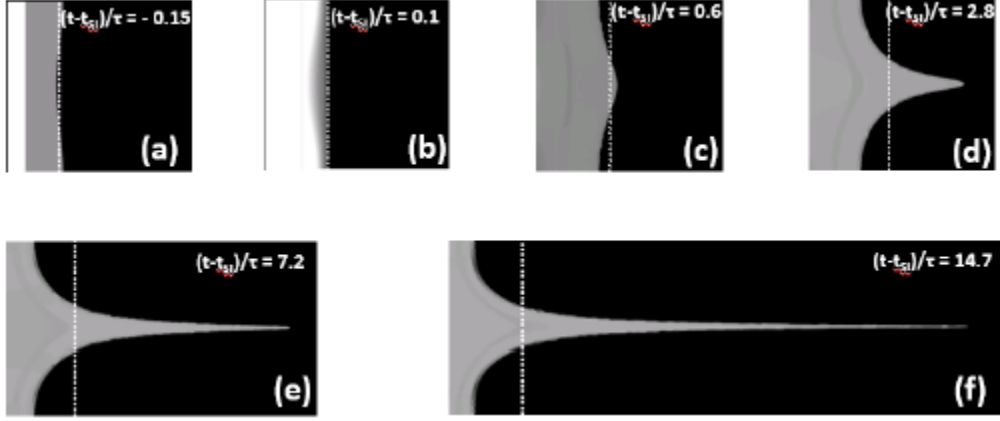


FIG. 5.1. Density contour images from FLASH simulations at different scaled times for an initially sinusoidal interface ( $kh_0=1/8$ ).

Fig. 5.2 is a plot of the streamwise profiles of the planar-averaged mass fraction of fluid

A ( $\langle Y_A \rangle$ ) and the scaled centerline velocity  $\left( \frac{V}{V_{sp}} \right)$  extracted from the  $kh_0^- = 1/8$

simulation. The sharp drop-off observed in the mass fraction profiles near the location where the scaled velocity reaches a maximum, suggests the spike tips may be tracked robustly through a mass fraction threshold value of  $\sim 1\%$ . The streamwise profiles serve to illustrate the internal structure of the ejecta, and show the significant asymmetry between bubble and spike features at this late time  $\left( (t-t_{sl})/\tau = 13.5 \right)$ .

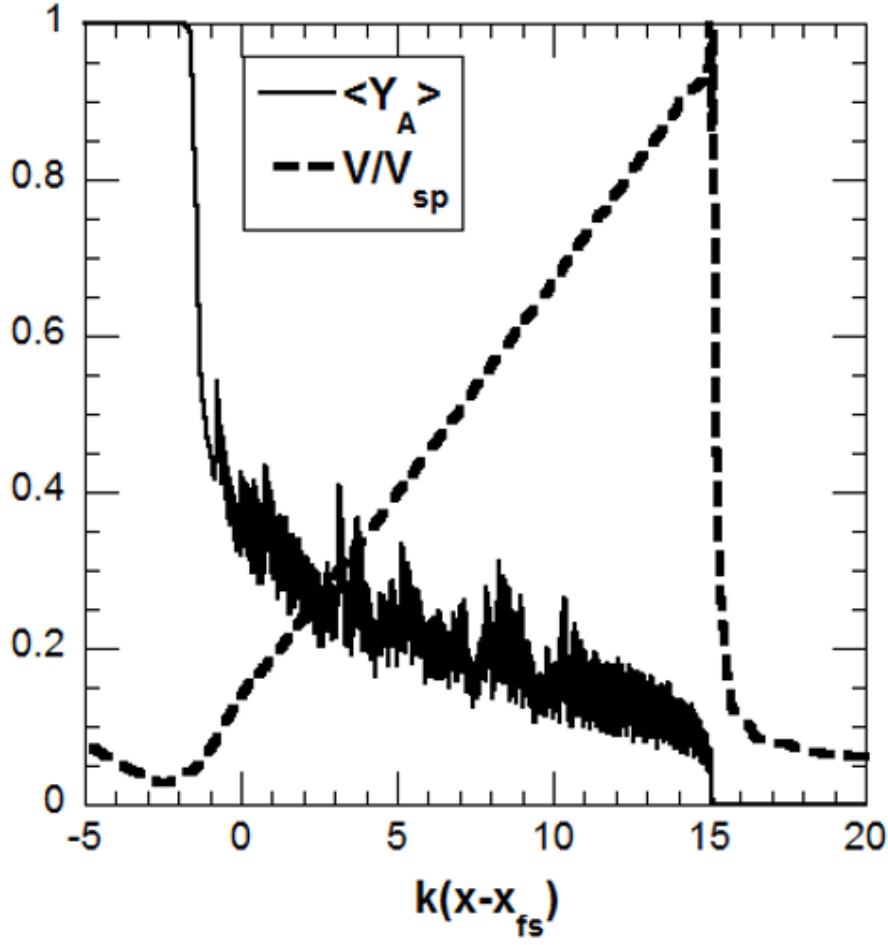


FIG. 5.2. Late time ( $t/\tau=13.5$ ) x-profiles of the planar-averaged mass fraction ( $\langle Y_A \rangle$ ), and the centerline scaled velocity ( $V/V_{sp}$ ) from FLASH simulation with  $kh_0=1/8$ .

To validate models in Chapter 2, we extract bubble and spike amplitudes and ejecta areal mass density from FLASH datafields using the procedure outlined in [7,28]. Following [7], the location of the bubble tip is identified as the x-position where the planar averaged (in y-) density falls below 90% of the release density  $\rho_{rel}$ . To determine the bubble amplitudes, the free surface location is required and obtained from enforcing mass conservation across the interface:

$$m(t) = \int_{x_{bu}(t)}^{x_{fs}(t)} (\rho_{rel} - \langle \rho(x) \rangle) dx = \int_{x_{fs}(t)}^{\infty} \langle \rho(x) \rangle dx, \quad (5.8)$$

In eq. (5.8),  $x_{bu}$ ,  $x_{fs}$  are the bubble and free-surface positions, while  $\langle \bullet \rangle$  refers to planar-averaging. The free-surface location  $x_{fs}$  is then iteratively calculated from eq. (5.8). We also use eq. (5.8) to evaluate the time-dependent ejecta mass,  $m(t)$  from our simulations. Finally, the spike positions  $x_{sp}$  are computed as the x-location where the y-averaged mass fraction of the heavy fluid reaches a threshold value of 1 %. The bubble/spike amplitudes are directly obtained as  $h_{bu/sp} = |x_{bu/sp} - x_{fs}|$ .

The time evolution of bubble and spike amplitudes thus obtained are shown in figs. 5.3 (a) – (b), while corresponding velocities are plotted in fig. 5.3 (c) as a function of the scaled time. To indicate the extent of nonlinearity at any time, we plot scaled amplitudes  $kh_{bu/sp}$ , where ‘k’ is the perturbation wavenumber. As the bubble tip flattens, the saturation of the amplitude is evident in fig. 5.3 (a) consistent with the curvature approaching  $|kh_{bu}| \sim 2$ . Spikes, on the other hand acquire a terminal velocity that is unabated in the presence of minimal amounts of viscous drag (numerical) encountered in the simulations. The corresponding velocities are shown in Fig. 5.3(c), and are scaled using the linear growth rate estimate from the Meyer-Blewett [35] model valid for  $A < 0$ . Since the initial amplitude  $kh_0 = 1/8 \ll 1$ , the instability is initialized in the linear regime, and the nonlinear growth rate reduction factors for both bubbles and spikes are close to unity ( $F_{bu}^{NL} \sim 0.98, F_{sp}^{NL} \sim 0.996$ ). This is evident in Fig. 5.3(c), where short-

lived peaks near  $(t-t_{sl})/\tau \sim 0$  signifying the initial growth rates approach  $\sim V_0^{MB}$  in agreement with eq. (1.8) for both bubbles and spikes.

For  $(t-t_{sl})/\tau \gg 1$ , bubble asymptotics closely follow the  $\frac{1}{V_{bu0}kt}$  trend line decay predicted by eq. (1.3) (Fig. 5.3c), when the initial bubble velocity  $V_{bu0}$  is evaluated consistently using the model of [9] (eq. 1.8). The asymptotic spike velocity is constant, but dependent on the initial perturbation amplitude through nonlinearities as well as the initial spike curvature as discussed earlier. From the simulations, we find that for  $(t-t_{sl})/\tau > 1$ , spikes average a velocity of  $V_{sp}/V_0^{MB} \sim 1.6 \pm 0.1$  between the upper bound of  $\sqrt{3}$  given by eq. (1.5) and the prediction from eq. (5.1) of  $\sim 1.56$ . Thus, eq. (1.5) is an upper bound for spike velocities that is realized in the limit of vanishing initial amplitudes, so that the spike curvature also vanishes. Already, at  $kh_0 = 1/8$ , this condition is violated as the simulation approaches the prediction of eq. (5.1) at late times. We also plot the empirical model of [25] in fig. 5.3 (c), and find that it overpredicts the simulation significantly. In fact, eq. 1.9 yields a value of  $V_{sp}/V_0^{MB} \sim 1.9$ , even higher than the upper bound set by eq. (1.5). This is due to the choice of the model parameter  $\phi_{sp} = 2.63$  in eq. (1.9), to fit experimental and simulation data at higher amplitudes. However, this leads to discrepancies at  $kh_0 \rightarrow 0$ , with the model predicting a scaled spike velocity of 2.625.

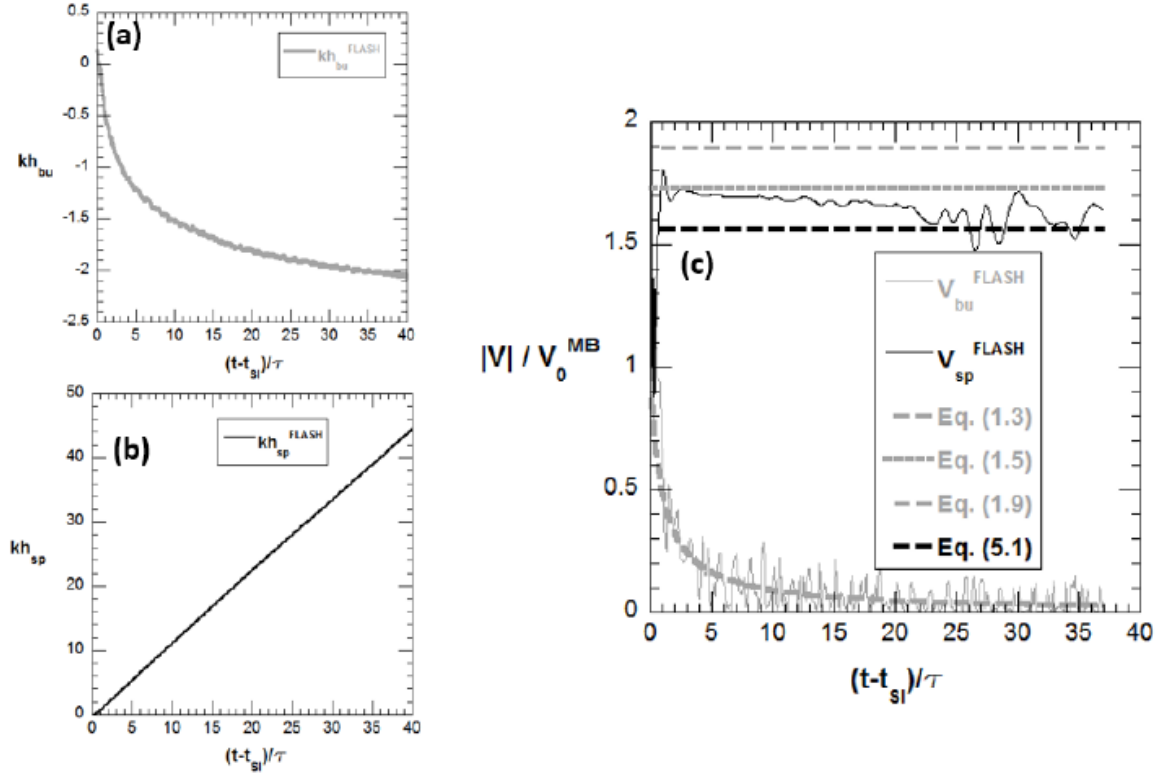


FIG. 5.3. Time evolution of scaled (a) bubble and (b) spike amplitudes, and (c) corresponding absolute scaled velocities ( $V_{bu/sp}/V_0^{MB}$ ) from FLASH simulations and comparison with models. Data from  $kh_0=1/8$  sinusoidal case.

We now test these models at large initial amplitudes using FLASH simulation data at  $kh_0^- = 2$ . In Fig. 5.4(a-f), we plot density contour images from the FLASH simulation at scaled times extending from -1.35 to 32.5. The Mach 2.5 incident shock compresses the interface amplitude from its initial value to a post-shock value of  $kh_0^+ = 0.3$ , so that  $\frac{h_0^+}{h_0^-}$

is in agreement with  $F^C = 1 - \frac{\Delta U}{W_i} \sim 0.159$ . The phase inversion observed in fig. 5.4 is

indirect [51] and due to the RM initial growth rate being negative. At the large initial



amplitudes, complex secondary features are observed on the bubble surface (Fig. 5.4(d-f)), and are attributed to the additional vorticity deposited at the interface due to the increased misalignment between the shock and the initial interface. The increased vorticity deposited on the original interface also manifests on the spike tip through the appearance of the additional material at late times. These features have been independently observed in recent target experiments [9] through pRad imagery.

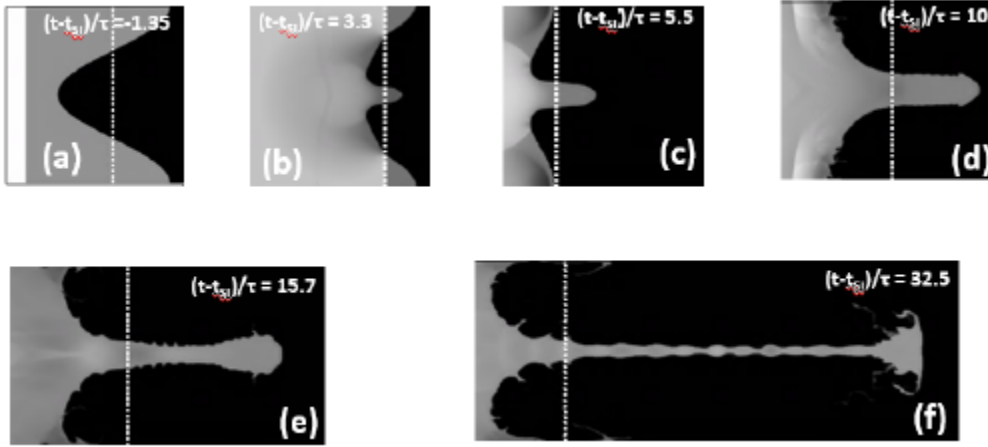


FIG. 5.4. Density contour images from FLASH simulations at different scaled times for initially sinusoidal interface ( $kh_0=2$ ). Dashed line is free surface.

Amplitudes and velocities from the large-amplitude FLASH calculation are shown in fig. 5.5, and are scaled as before. Following the initial phase inversion at  $(t-t_{SI})/\tau=5$ , bubbles quickly saturate to a constant amplitude while spikes stay terminal. At such large initial amplitudes, the initial bubble growth rate is significantly compromised resulting in a peak value of  $V_{bu}/V_0^{MB} \sim 0.8$ , before the initiation of the late-time decay. Thus, the peak growth rate reduction agrees with the prediction from the nonlinear correction

$F_{bu}^{NL} \sim 0.75$ . Once again, the asymptotic bubble velocity decay in fig. 5.5(c) is explained by the model of [36], with this value of  $F_{bu}^{NL}$ . For spikes, the initial growth rate reduction due to nonlinearity is significant, and given by eq. (1.6) to be  $F_{sp}^{NL} \sim 0.5$ . However, additional mitigation of spike velocity occurs through the effect of nonlinearity on curvature and is evaluated as  $\sqrt{3 \frac{kh_0 + 1}{3kh_0 + 1}} \sim 1.13$ , significantly lower than the  $\sqrt{3}$  upper bound from eq. (1.5). These two factors are combined in eq. (5.1), which predicts a scaled spike growth rate of  $\sim 0.57$  in good agreement with the reported value of  $\sim 0.5$  from FLASH simulations (obtained by averaging for  $(t - t_{sl})/\tau > 1$  as before). Note that even when eq. (1.5) is evaluated using  $V_0$  from eq. (1.8), it still predicts a scaled growth rate of  $\sim 0.86$  much higher than the observed simulation values in fig. 5.5 (c), highlighting the importance of the curvature effects at large amplitudes. The empirical model of [25] predicts a scaled spike velocity of  $\sim 0.6$ .

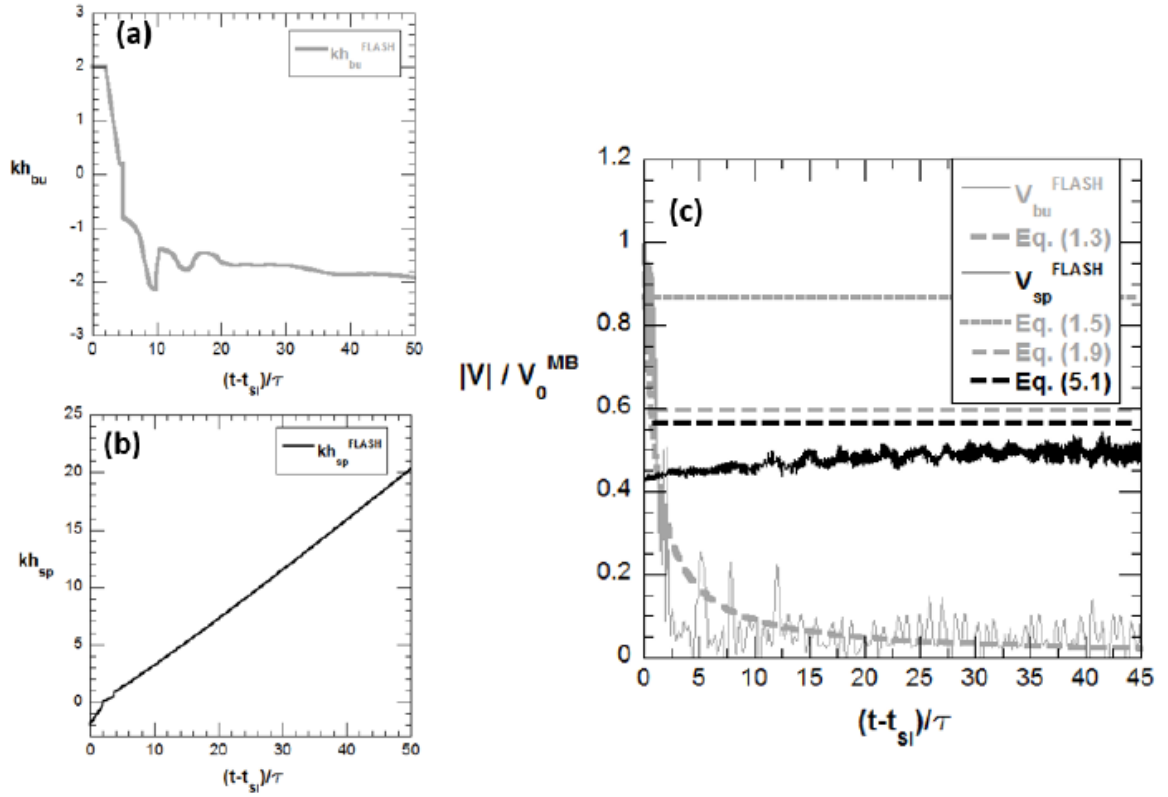


FIG. 5.5. Time evolution of scaled (a) bubble and (b) spike amplitudes, and (c) corresponding absolute scaled velocities ( $V_{bu/sp}/V_0^{MB}$ ) from FLASH simulations and comparison with models. Data from  $kh_0=2$  sinusoidal case.

In our simulations, we are also able to measure the initial growth rates associated with spikes and bubbles immediately after shock impact. We plot these growth rates scaled by the MB growth rate formula as a function of the non-dimensional initial amplitudes ( $kh_0$ ) in fig. 5.6. We are thus able to compare FLASH data for  $\frac{V_{0,bu/sp}}{V_{MB}}$  directly with the nonlinear correction factors for bubbles and spikes from eqs. (1.6-1.7). Fig. 5.6 shows excellent agreement between the simulations and the empirical fits to the Pade approximants of [39] suggested by [40] and [9].

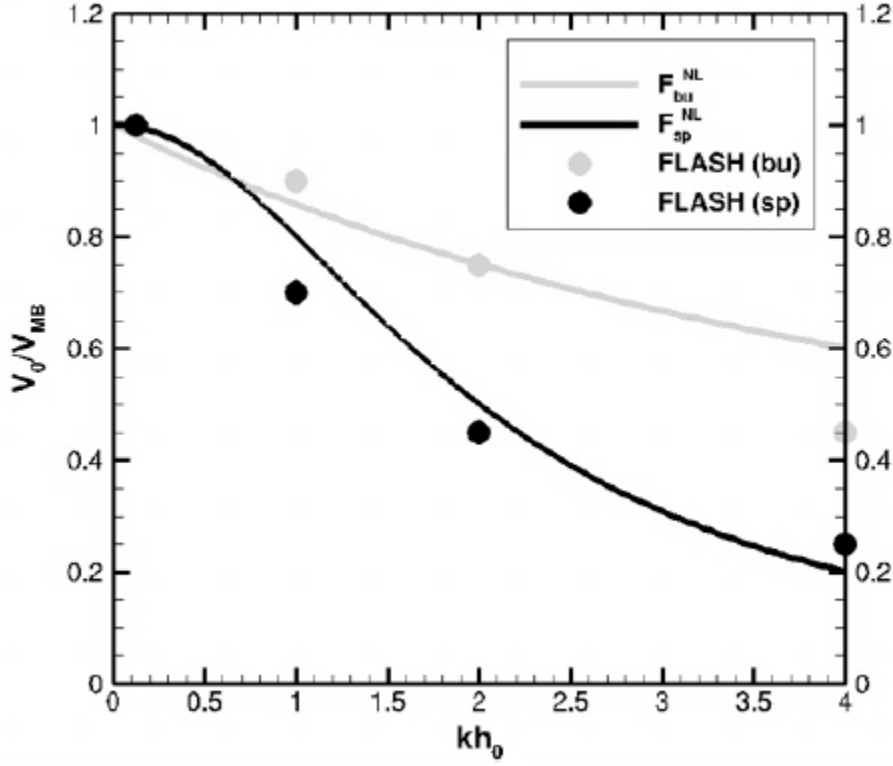


FIG. 5.6. Nonlinear factors for bubble and spike ( $F_{bu/sp}^{NL}$ ) embodied in eqs. (1.6-1.7) plotted against scaled initial amplitude ( $kh_0$ ), and comparison with data from FLASH simulations.

Thus, the amplitude variation study establishes the importance of accounting for nonlinear effects on both  $V_0$  (the initial growth rate), and the asymptotic velocity (through curvature). When the curvature effects are ignored (eq. 1.5), the models overpredict the simulations, while eq. (1.5) serves as an upper bound in the ideal limit of vanishing initial amplitudes. Due to the particular choice of the fitting parameter, the empirical model of [25] performs better at large initial amplitudes, but poorly as  $kh_0 \rightarrow 0$ . We now examine the validity of these ideas for ejecta that are sourced from non-sinusoidal shapes.

### 5.3 Non-sinusoidal Shapes

Shape effects are important in interpreting experimental results [18,17] from target experiments, where the free surface has been shocked more than once. Following the incident shock, the interface assumes a distinctly non-sinusoidal shape through the effect of higher harmonics as nonlinearities become dominant. In a recent study [28], it was shown that for second shock the interface presents a flycut profile, and the experimental measurements of areal mass densities [18,17] (from piezo probes) can be explained by properly accounting for the corresponding missing area in the source model of [7]. As shown in [7], this can be accomplished by defining the effective wavelength of an equivalent sinusoid that has the same missing area as the profile under consideration. In this section, we first extend this idea to the velocity models discussed above, before examining the implications to the mass models in § 5.4.

Table 5.1 provides a summary of the shapes studied using FLASH, along with the initial amplitudes and perturbation wavelengths in each case. The initial interface perturbation forms for the shapes listed in Table 5.1 are provided below (the sinusoidal form is repeated here for reference):

$$\text{Sinusoid: } h(y) = h_0 \cos(2\pi y / \lambda), \quad (5.9)$$

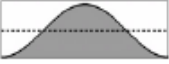


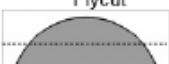
$$\text{Chevron: } h(y) = \frac{4h_0}{\lambda} |y| - h_0, \quad (5.10)$$

$$\text{Gaussian: } h(y) = 2h_0 \exp(-y^2 / 2c^2), \quad (5.11)$$

$$\begin{aligned}
 h(y) &= h_0 & 0 \leq y \leq \frac{\lambda}{2} - b \\
 \text{Flycut: } &= R - h_0 - \sqrt{R^2 - \left(y - \frac{\lambda}{2}\right)^2} & \frac{\lambda}{2} - b \leq y \leq \frac{\lambda}{2} + b \\
 &= h_0 & \frac{\lambda}{2} + b \leq y \leq \lambda
 \end{aligned} \quad (5.12)$$

For the Gaussian function, the standard deviation  $c$  was chosen to be  $\sim 0.2832$  cm in FLASH. The flycut profile in eq. (5.12) is characterized by  $R$  which represents the radius of the fly-cutter tool and  $b$  which signifies the intersection of the truncated circle with the free surface and is related to the radius:  $b = \sqrt{R^2 - (R - 2h_0)^2}$ . In table 5.1, we also indicate the missing area associated with each shape as the gray, shaded region along with the corresponding numerical estimate.

TABLE 5.1. Interface shapes investigated using FLASH ( $\lambda=1$  cm) simulations ( $kh_0=1/8, 0.5, 1$  and  $2$ ).

Shape \ kh0	Missing area, $A_{sh}$ (cm <sup>2</sup> )				$\lambda_{eff}$ (cm)				$k_{eff}$ (cm <sup>-1</sup> )			
	1/8	0.5	1	2	1/8	0.5	1	2	1/8	0.5	1	2
Sinusoidal 	0.02	0.08	0.16	0.32	1.0	1.0	1.0	1.0	6.28	6.28	6.28	6.28
Chevron 	0.02	0.08	0.16	0.32	1.0	1.0	1.0	1.0	6.28	6.28	6.28	6.28
Gaussian 	0.014	0.055	0.11	0.22	0.88	0.88	0.88	0.88	7.14	7.14	7.14	7.14
Flycut 	0.01	0.074	0.2	0.46	0.5	0.93	1.26	1.44	12.57	6.76	4.99	4.36

The corresponding expressions for the missing areas  $A_{sh}$  for the above shapes are:

$$\text{Sinusoid: } A_{sh} = h_0 \lambda, \quad (5.13)$$

$$\text{Chevron: } A_{sh} = h_0 \lambda, \quad (5.14)$$

$$\text{Gaussian: } A_{sh} = 2h_0 \left[ \lambda - \left\{ \sqrt{2\pi c} \operatorname{erf} \left( \frac{\lambda/2}{\sqrt{2c}} \right) \right\} \right] \quad (5.15)$$

$$\begin{aligned} A_{sh} &= \theta R^2 - b(R - 2h_0) & R > 2h_0 \\ \text{Flycut: } &= \theta R^2 + 2b(2h_0 - R) + bR \cos \theta & R < 2h_0 \end{aligned} \quad (5.16)$$

with  $\theta = \sin^{-1} \left( \frac{b}{R} \right)$ .

From eqs. (5.13-5.16), the effective wavelengths ( $\lambda_{eff} = \frac{A_{sh}}{h_0}$ ) for Sine, Chevron and

Gaussian shapes are independent of the corresponding initial perturbation amplitude. In contrast, the effective wavelength for the flycut (eq. 5.16) profile retains a dependence on  $h_0$  (Table 1). Furthermore, the missing area associated with the flycut depends on the relationship between the radius of the flycutter tool and the groove size as seen in eq. (5.16). For  $R > 2h_0$ , the flycut profile consists entirely of a truncated circle; When  $R < 2h_0$ , the flycut assumes a ‘U’ shape and the missing area is comprised of a truncated circle and a rectangle of area  $2b((2h_0 - R) + R \cos \theta)$ . Thus, the behavior of bubbles and spikes will be fundamentally different at low and high initial amplitudes, when seeded from a flycut function.

For the Gaussian function, eq. (5.11) suggests the free surface lies entirely to one side of the perturbation function, since  $h(y)$  is always  $> 0$ . As a result, the actual amplitude that is relevant to RM instability growth is  $h_0'$  (measured as distance from peak-to-valley), and

is related to  $h_0$  through  $h_0' = h_0 \left( 1 - \exp \left[ \frac{-(\lambda/2)^2}{2c^2} \right] \right) \sim 0.016 \text{ cm}$ . This results in

effective wavelength  $\lambda_{eff} = 0.88 \text{ cm}$  for Gaussian shape. For the same  $h_0$ , the flycut has  $\sim 50\%$  smaller area than the corresponding sinusoid resulting in  $\lambda_{eff} = 0.5 \text{ cm}$ .

The panels in fig. 5.7 correspond to snapshots of density contours from FLASH simulations at  $kh_0 = 1/8$  and with sine (a), Chevron (b), Gaussian (c) and Flycut (d) shapes respectively. As before, the dotted white line in each image shows the location of the unperturbed free surface. Consistent with the missing areas listed in table 1, the sine and Chevron profiles source identical bubble and spike structures. The effective wavelength for a Gaussian profile (0.88 cm) is close to the sine and Chevron functions (1 cm), and thus yields qualitatively similar bubble and spike structures with a phase shift of  $\pi$  radians (Fig. 5.7(c)). From table 1, the flycut profile has a smaller effective wavelength ( $\lambda_{eff} = 0.5 \text{ cm}$ ), such that the wavenumber  $k_{eff}$  is twice of that of the corresponding sinusoid. This leads to higher initial growth rates by a factor  $\sim 2$  relative to the baseline cases. For the  $kh_0 = 1/8$  simulation, the flycut had  $2b/\lambda = 0.37$ , which is the fractional length of the perturbation responsible for generating the baroclinic torque leading to spike growth. The remainder of the perturbation interface is a flat free surface.



As a result, the vorticity is concentrated within the narrow cavity leading to more aggressive spike growth in fig. 5.7 (d).

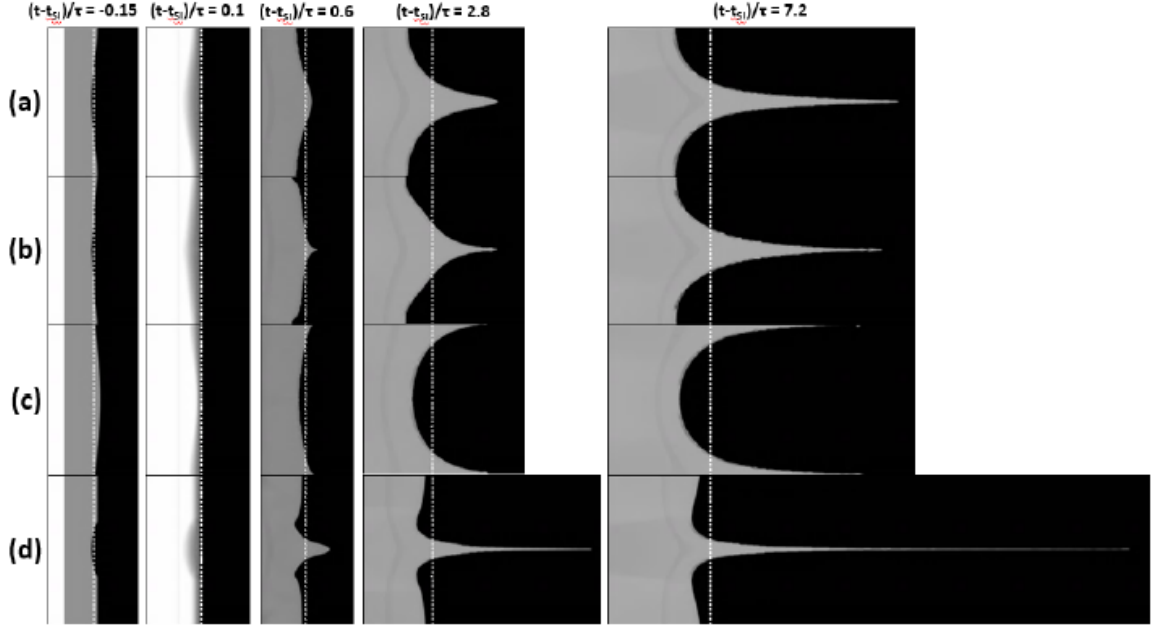


FIG. 5.7. Density contour images from FLASH simulations ( $kh_0=1/8$ ) for (a) Sinusoidal (upper panel), (b) Chevron (2<sup>nd</sup> panel), (c) Gaussian (3<sup>rd</sup> panel), and (d) Flycut (lower panel) at different scaled times. Dashed line is free surface.

In Figs. 5.8(a-b), we plot bubble and spike amplitudes for all the shapes with  $kh_0 = 1/8$ .

From fig. 5.8 (a), for any given time the bubble amplitude clearly scales with the initial missing area, and thus  $\lambda_{eff}$ . Spikes achieve a constant terminal velocity in each case (fig.

5.8 (b)) that is proportional to  $k_{eff}h_0$ . For example, the largest spike velocity is observed

for the flycut profile which had the highest effective perturbation wavenumber ( $k_{eff} \sim 12.57 \text{ cm}^{-1}$ ). The corresponding scaled velocities for bubbles and spikes are shown in

figs. 5.8 (c) – (d) respectively, where they are compared with the asymptotic models

which have now been evaluated with  $k_{eff}$ . When scaled with  $(V_{bu0})_{eff}$  (eq. 1.8 evaluated

with  $k_{\text{eff}}$ ) and plotted against  $t/\tau_{\text{eff}}$ , bubble velocities from all shapes collapse in fig. 5.8 (c). We also plot the bubble decay model of [36] in fig. 5.8 (c), which shows excellent agreement with simulation data for all shapes if the effective wavenumber is used as in eq. (5.5). We scale spike velocities in fig. 5.8 (d) with the RHS of eq. (5.6) to eliminate the explicit dependence on  $(kh_0)_{\text{eff}}$ , which results in a collapse of all the data. At late time, all the shapes produce scaled spike velocities close to unity, in excellent agreement with eq. (5.6).

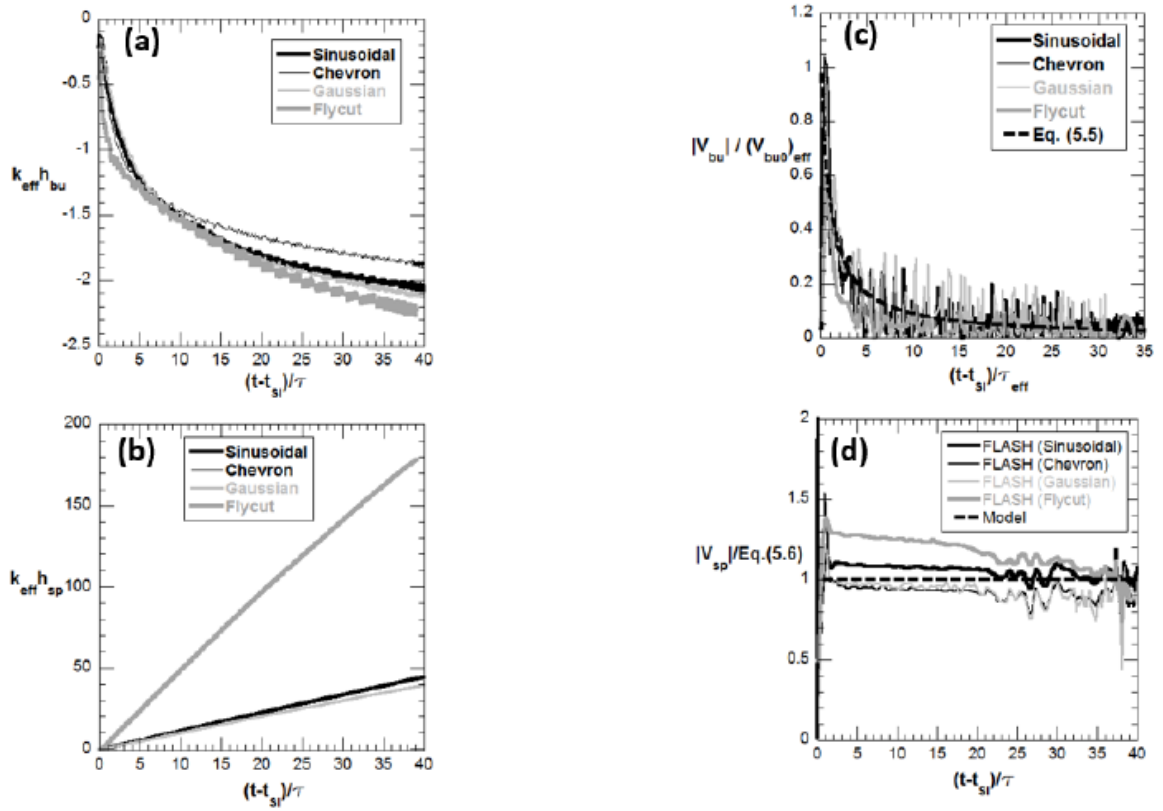


FIG. 5.8. Time evolution of scaled (a) bubble, and (b) spike amplitudes, and (c) bubble, and (d) spike velocities from FLASH simulations for all shapes with  $kh_0=1/8$ . Bubble velocities are scaled using eq. 1.8 [9] which is corrected for  $\lambda_{\text{eff}}$  of each shape. Spike velocities for different shapes are scaled using the asymptotic expression (eq. (5.6)).

The shape study is extended to higher initial amplitudes ( $kh_0 = 2$ ) in figs. 5.9 (a) – (d). Note that for flycut,  $\lambda_{eff}$  and  $k_{eff}$  are dependent on  $kh_0$ , so that at these large initial amplitudes, the flycut profile has ~44% additional missing area than the corresponding sinusoid (Table 1). This results in  $\lambda_{eff} \sim 1.44$  cm (higher than the sinusoid), while  $k_{eff} \sim 4.36 \text{ cm}^{-1}$  (~30% less than corresponding sinusoid). Hence, the relative trend from fig. 5.8 is now reversed, with bubbles from the flycut outpacing those from other shapes, while spikes lag. This can be explained in terms of the ratio  $2b/\lambda$  now evaluating to ~0.82 for  $kh_0 = 2$ , much higher than the corresponding value obtained at smaller amplitudes. Thus, the circular arc now occupies most of the perturbation surface, and is no longer concentrated at the center as in the  $kh_0 = 1/8$  case leading to lower baroclinic vorticity and spike growth rates. Scaling bubble velocities as before in fig. 5.9(c) collapses the data, and produces an average that agrees closely with the model eq. (5.5) which has been evaluated using the effective wavelength. When spike velocities are scaled with eq. (5.6), the data from all shapes studied here collapse to a value  $\sim 1$ . The disagreement with the empirical model from [25] is larger and averages to  $\sim 20$  %. Finally, as expected eq. (1.5) when evaluated with the effective wavelength significantly overpredicts the simulation data.

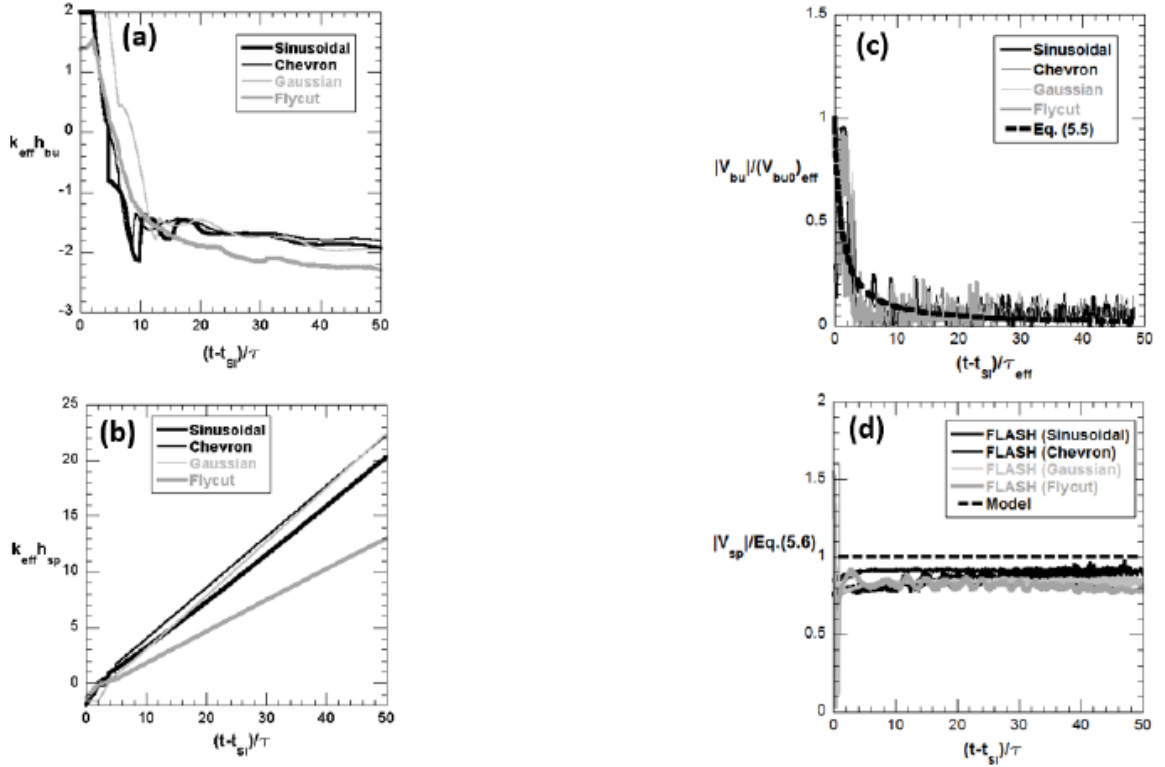


FIG. 5.9. Time evolution of scaled (a) bubble, and (b) spike amplitudes, and (c) bubble, and (d) spike velocities from FLASH simulations for all shapes with  $kh_0=2$ . Bubble velocities are scaled using eq. 1.8 [9] which is corrected for  $\lambda_{\text{eff}}$  of each shape. Spike velocities for different shapes are scaled using the asymptotic expression (eq. (5.6)).

We summarize these results for spikes in fig. 5.10 by plotting the asymptotic spike velocity from all the simulations scaled by the MB growth rate, and against the effective initial amplitude  $k_{\text{eff}} h_0$  for each case. Note that  $V_0^{\text{MB}}$  (eq. 1.2) must also be computed consistently for non-sinusoidal shapes using the appropriate  $\lambda_{\text{eff}}$ . At finite amplitudes, both the empirical model and eq. (5.1) agree with data from FLASH and SPaSM. At small initial amplitudes, the model of [25] significantly overpredicts the ejecta velocities. The gray line in fig. 5.10 is from eq. (1.5), with  $V_0$  calculated as suggested by [9] and

given by eq. (1.8). For all the cases included here, this model represents an upper bound that is violated for finite values of the initial amplitude.

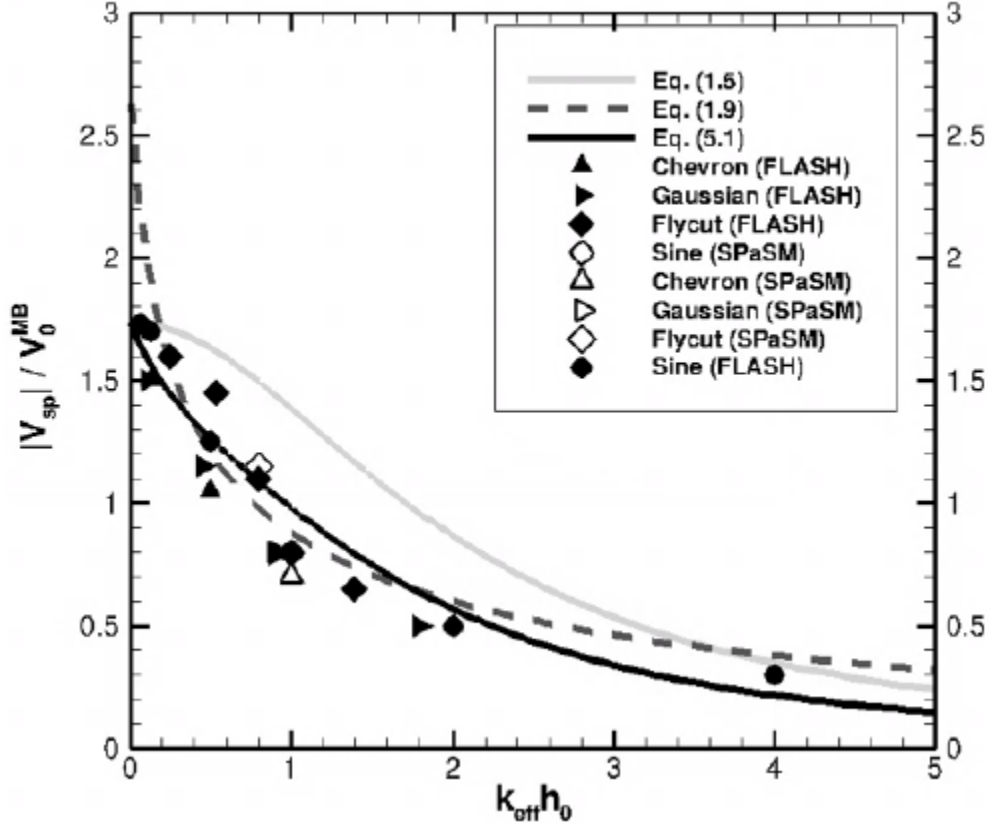


FIG. 5.10. Summary of simulations: asymptotic spike velocity ( $V_{\text{sp}}/V_0^{\text{MB}}$ ) from FLASH simulations (solid symbols), SPaSM simulations (open symbols) and models (lines) for all shapes plotted against initial amplitude ( $k_{\text{eff}} h_0$ ).

#### 5.4 Ejected mass per unit area

The initial bubble velocity and the asymptotic spike velocity influence the ejecta mass in eq. (1.13) through the parameter  $\beta$  (eq. 1.13). The simulations discussed in § 5.2 - 5.3 show bubble velocities are accurately described by eq. (1.3) [36], with the appropriate reduction factor  $F_{\text{bu}}^{\text{nl}}$  for the initial growth rate. We evaluate the ejecta areal mass by first computing  $\beta$  corresponding to the spike velocity models given in eqs. (1.5), (5.1) and

(1.9) (We refer to these as  $\beta^{KM}$ ,  $\beta$ , and  $\beta^{GD}$  respectively). This is shown in fig. 5.11, where we plot  $\beta$  from the numerical simulations with different initial amplitudes and shapes, and compare with eqs. (5.2) – (5.4). The large differences in spike velocities between eq. (1.5) and eq. (1.9) as  $kh_0 \rightarrow 0$  do not lead to large variations in  $\beta$  in that limit. For vanishing initial amplitudes,  $(F_{bu}^{nl}, F_{sp}^{nl})$  approach  $\sim 1$ , so that eqs. (5.2) and (5.3) both give  $(\beta^{KM}, \beta) \rightarrow 1 + \frac{1}{\sqrt{3}}$  in excellent agreement with our simulation data at  $kh_0=1/16$  and  $kh_0=1/8$  data. Using the empirical expression for  $V_{sp}^{GD}$ , eq. (1.9) gives  $\beta^{GD} \rightarrow 1 + \frac{1}{\phi_{sp}} = 1 + \frac{1}{2.625}$  in reasonable agreement with the simulations and the other models. For  $kh_0 < 2$ , the simulation data are closer to eqs. (5.3-5.4) than eq. (5.2). For  $kh_0 \gg 1$ , the model predictions for  $\beta$  are divergent; In that limit  $\frac{F_{bu}^{NL}}{F_{sp}^{NL}} \sim \frac{3}{2}kh_0$ , so that  $\beta$  from eqs. (5.2) and (5.3) approach  $1 + \frac{\sqrt{3}}{2}kh_0$  and  $1 + \frac{3}{2}kh_0$  respectively. When eq. (5.4) is evaluated for  $kh_0 \gg 1$ , we obtain  $\beta^{GD} \rightarrow 1 + 6\sqrt{3}M_i \frac{\phi_{bu}}{\phi_{sp}} = 3.8$  for  $M_i = 2.5$ , independent of  $kh_0$ . FLASH data obtained at  $kh_0 = 4$  lies closer to  $\beta^{KM}$ , than to  $\beta$  obtained from eq. (5.3). At all other amplitudes, the simulation data are closest to  $\beta$  calculated from eq. (5.3).

With the exception of the simulation data at  $kh_0 = 4$ , FLASH and SPaSM results for  $\beta$  are in excellent agreement with eq. (5.3). In fig. 5.12, we now compare the time-dependent ejecta masses from eq. (5.7) evaluated with  $\beta$  from eq. (5.3), and our simulation results at

$kh_0 = 1$ . The areal mass density is scaled using  $\frac{2}{3}m_{0,eff}$  corresponding to each shape, while the logarithmic term from eq. (5.7) is used as the abscissa. The observed collapse for all shapes from the simulations, and the alignment with the 45° degree reference line suggests agreement with eq. (5.7).

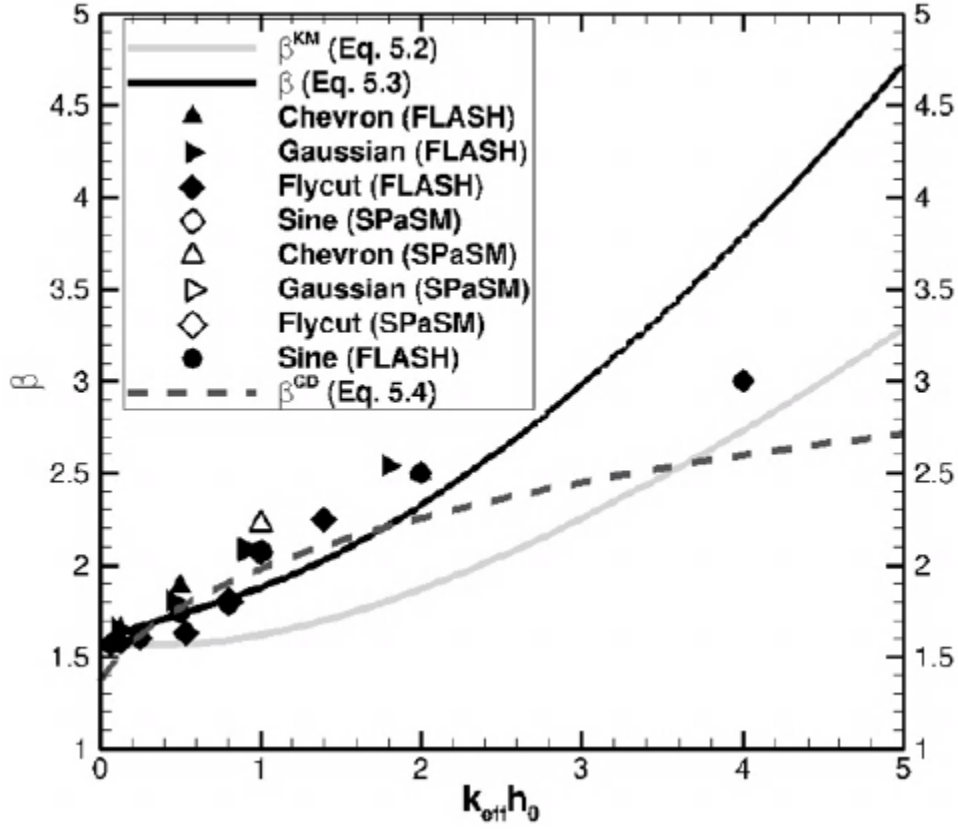


FIG. 5.11. Plot of parameter beta ( $\beta$ ) as a function of initial amplitude ( $kh_0$ ) from simulations and models.

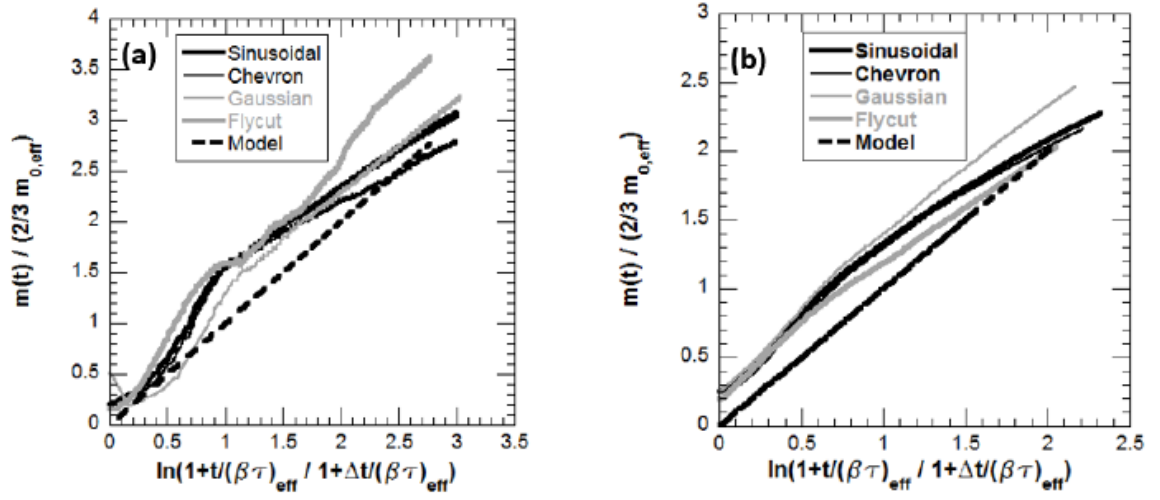


FIG. 5.12. Scaled ejected mass per unit area from: (a) FLASH simulations, (b) SPaSM simulations [7] with  $kh_0=1$  for all shapes studied in this work. Dashed 45-degree line indicates model prediction evaluated using modified expression of  $\beta$  (eq. 5.3).



## CHAPTER 6: SUMMARY AND CONCLUSIONS

We describe an approach in which continuum simulations using ideal gases can be used to capture key aspects of ejecta growth associated with the Richtmyer-Meshkov instability. The approach exploits the analogy between the Rankine-Hugoniot jump conditions for ideal gases and the linear relationship between the shock velocity and particle velocity governing shocked metals. Such simulations with  $\gamma$ -law fluids have been successful in accurately predicting the velocity and mass of ejecta for different shapes [7], and in excellent agreement with experiments. We define a conceptual fluid with the same density as that of metal, and find that it reproduces the hydrodynamic response of shocked metals to within 5% over a wide range of particle velocities (0-5 km/s). We use the astrophysical FLASH code, developed at the University of Chicago to model Richtmyer-Meshkov (RM) instability in metal-air configuration ( $A \rightarrow -1$ ) to mimic ejecta production in shocked metals. The details of the numerical setup using FLASH are provided in Chapter 2.

In Chapter 3, we present results from FLASH simulations and the comparison with recently proposed model to predict ejected mass per unit area [7] for any arbitrary shape. Two variants for the magnitude of the ejected mass per unit area have been considered and compared with detailed simulations using FLASH hydrodynamics code. These two model variants both account reasonably well for the magnitude and time dependence of the ejected mass. One (method I) incorporates local shape through an effective

wavelength,  $\lambda_{eff}$ , defined by the local geometry of the surface defect structure. A second (method II) incorporates shape through the first coefficient of the Fourier expansion giving an effective amplitude. Both methods assume that the late time bubble development is dominated by the longest wavelength, an assumption that is corroborated by the simulation results presented here. The model also accounts for the time dependent shape of the ingrowing bubble which gives rise to a reduction in ejected mass in the form of a pre-factor of  $2/3$ .

In a departure from most numerical studies of the RM instability, we have investigated the formation of ejecta from two shocks originating in the heavy fluid in Chapter 4. The saturated bubble surface from the first shock serves as the initial condition for the second shock, while the corresponding missing area of the bubble can be used to estimate the mass eventually ejected from spikes. Our analysis of first- and second-shock results builds extensively on a recent model that predicts bubble and spike velocities under ejecta conditions [9], as well as a model for ejecta mass [7]. The mass model is valid in principle for any shape and relates the time dependent mass to an effective wavelength associated with each shape. We have verified these models by comparing with velocities and mass predictions from our numerical simulations for first and second shock ejections. However, we find the agreement with the models is improved if the bubble surface just before the second shock impact is treated as a flycut profile with consistent geometric parameters that correspond to the wavelength, amplitude and radius of such a cutout. From these parameters, an effective wavelength  $\lambda_{eff}$  may be defined, which when used in eq. (1.13) successfully predicts the ejected mass from twice-shocked surfaces.

We test these ideas by comparing results from FLASH simulations with data from recent experiments involving a two-shockwave tool [18,17] at LANL. The experiments reported ejecta velocities and mass at different shock strengths using a combination of LDV and Ln piezoelectric probes. The highest pressure experiments from the LANL campaign had shock pressures that exceeded  $P_{\text{melt}}$  for Sn, so that the shocked metal is comprised of a mixed liquid-solid phase. Our FLASH model of that experimental shot matched the strengths of the first and second shocks, as well as the reported values of perturbation amplitudes of the interface prior to the shock events. This strategy appears to have merit, as predicted values of the ejecta velocity from our simulations are in good agreement with the experiment, and the models reviewed in this work (when the models are evaluated with  $\lambda_{\text{eff}}$ ), while the ejecta mass is slightly overpredicted. The experiments do not directly report bubble velocities, but we find the simulation values are in very good agreement with the model.

We note the comparison of ejecta mass between FLASH and the experiments [18] is complicated by several factors. For instance, the experiments likely experience a recompaction event of cavitated material from the first shock, so that the upper experimental bound reported in fig. 4.11 (b) includes some contribution from this phenomenon (while the lower bound may be indicative of a pure RM contribution). While the precise extent of the contribution of the recompaction process to  $m(t)^{\text{EXPT}}$  is not clear, it appears from fig. 4.11 (b) the simulations are near the upper limit of the measured mass from experimental second shock. There are several factors that could contribute to this modest discrepancy in  $m(t)$  (but not the spike velocities) between

FLASH and the experiments. The use of high explosives in the experiments result in a Taylor wave shock, while the numerical simulations use a supported shock. Previous studies [10,12,15] have shown for shock strengths above a critical value ( $\sim 230$  kbar for Sn), the jetting factors ( $R(\Theta) \equiv \frac{m(t \rightarrow \infty)}{\rho_A V_d}$ ;  $V_d$  is the initial defect volume) for supported and unsupported shocks diverge –  $R(\Theta)$  saturates for unsupported shocks, while increasing linearly with shock strength for supported shocks [19]. Data is unavailable for the exact experimental shock strength of  $\sim 26.4$  GPa, but a linear interpolation of available data in fig. 16 of [19] suggests we should expect an increase of  $\sim 45\%$  when using a supported shock. Applying this correction to  $\frac{m(t)}{\left(\frac{2}{3}m_0^{++}\right)}$  from FLASH in fig.

4.11 (b) suggests a downward revision to  $\sim 2.06$ . A detailed investigation of the effect of shock profile [55-58,38,59-61] is planned in future studies.

A second effect is the presence of viscosity in the experiments, which is excluded from the FLASH simulations to allow a direct comparison with eq. (1.13) which is inviscid. For Sn above melt ( $T \sim 550$  K), we obtain  $\mu_{SN} \sim 1.6$  mPa-s and  $\nu_{SN} \sim 2.24\text{e-}7$  m<sup>2</sup>/s from [62]. The solution to potential flow model augmented by viscosity of [63] suggests bubble velocities are affected by viscosity, but only logarithmically and according to

$$h_{bu}^{KM+}(t) = h_0 + \frac{2}{3k} \ln \left( 1 + \frac{3V_0^{RM+}}{4\nu k} (1 - e^{-\gamma t}) \right), \quad (6.1)$$

where  $\gamma$  is  $2\nu k^2$ . The corresponding reduction in bubble growth rate will be

$$V_{bu}^{KM+}(t) = \frac{V_0^{RM+}}{e^{\gamma t} + B(e^{\gamma t} - 1)}, \quad (6.2)$$

with  $B = \frac{3V_0^{RM+}}{4\nu k}$ . Evaluating eq. (6.2) for experimental conditions ( $t = 8\text{e-}6$  s,  $\gamma = 2.8\text{e}3$  s<sup>-1</sup>

<sup>1</sup>,  $B = 9.021\text{e}3$ ), we find the viscous bubble growth rate is reduced from the inviscid value by 10%. We expect the difference in ejecta masses between viscous and inviscid cases to be even smaller for the experimental conditions.

Velocities associated with bubble and spike features are critical to understanding the properties and quantity of ejecta that is generated when a metallic free surface is loaded by a shock wave. The time dependent behavior of the bubble, culminating in its eventual saturation determine the ejecta mass. Similarly, the spike velocities affect the ejecta transport process, but also the timescale of the problem via parameter  $\beta$  as shown recently in [7], and in Chapter 5. Fortunately, bubble and spike velocities in such applications are still explained by RM-based phenomenology, and we can rely on the extensive suite of linear and nonlinear models that are available. These models [36,9] suggest an expression for bubble velocities at  $A \rightarrow -1$  derived from potential flow approximations, summarized here in eq. (1.3). For spikes, existing models [38,9] have acknowledged the importance of nonlinearity in modifying the initial growth rates. However, as shown by the potential flow model of Zhang [33], the late-time spike velocities are also affected by nonlinearity through the curvature term. To successfully explain spike behavior at large initial amplitudes, both effects must be included as shown here in eq. (5.1).

A related issue is the dependence of ejecta properties on the shape of the initial cutout from which the ejecta are sourced. This issue gains salience in experiments where the free surface is shocked multiple times, such that the perturbation forms that are presented

for subsequent shocks are distinctly non-sinusoidal (and often nonlinear). Any successful model for bubble or spike velocities must also be able to predict ejecta from such non-sinusoidal shapes. In a recent paper [7], it was hypothesized that for any shape the largest wavelength in the Fourier spectrum determines most of the ejecta mass, and this effect can be captured by replacing the wavelength of that shape with the effective wavelength of a sine wave with the same missing area.

We have performed several continuum hydrodynamics simulations to test the above ideas, and develop insights in to the behavior of bubbles and spikes associated with the ejecta problem. By varying both the initial amplitudes and the shapes, we have tested the models for conditions that are relevant to target experiments. The simulations were performed assuming conditions above melt, and thus strength effects are not relevant to our study. The simulations suggest bubble and spike initial velocities are affected by the scaled perturbation amplitudes through eq. (1.8). According to data from the simulations, the asymptotic bubble velocity satisfies the model of [36] for all cases investigated here. Spikes assume a terminal velocity that is dependent on the initial RM growth rate (which could itself be affected by the initial amplitude), but also the curvature which could be written in terms of  $kh_0$ . Accounting for both effects through eq. (5.1) provides the best agreement with simulation data across the range of conditions investigated here. The empirical model in eq. (1.9) fails in the  $kh_0 \rightarrow 0$  limit, but matches simulation results for finite amplitudes due to the choice of tuning parameters. Similarly, eq. (1.5) does not include curvature effects and must be interpreted as an upper bound for spike velocities. We also extend eq. (5.1) to incorporate shape effects and find good agreement with

simulation results for all initial amplitudes. Finally, the recently proposed source model [7] agrees well with ejecta areal mass from the simulations, when evaluated with these expressions for bubble and spike velocities.

## REFERENCES

1. Lindl JD (1998) Inertial confinement fusion: the quest for ignition and energy gain using indirect drive. Springer-Verlag, New York
2. Zingale M, Woosley SE, Rendleman CA, Day MS, Bell JB (2005) Three-dimensional numerical simulations of Rayleigh-Taylor unstable flames in type Ia supernovae. *Astrophys J* 632 (2):1021
3. Herant M, Benz W, Hix WR, Fryer CL, Colgate SA (1994) Inside the supernova: A powerful convective engine. *Astrophys J* 435:339
4. Wang C-Y, Chevalier RA (2001) Instabilities and clumping in type IA supernova remnants. *Astrophys J* 549 (2):1119
5. Richtmyer RD (1960) Taylor instability in shock acceleration of compressible fluids. *Commun Pure Appl Math* 13 (2):297
6. Meshkov EE (1969) Instability of the interface of two gases accelerated by a shock wave. *Fluid Dyn* 4 (5):101
7. Cherne FJ, Hammerberg JE, Andrews MJ, Karkhanis V, Ramaprabhu P (2015) On shock driven jetting of liquid from non-sinusoidal surfaces into a vacuum. *J Appl Phys* 118 (18):185901
8. Hammerberg JE, Buttler WT, Cherne FJ, Andrews MJ, Karkhanis V, Ramaprabhu P, Stevens GD, Turley WD (2017) A Source Model for Ejecta. *J Dyn Behav Mat*:1-5
9. Buttler WT, Oró DM, Preston DL, Mikaelian KO, Cherne FJ, Hixson RS, Mariam FG, Morris C, Stone JB, Terrones G, Tupa D (2012) Unstable Richtmyer-Meshkov growth of solid and liquid metals in vacuum. *J Fluid Mech* 703:60
10. Zellner MB, Byers M, Dimonte G, Hammerberg JE, Germann TC, Rigg PA, Buttler WT (2009) Influence of shockwave profile on ejection of micron-scale material from shocked Sn surfaces: An experimental study. *DYMAT Int Conf Mech Phys Behav Mater Dyn Load* 1:89
11. Zellner MB, Buttler WT (2008) Exploring Richtmyer–Meshkov instability phenomena and ejecta cloud physics. *Appl Phys Lett* 93 (11):114102
12. Zellner MB, Vogan-McNeil W, Hammerberg JE, Hixson RS, Obst AW, Olson RT, Payton JR, Rigg PA, Routley N, Stevens GD, Turley WD, Veaser L, Buttler WT (2008) Probing the underlying physics of ejecta production from shocked Sn samples. *J Appl Phys* 103 (12):123502



13. Zellner MB, Vogan-McNeil W, Gray GT III, Huerta DC, King NSP, Neal GE, Valentine SJ, Payton JR, Rubin J, Stevens GD, Turley WD, Buttler WT (2008) Surface preparation methods to enhance dynamic surface property measurements of shocked metal surfaces. *J Appl Phys* 103 (8):083521
14. Vogan-McNeil W, Anderson WW, Grover M, Hammerberg JE, King NSP, Lamoreaux SK, Macrum G, Morley KB, Rigg PA, Stevens GD, Turley WD (2005) Piezoelectric characterization of ejecta from shocked tin surfaces. *J App Phys* 98 (11):113508
15. Schwarzkopf JD, Balachandar B, Buttler WT (2017) Compressible multiphase flow. In: Michaelides EE, Crowe CT, Schwarzkopf JD (eds). *Multiphase flow handbook*, 2nd Edn. CRC Press, Taylor & Francis Group, Boca Raton, pp 455–514
16. Buttler WT, Hixson RS, King NSP, Olson RT, Rigg PA, Zellner MB, Routley N, Rimmer A (2007) Method to separate and determine the amount of ejecta produced in a second-shock material-fragmentation event. *Appl Phys Lett* 90 (15):151921
17. Buttler WT, Oró DM, Mariam FG, Saunders A, Andrews MJ, Cherne FJ, Hammerberg JE, Hixson RS, Monfared SK, Morris C, Olson RT, Preston DL, Stone JB, Terrones G, Tupa D, Vogan-McNeil W (2014) Explosively driven two-shockwave tools with applications. *J Phys Conf Ser* 500 (11):112014
18. Buttler WT, Oró DM, Olson RT, Cherne FJ, Hammerberg JE, Hixson RS, Monfared SK, Pack CL, Rigg PA, Stone JB, Terrones G (2014) Second shock ejecta measurements with an explosively driven two-shockwave drive. *J Appl Phys* 116 (10):103519
19. Buttler WT, Zellner MB (2007) Tin ejecta data review: toward a statistical material fragmentation model. Los Alamos National Laboratory: Report LA-UR-07-6522:NM
20. Buttler WT, Zellner MB, Olson RT, Rigg PA, Hixson RS, Hammerberg JE, Obst AW, Payton JR, Iverson A, Young J (2007) Dynamic comparisons of piezoelectric ejecta diagnostics. *J Appl Phys* 101 (6):063547
21. Dimonte G, Terrones G, Cherne FJ, Germann TC, Dupont V, Kadau K, Buttler WT, Oro DM, Morris C, Preston DL (2011) Use of the Richtmyer-Meshkov instability to infer yield stress at high-energy densities. *Phys Rev Lett* 107 (26):264502
22. Asay JR, Bertholf LD (1978) Model for estimating the effects of surface roughness on mass ejection from shocked materials. Sandia National Laboratory: Report SAND-78-1256: NM
23. Asay JR, Mix LP, Perry FC (1976) Ejection of material from shocked surfaces.

- App Phys Lett 29 (5):284
24. Ren G, Chen Y, Tang T, Li Q (2014) Ejecta production from shocked Pb surface via molecular dynamics. J Appl Phys 116 (13):133507
  25. Dimonte G, Terrones G, Cherne FJ, Ramaprabhu P (2013) Ejecta source model based on the nonlinear Richtmyer-Meshkov instability. J Appl Phys 113 (2):024905
  26. Durand O, Soulard L (2015) Mass-velocity and size-velocity distributions of ejecta cloud from shock-loaded tin surface using atomistic simulations. J Appl Phys 117 (16):165903
  27. Ortega AL, Lombardini M, Pullin DI, Meiron DI (2014) Numerical simulations of the Richtmyer-Meshkov instability in solid-vacuum interfaces using calibrated plasticity laws. Phys Rev E 89 (3):033018
  28. Karkhanis V, Ramaprabhu P, Buttler WT, Hammerberg JE, Cherne FJ, Andrews MJ (2017) Ejecta Production from Second Shock: Numerical Simulations and Experiments. J Dyn Behav Mat:1-15
  29. Williams RJR (2016) The late time structure of high density contrast, single mode Richtmyer-Meshkov flow. Phys Fluids 28 (7):074108
  30. Durand O, Soulard L (2012) Large-scale molecular dynamics study of jet breakup and ejecta production from shock-loaded copper with a hybrid method. J Appl Phys 111 (4):044901
  31. Karkhanis V (2013) Doubly-shocked Richtmyer-Meshkov Instability. University of North Carolina at Charlotte
  32. Charakhch'an AA (2000) Richtmyer-Meshkov instability of an interface between two media due to passage of two successive shocks. J Appl Mech Tech Phys 41 (1):23
  33. Zhang Q (1998) Analytical solutions of Layzer-type approach to unstable interfacial fluid mixing. Phys Rev Lett 81 (16):3391
  34. Mikaelian KO (2008) Limitations and failures of the Layzer model for hydrodynamic instabilities. Phys Rev E 78 (1):015303
  35. Meyer KA, Blewett PJ (1972) Numerical Investigation of the Stability of a Shock-Accelerated Interface between Two Fluids. Phys Fluids 15 (5):753
  36. Mikaelian KO (1998) Analytic approach to nonlinear Rayleigh-Taylor and Richtmyer-Meshkov instabilities. Phys Rev Lett 80 (3):508

37. Layzer D (1955) On the Instability of Superposed Fluids in a Gravitational Field *Astrophys J* 122:1
38. Mikaelian KO (2010) Analytic approach to nonlinear hydrodynamic instabilities driven by time-dependent accelerations. *Phys Rev E* 81 (1):016325
39. Velikovich AL, Dimonte G (1996) Nonlinear perturbation theory of the incompressible Richtmyer-Meshkov instability. *Phys Rev Lett* 76 (17):3112
40. Dimonte G, Ramaprabhu P (2010) Simulations and model of the nonlinear Richtmyer–Meshkov instability. *Phys Fluids* 22 (1):014104
41. Velikovich AL, Herrmann M, Abarzhi SI (2014) Perturbation theory and numerical modelling of weakly and moderately nonlinear dynamics of the incompressible Richtmyer–Meshkov instability. *J Fluid Mech* 751:432
42. Fryxell B, Olson K, Ricker P, Timmes FX, Zingale M, Lamb DQ, MacNeice P, Rosner R, Truran JW, Tufo H (2000) FLASH: An adaptive mesh hydrodynamics code for modeling astrophysical thermonuclear flashes. *Astrophys J Suppl Ser* 131 (1):273
43. Colella P, Woodward PR (1984) The piecewise parabolic method (PPM) for gas-dynamical simulations. *J Comp Phys* 54 (1):174
44. FLASH ASC (2005) Flash user’s guide. University of Chicago, Chicago
45. Zel’dovich YB, Raizer YP (1996) *Physics of Shock Waves and High-Temperature Hydrodynamic Phenomena*. Academic INC, San Diego, CA
46. Mikaelian KO (1994) Freeze-out and the effect of compressibility in the Richtmyer–Meshkov instability. *Phys Fluids* 6 (1):356
47. Mikaelian KO (2005) Richtmyer–Meshkov instability of arbitrary shapes. *Phys Fluids* 17 (3):034101
48. Mansour NN, Lundgren TS (1990) Satellite formation in capillary jet breakup. *Phys Fluids A: Fluid Dynamics* 2 (7):1141
49. Webb III EB, Grest GS (2001) Liquid/vapor surface tension of metals: Embedded atom method with charge gradient corrections. *Phys Rev Lett* 86 (10):2066
50. Mikaelian KO (1993) Effect of viscosity on Rayleigh-Taylor and Richtmyer-Meshkov instabilities. *Phys Rev E* 47 (1):375
51. Yang Y, Zhang Q, Sharp DH (1994) Small amplitude theory of Richtmyer–Meshkov

- instability. *Phys Fluids* 6 (5):1856
52. Mabire C, Hereil PL (2000) Shock induced polymorphic transition and melting of tin. *AIP Conf Proc* 505 (1):93
  53. Mabire C, Hereil PL (2000) Shock induced polymorphic transition and melting of tin up to 53 GPa (experimental study and modelling). *J Phys IV* 10 (PR9):749
  54. Greeff C, Chisolm E, George D (2005) SESAME 2161: An explicit multiphase equation of state for tin. Los Alamos National Laboratory: Report LA-UR-05-9414:NM
  55. Ramaprabhu P, Karkhanis V, Banerjee R, Varshochi H, Khan M, Lawrie AGW (2016) Evolution of the single-mode Rayleigh-Taylor instability under the influence of time-dependent accelerations. *Phys Rev E* 93 (1):013118
  56. Drake RP, Leibbrandt DR, Harding EC, Kuranz CC, Blackburn MA, Robey H, Remington B, Edwards M, Miles A, Perry T, Wallace R (2004) Nonlinear mixing behavior of the three-dimensional Rayleigh–Taylor instability at a decelerating interface. *Phys Plasmas* 11 (5):2829
  57. Kuranz CC, Drake RP, Harding EC, Grosskopf MJ, Robey HF, Remington BA, Edwards MJ, Miles AR, Perry TS, Blue BE, Plewa T (2009) Two-dimensional blast-wave-driven Rayleigh-Taylor instability: experiment and simulation. *Astrophys J* 696 (1):749
  58. Mikaelian KO (2009) Reshocks, rarefactions, and the generalized Layzer model for hydrodynamic instabilities. *Phys Fluids* 21 (2):024103
  59. Shao JL, Wang P, He AM (2014) Microjetting from a grooved Al surface under supported and unsupported shocks. *J App Phys* 116 (7):073501
  60. Marc T Henry (2016) Numerical Simulations of Shock and Rarefaction Waves Interacting With Interfaces in Compressible Multiphase Flows, University of Michigan
  61. Ramaprabhu P, Karkhanis V, Lawrie AGW (2013) The Rayleigh-Taylor Instability driven by an accel-decel-accel profile. *Phys Fluids* 25 (11):115104
  62. Assael MJ, Kalyva AE, Antoniadis KD, Banish RM, Egry I, Wu J, Kaschnitz E, Wakeham WA (2010) Reference data for the density and viscosity of liquid copper and liquid tin. *J Phys Chem Ref Data* 39 (3):033105
  63. Mikaelian KO (2013) Shock-induced interface instability in viscous fluids and metals. *Phys Rev E* 87 (3):031003